

Halvor Njåstad Møgster

# Study of a novel fish farm concept consisting of a large-volume spar and nets

Master's thesis in Marine Technology

Supervisor: Trygve Kristiansen

June 2020

**NTNU**  
Norwegian University of Science and Technology  
Faculty of Engineering  
Department of Marine Technology



Norwegian University of  
Science and Technology



Halvor Njåstad Møgster

# **Study of a novel fish farm concept consisting of a large-volume spar and nets**

Master's thesis in Marine Technology  
Supervisor: Trygve Kristiansen  
June 2020

Norwegian University of Science and Technology  
Faculty of Engineering  
Department of Marine Technology





---

# Summary

For the last couple of years a lot of new fish farm concepts have emerged as a result of the granting of development licenses by the Norwegian Directorate of Fisheries. Several of which are complex structures consisting of large-volume components and nets, with slack mooring, planned to be located offshore. The purpose of this thesis has therefore been to study an example of such a structure and to assess the interaction between a large-volume structure and surrounding nets, both in regular waves and in current.

This subject was studied by performing both experimental tests and numerical calculations on a slack moored fish farm consisting of a large-volume spar in the centre, encircled by an octagonal framework, to which net-panels were attached. In order to study the influence nets have on the large-volume structure, all experiments and calculations were performed with and without nets.

The experimental results from the towing tests found that the drag of the fish farm was approximately doubled when nets were attached. These results were supported by numerical calculations. The numerical calculations further suggested that the nets themselves, when attached, comprise of the majority of the drag, as they reduced the drag on the other structural components. It was further found numerically that implementation of reduction factors to account for the influence of the nets on the flow, was essential to estimate the drag correctly. In addition it was found that taking into account the presence of the spar with respect to the flow, resulted in increased forces on the nets and more accurate numerical results.

From the experimental tests in regular waves there were found that the nets resulted in reduced motions, in addition to slightly alter the phases, mainly due to increased damping. This further resulted in smaller oscillatory and mean forces acting on the mooring system, with nets attached. However even though the mean forces were reduced with nets, it was found that they still were in the same order of magnitude as the drag forces in current, and should therefore be considered, for instance in the dimensioning of the mooring system. From the numerical calculations in regular waves there were obtained some results indicating that more accurate results might be achieved if the diffracted wave pattern from the large-volume structure is taken into account on the surrounding nets and columns. With respect to the nets, a numerical investigation was performed, in order to take a closer look into how the forces on the nets change if diffraction of the centre spar is taken into account, compared to assuming undisturbed waves. The results pointed towards the forces on the net-panels being increased, when taking diffraction into account. Likely a result of altered inflow angles and speed-up around the spar.

It is therefore concluded that there are several different interaction effects between nets and a large-volume structure in proximity of one another and some of these interactions have been identified and quantified both numerically and experimentally in this thesis.

---

# Sammendrag

I løpet av de siste par årene har det dukket opp mange nye konsepter for produksjon av laksefisker. Mye på grunn av Fiskeridirektoratets utdelinger av utviklingstillatelser. Mange av disse konseptene er komplekse konstruksjoner bestående av stor-volum komponenter og not, med slakk forankring, som videre er planlagt å være plassert offshore. Hensikten med denne oppgaven var dermed å studere et eksempel av en slik konstruksjon og videre se på samhandlingen mellom stor-volum komponenten og omkringende not, både i bølger og i strøm.

Dette temaet ble studert ved å gjennomføre både eksperimentelle forsøk og numeriske utregninger på et slakt forankret fiskeoppdrett, bestående av en stor-volum sentersøyle, omringet av et åttekantet rammeverk som not-panelene videre var festet i. For å kunne studere påvirkningen noten har på stor-volum konstruksjonen, så ble alle eksperiment og utregninger gjennomført med og uten not.

De eksperimentelle resultatene fra slepetestene viste at drag kreftene på fiskeoppdrettet ble doblet når not var festet på. Disse resultatene ble videre støttet av numeriske utregninger. De numeriske utregninger viste videre at når not var festet på, så stod noten for majoritet av drag kreftene, da noten reduserte kreftene på de andre konstruksjonsdelene. Det ble videre funnet numerisk at implementeringen av reduksjonsfaktorer, for å ta i betraktning påvirkningen fra noten på strømmingen, var essensielt for å estimere drag kreftene riktig. I tillegg ble det funnet ut at å ta hensyn til sentersøylens påvirkning på strømmingen resulterte i økte krefter på noten, samtidig som det ga mer nøyaktige resultat.

Fra de eksperimentelle forsøkene i regulære bølger ble det funnet at noten resulterte i mindre bevegelser, i tillegg til å endre fasene til bevegelsene noe. Hovedsakelig på grunn av økt demping. Dette førte videre til reduserte oscillerende og midlere krefter på forankringssystemet. Selv om de midlere kreftene i bølger ble redusert med not, så var de likevel fortsatt i samme størrelsesorden som drag kreftene i strøm for fiskeoppdrettet med not. De midlere drift-kreftene fra bølger bør derfor fortsatt tas hensyn til, for eksempel ved dimensjoneringen av forankringssystemet til en slik konstruksjon. Fra de numeriske utregningene i regulære bølger ble det oppnådd resultater som pekte i retningen av at mer nøyaktige utregninger kan bli oppnådd, dersom man tar hensyn til det diffrakterte bølgeprofilen fra stor-volum konstruksjonen, når man regner kreftene på omkringende not og søyler. Med tanke på noten, så ble det gjennomført en numerisk sammenligning der resultatene indikerte at kreftene på noten øker når man tar hensyn til diffraksjon. Mest sannsynlig som et resultat av hastighetsøkning rundt sentersøylen og endrede innstrømningsvinkler på noten.

Det blir derfor konkludert med at det vil være flere samhandlingseffekter mellom not og en stor-volum konstruksjon i nærheten av hverandre og noen av disse interaksjonene har blitt identifisert og kvantifisert både numerisk og eksperimentelt i denne oppgaven.

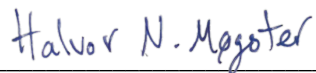
---

# Preface

This Master's thesis is the result of work performed during the spring of 2020 and represents the end of my Master in Science in Marine Technology at the Norwegian University of Science and Technology in Trondheim.

I would like to thank my supervisor Professor Trygve Kristiansen for providing me with excellent advice, interesting suggestions, good guidance and valuable discussions throughout this semester.

In addition I would like to thank Trond Innset and Ole Erik Vinje for great cooperation and help with the planning and creation of the experimental model. Further I would like to express my gratitude towards Terje Rosten and Torgeir Wahl for helping me out with the instrumentation used in the experiments and with the conduction of the experiments in general.



---

Halvor Njåstad Møgster

Trondheim, June 10, 2020

---



# Table of Contents

<b>Summary</b>	<b>i</b>
<b>Sammendrag</b>	<b>ii</b>
<b>Preface</b>	<b>iii</b>
<b>Table of Contents</b>	<b>vii</b>
<b>Abbreviations</b>	<b>viii</b>
<b>Nomenclature</b>	<b>ix</b>
<b>1 Introduction</b>	<b>1</b>
<b>2 Literature Review</b>	<b>3</b>
<b>3 Theoretical Background</b>	<b>5</b>
3.1 Viscous loads in steady current . . . . .	6
3.2 Wave loads on nets, slender elements and large-volume structures . . . . .	9
3.2.1 Definition of coordinate system and DOFs . . . . .	9
3.2.2 Equations of motion . . . . .	10
3.2.3 Mass matrix . . . . .	12
3.2.4 Stiffness matrix . . . . .	12
3.2.5 Linear potential flow theory . . . . .	15
3.2.6 Diffraction . . . . .	16
3.2.7 Radiation . . . . .	18
3.2.8 Added mass . . . . .	19
3.2.9 Potential damping . . . . .	20
3.2.10 Wave excitation forces on slender elements . . . . .	21
3.2.11 Wave excitation forces on nets . . . . .	23
3.2.12 Viscous damping . . . . .	27

---

3.3	Natural periods . . . . .	27
3.4	Additional non-linear effects . . . . .	29
3.4.1	Mean wave-drift forces . . . . .	29
3.4.2	KC-number dependency of $C_D$ and $C_m$ . . . . .	32
<b>4</b>	<b>Numerical Method</b>	<b>35</b>
4.1	Steady current . . . . .	35
4.1.1	Modelling of flow . . . . .	35
4.1.2	Spar . . . . .	37
4.1.3	Columns . . . . .	38
4.1.4	Nets . . . . .	39
4.1.5	Wave resistance . . . . .	40
4.2	Regular waves . . . . .	41
4.2.1	Modelling of flow . . . . .	41
4.2.2	Spar . . . . .	41
4.2.3	Columns . . . . .	44
4.2.4	Nets . . . . .	45
4.2.5	Solving the equations of motion using ODE45 . . . . .	45
<b>5</b>	<b>Experimental Method</b>	<b>47</b>
5.1	Description of model . . . . .	47
5.2	Experimental setup towing tests . . . . .	49
5.3	Experimental setup regular wave tests . . . . .	50
5.4	Decay test setup . . . . .	53
5.5	Experimental sources of error . . . . .	53
<b>6</b>	<b>Results and Discussion</b>	<b>55</b>
6.1	Current forces . . . . .	55
6.1.1	Experimental results . . . . .	55
6.1.2	Comparison of experimental and numeric results . . . . .	59
6.1.3	Summary of experimental and calculated results in current . . . . .	64
6.2	Natural periods . . . . .	64
6.3	Experimental and numerical results in regular waves . . . . .	67
6.3.1	Experimental results . . . . .	67
6.3.2	Comparison numerical and experimental results . . . . .	81
6.3.3	Numerical assessment of the effect of diffraction on nets . . . . .	91
<b>7</b>	<b>Conclusion</b>	<b>93</b>
	<b>Bibliography</b>	<b>95</b>
	<b>Appendix</b>	<b>I</b>
A	Flow Regimes . . . . .	I
B	Supplementary Theory . . . . .	II
B.1	Diffraction Theory . . . . .	II
C	Experimental results for sway, roll and yaw . . . . .	V

---

---

C.1	Sway . . . . .	V
C.2	Roll . . . . .	VII
C.3	Yaw . . . . .	VIII
D	Stiffness and mass-matrices . . . . .	XI
D.1	With nets . . . . .	XI
D.2	Without nets . . . . .	XI
E	Natural periods using logarithmic decrement . . . . .	XII
F	Hydrodynamic quantities from WAMIT . . . . .	XIV
G	Net-panel moments . . . . .	XV

---

# Abbreviations

DOF = Degree of freedom  
CFD = Computational fluid dynamics  
KC = Keulegan-Carpenter  
RAO = Response amplitude operator

---

# Nomenclature

$Re$	=	Reynolds number
$\zeta_a$	=	Wave amplitude
$\zeta$	=	Surface elevation
$k$	=	Wave number
$\omega$	=	Wave frequency
$T$	=	Wave period
$g$	=	Gravitational acceleration
$KC$	=	Keulegan-Carpenter number
$H(\omega)$	=	Response amplitude operator
$F_D$	=	Drag force
$\rho$	=	Density of water
$C_D$	=	Drag coefficient
$C_D^{c,c}$	=	Drag coefficient circular cylinder
$U$	=	Fluid velocity
$A$	=	Projected area
$A_{net}$	=	Projected area of net
$D$	=	Diameter or characteristic length
$R$	=	Radius or radial coordinate using a polar coordinate system
$\nu$	=	Kinematic viscosity of water
$\phi$	=	Velocity potential or phase angle of motions
$St$	=	Strouhals number
$f_v$	=	Vortex shedding frequency
$U_R$	=	Reduced velocity
$f_n$	=	Natural frequency
$Sn$	=	Solidity
$U_s$	=	Fluid velocity accounting for speed-up between twines
$\eta_1 \eta_2 \eta_3 \eta_4 \eta_5 \eta_6$	=	Motion in surge, sway, heave, roll, pitch and yaw
$I_{44} I_{55} I_{66}$	=	Moment of inertia in roll, pitch and yaw
$M$	=	Mass
$M_i$	=	Point mass
$z_G$	=	Vertical position of centre of gravity
$z_B$	=	Vertical position of centre of buoyancy
$C_{33}^{hs} C_{44}^{hs} C_{55}^{hs}$	=	Hydrostatic stiffness in heave, roll and pitch
$C_{11}^{ms} C_{22}^{ms} C_{33}^{ms}$	=	Mooring system stiffness in surge, sway and heave
$C_{44}^{ms} C_{55}^{ms} C_{66}^{ms}$	=	Mooring system stiffness in roll, pitch and yaw
$\phi_0$	=	Incident velocity potential
$\phi_7$	=	Diffraction potential
$\phi_j$	=	Radiation potential for DOF $j$
$A_{wp}$	=	Waterplane area

---

$\dot{\eta}_1 \dot{\eta}_2 \dot{\eta}_3 \dot{\eta}_4 \dot{\eta}_5 \dot{\eta}_6$	=	Velocity in surge, sway, heave, roll, pitch and yaw
$\nabla$	=	Volume displacement
$\overline{GM}_T$	=	Transverse metacentric height
$\overline{GM}_L$	=	Longitudinal metacentric height
$I_{xx}$	=	Second moment of area inertia around $x$ -axis
$I_{yy}$	=	Second moment of area inertia around $y$ -axis
$k_i$	=	Mooring line stiffness
$\psi_i$	=	Horizontal mooring line angle
$l_i$	=	Mooring line length
$P_i$	=	Mooring line pretension
$\theta$	=	Mooring line angle, inflow angle, mooring force phase, angular coordinate
$H_m^{(2)}$	=	Hankel function of second kind
$J_m$	=	Bessel function of first kind
$i$	=	imaginary unit, but also used as subscript
$n_j n_k$	=	Component of unit normal vector in DOF $j$ and DOF $k$
$S_0$	=	Mean wetted surface of body
$P$	=	Hydrodynamic pressure
$u v w$	=	Water particle velocity in $x$ -, $y$ - and $z$ -direction
$a_x a_y a_z$	=	Water particle acceleration in $x$ -, $y$ - and $z$ -direction
<b>M</b>	=	Mass matrix
<b>A</b> ( $\omega$ )	=	Added mass matrix
<b>B</b> ( $\omega$ )	=	Potential damping matrix
<b>C</b>	=	Stiffness matrix
$A_{kj}$	=	Added mass in DOF $k$ due to motion in DOF $j$
$B_{kj}$	=	Potential damping in DOF $k$ due to motion in DOF $j$
$A_N^{2D}$	=	Two-dimensional added mass, normal to longitudinal axis of body
$A_N^{3D}$	=	Three-dimensional added mass, normal to longitudinal axis of body
$C_m$	=	Mass coefficient
<b>U</b> <sub>rel</sub>	=	Relative velocity vector
<b>U</b> <sub>∞</sub>	=	Ambient velocity vector
<b>u</b> <sub><math>i</math></sub>	=	Velocity vector of node $i$
<b>U</b> <sub>n</sub>	=	Normal projection of relative velocity vector
<b>û</b>	=	Unit vector in direction of relative velocity
<b>n</b>	=	Initial unit normal vector
<b>ñ</b>	=	Unit normal vector for relative velocity
<b>ñ</b> <sub>a</sub>	=	Unit normal vector for water particle acceleration
<b>t</b>	=	Initial unit tangential vector
<b>t̂</b>	=	Unit tangential vector for relative velocity
<b>t̂</b> <sub>a</sub>	=	Unit tangential vector for water particle acceleration
<b>l̂</b>	=	Unit lift vector
<b>a</b>	=	Acceleration vector
<b>a</b> <sub>n</sub>	=	Normal acceleration vector
<b>F</b>	=	Excitation force vector
<b>M</b> <sub>Morison</sub>	=	Morison moment vector
<b>x</b>	=	Position vector

---

---

$\ddot{\eta}_1 \ddot{\eta}_2 \ddot{\eta}_3 \ddot{\eta}_4 \ddot{\eta}_5 \ddot{\eta}_6$	=	Acceleration in surge, sway, heave, roll, pitch and yaw
$F_N$	=	Normal force
$F_T$	=	Tangential force
$C_N$	=	Normal coefficient
$C_T$	=	Tangential coefficient
$C_L$	=	Lift coefficient
$U_{reduced}$	=	Velocity accounting for reduction factor
$\mathbf{x}$	=	Position vector
$r$	=	Reduction factor due to nets
$\kappa$	=	Reduction factor due to finite length
$A_{i,j}$	=	Projected area of screen
$d_w$	=	Twine diameter
$\omega_d$	=	Damped natural frequency
$T_d$	=	Damped natural period
$\omega_3$	=	Natural frequency in heave
$T_3$	=	Natural period in heave
$T_1$	=	Natural period in surge
$T_5$	=	Natural period in pitch
$\omega_{15}$	=	Natural frequency for coupled surge and pitch motion
$T_{15}$	=	Natural period for coupled surge and pitch motion
$\lambda$	=	Wave length or damping ratio
$\epsilon$	=	Wave steepness
$\delta$	=	Logarithmic decrement
$h$	=	Water depth or height of square cross-section
$A_R$	=	Amplitude of reflected waves
$A_T$	=	Amplitude of transmitted waves
$\bar{F}_i$	=	Mean wave-drift force
$U_{rel}$	=	Relative velocity
$F_I$	=	Inertia forces
$\Delta$	=	Mass displacement
$U_M$	=	Velocity amplitude of oscillatory flow
$\mathbf{B}_v$	=	Viscous damping matrix
$\mathbf{F}_{Morison}$	=	Morison force vector
$\mathbf{F}_D$	=	Drag force vector
$\mathbf{F}_L$	=	Lift force vector
$\mathbf{F}_{Diff}$	=	Diffraction force vector
$\mathbf{F}_{FK}$	=	Froude-Kriloff force vector
$\mathbf{s} \dot{\mathbf{s}}$	=	State variable vector and derivative of the state variable vector
$\phi_0^{steady}$	=	Velocity potential for non-separated steady flow
$\mathbf{r}$	=	Position vector
$\tau$	=	Time-delay between two signals
$t$	=	Time
$a$	=	Radius
$u_t$	=	Response peak at time $t$
$\beta$	=	Wave propagation direction

---

---



# Chapter 1

## Introduction

In recent years several new concepts for producing salmonids have been introduced as a result of the granting of development licenses. Between 20th November 2015 and 17th November 2017, the Norwegian Directorate of Fisheries allowed companies to apply for development licenses (Norwegian Directorate of Fisheries, 2018). Meaning that companies might be granted licences to produce a larger biomass of salmonids, if they can present a new concept for producing salmonids that represents substantial innovation. Specifically concerning their solutions towards challenges of the Norwegian salmon industry, such as salmon lice, escape of salmon, limited coastal production locations and waste management of salmon feces, to mention a few.

Consequently, several new concepts for producing salmonids were granted development licences, many of which are utilizing and/or being inspired by technology from the offshore oil and gas industry. Some of these concepts involve the combination of large-volume structures and nets moored offshore. There has not been built structures like this in the past and little work has been done in terms of studying such structures, thus the need for more knowledge on the topic arises.

The objective of this project is therefore to study an example of a slack moored fish farm, where the fish farm consists of a large-volume spar in the centre encircled by an octagonal framework, to which net panels are attached. The fish farm will be studied in pure current and in regular waves, however not in combination.

In current, it is of interest to find out how the total drag is changed with nets, as opposed to without nets. Further it is of interest to see how the presence of the center spar affects the forces on the nets, as well as looking into how the flow is influenced by the many net-panels. To try and answer these questions towing tests are performed on a physical model of the fish farm, as well as calculations on a numerical model are carried out. In both the experiments and in the calculations the fish farm will be studied with and without nets.

These two configurations will also be used when the fish farm is studied in regular waves. In waves it is desirable to find out how the response of the large-volume centre spar and surrounding framework is affected when nets are present, compared to without nets. Further the importance of considering diffraction around the centre spar will be examined numerically, by comparing the response when nets and columns are exposed to a diffracted wave pattern versus undisturbed waves. The influence of diffraction on the forces acting on the net-panels will also be studied numerically.

## Literature Review

As mentioned in the introduction, not much have been done in terms of studying structures consisting of nets and large-volume components in combination. However there has been done quite a lot of work on these topics separately.

Large-volume structures will experience diffraction, meaning that the incident waves are greatly disturbed due to the presence of the body. The diffraction theory for water waves was first presented by MacCamy and Fuchs (1954). Here an analytical solution of the combined diffracted and incident velocity potential was found for a bottom-fixed vertical cylindrical pile in finite water depth.

However not all offshore structures are cylindrical and one should be able to analyse arbitrary body shapes. As a result a numerical method for analysing arbitrary three-dimensional bodies was introduced a couple years later by Hess and Smith (1962). This is what today often is referred to as panel methods and is widely used for studying large-volume structures. The principle of this method was to use source formulation and describing the body in terms of several flat quadrilateral panels, with constant source strength on each panel. By imposing boundary conditions on the body surface, a system of linear equations appear, making it possible to solve for the source strength on each panel and thereafter obtain the velocity potential. Depending on the boundary conditions imposed on the body, it was then possible to solve both the diffraction and the radiation problem for an arbitrary three-dimensional body.

Net structures on the other hand, is something that has been studied a lot in more recent years, as the aquaculture industry has grown both domestically and internationally, in addition to the fact that many new fish farm concepts have emerged.

The effect of reduction of flow velocities through nets in current was examined by Løland (1991). Based on both experimental and theoretical work he managed to derive formulas for the reduction of flow through net-panels. This topic was studied further by Zhao et al. (2013), using CFD to analyse a system of several net cages. It was found that the velocity reduction between to cages did not vary significantly as a function of the distance between cages and the results obtained for the flow reductions were in compliance with Lølands formula. It was further found that the flow velocity around the cages were 1-10% greater than the incoming flow and increased as the number of aligned cages increased.

A screen-type load model for describing the viscous forces acting on nets both in current and in waves was outlined by Kristiansen and Faltinsen (2012) and proved to yield satisfactory results in current, and emerged as a less computationally expensive alternative to CFD. This model was further applied to analyse a single traditional fish cage in waves and current by Shen et al. (2018) and managed to demonstrate satisfactory agreement between numerical and experimental results.

As mentioned initially little has been done to study the combined problem of diffraction and nets. However Shen et al. (2019) did study a well boat moored to a fish cage in current. It was found that the effect of the well boat on the inflow acting on the fish cage was non-negligible. Thus indicating that the presence of a large-volume structure in the vicinity of nets, might in fact matter for the forces acting on the nets in waves as well.

## Theoretical Background

In this chapter the theory that was considered relevant for the model analyzed in this thesis will be covered. The model studied consisted of a large-volume spar encircled by a framework of columns and several net panels. Figure 5.2a and 5.2b provides pictures of the model both with and without nets. Since the fish farm consists of components with very different main dimensions and geometry, several different hydrodynamic phenomena have to be taken into account, both in regular waves and in current.

The spar for instance, might be categorized as large-volume for a certain range of wave periods. When exposed to incoming waves in that particular range, the spar will cause wave diffraction and reflection. In addition for longer wave periods, and in pure current for that matter, the spar will force the flow to move around it, thus affecting the inflow on the surrounding nets and columns.

For the columns on the other hand, drag and inertia forces have to be considered when exposed to waves, and these forces are further likely to be  $KC$ -number dependent. The relative importance of the different load types can be seen in Figure 3.1. When considering the net-panels in regular waves, the forces acting on them will be completely dominated by drag and viscous effects. Furthermore one have to consider speed-up between the twines of the net. In addition when exposed to current only, the solidity of the nets will also result in reduction of the flow-speed behind the nets, as well as some of the flow globally, will be forced to move on the outside of the entire structure.

To summarize, there have to be made distinctions between the different structural components. In current differences in Reynolds number must be considered, while in waves differences in load-type and  $KC$ -number have to be taken into account as well. Furthermore, both in current and in waves, it is necessary to consider how certain parts of the structure might influence the rest of the structure globally, for instance with regards to their effect on the flow surrounding the entire structure.

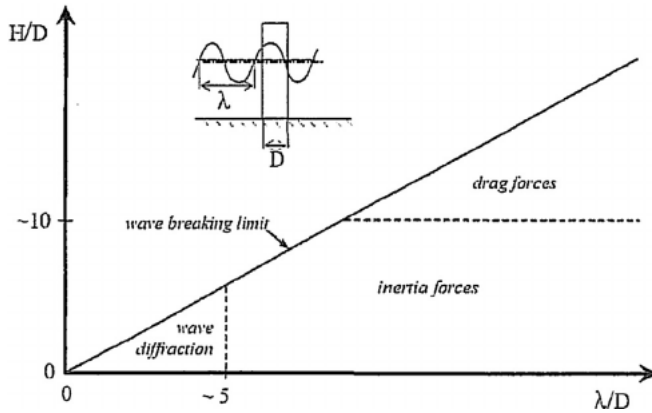


Figure 3.1: Relative importance of diffraction, inertia and drag (Faltinsen, 1998).

### 3.1 Viscous loads in steady current

A structure exposed to steady current will experience drag forces, both as a result of shear-forces between the body-surface and the fluid, and because of flow separating from the body. Separation of the flow from the body results in a high pressure zone in the front of the body and a low pressure zone at the aft, thus a net force will be acting on the body in the direction of the flow (Faltinsen, 1998). The relative importance of these two effects will depend on the shape of the body. For a streamlined body, skin-friction will be one of the main contributions to the drag force, while for a blunt body, separation will be most influential. The drag force acting on a body in a steady current is often described by,

$$F_D = \frac{1}{2} \rho C_D U^2 A, \quad (3.1)$$

where  $\rho$  is the density of the fluid,  $C_D$  is the drag coefficient,  $U$  is the velocity of the fluid flow and  $A$  is the projected area of the body as seen from the fluid. The drag coefficient  $C_D$  in steady current will vary as a function of the Reynolds number. The relationship between the drag coefficient for a smooth circular cylinder and the Reynolds number can be seen in Figure 3.2a. The Reynolds number is a non-dimensional number that describes the ratio between viscous forces and inertial forces, and is commonly expressed as,

$$Re = \frac{UD}{\nu} \quad (3.2)$$

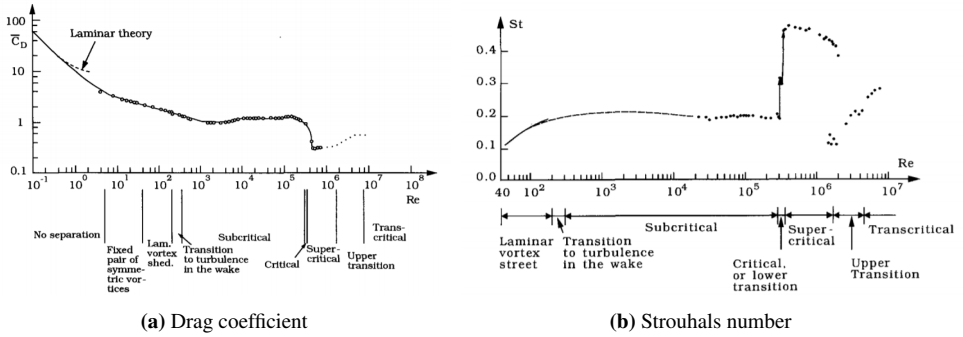
where  $U$ ,  $D$  and  $\nu$  are respectively the characteristic free-stream velocity, characteristic body length and kinematic viscosity of the fluid. The Reynolds number provides information regarding the characteristics of the flow around an object subjected to steady inflow (Sumer and Fredsøe, 2006). These characteristics relates to the wake behind the body, vortex shedding pattern and boundary layer, as seen in Figure 1. For sufficiently high Reynolds numbers vortices will be shed from the body, while for very low Reynolds numbers the flow will not even separate from the body.

Non-separated planar flow around a circular cylinder can be described using potential flow theory and an analytical expression for the velocity potential of non-separated steady flow has been presented by Faltinsen (1998). This expression takes the following form using Cartesian coordinates:

$$\phi_0^{steady} = U \left( 1 + \frac{R^2}{x^2 + y^2} \right) x \quad (3.3)$$

$U$  and  $R$  are respectively the free-stream velocity and the radius of the cylinder. Furthermore, as for any potential flow, the velocity field is found from spatial derivation of the velocity potential:

$$U_x = \frac{\partial \phi}{\partial x}, \quad U_y = \frac{\partial \phi}{\partial y} \quad (3.4)$$



**Figure 3.2:** Drag coefficient and Strouhals number of a smooth circular cylinder at different Reynolds numbers (Sumer and Fredsøe, 2006).

As mentioned above, depending on the Reynolds number, there might be created vortices in the wake behind the body as the flow separates. Meaning that Equation 3.1 does not describe the entire picture of the forces acting on a structure in steady current. When vortices are shed alternately on each side of the body, oscillatory forces will act in the direction of the inflow and perpendicular to the inflow. Thus culminating in a drag force oscillating with twice the vortex shedding frequency around the mean value described in Equation 3.1, in addition to a lift force oscillating with the vortex shedding frequency around a zero mean (Faltinsen, 1998). The vortex shedding frequency is usually found from the Strouhals number, which for a circular cylinder the Strouhals number is defined by,

$$St = \frac{f_v D}{U}, \quad (3.5)$$

where  $f_v$  is the vortex shedding frequency. Further the Strouhals number is Reynolds number dependent as seen in Figure 3.2b. Both the in-line and cross-flow oscillations might excite resonance, resulting in vortex induced vibration for flexible structures or alternatively vortex induced motions for rigid bodies.

This typically occurs for reduced velocities ( $U_R$ ) ranging from 5 to 7, resulting in a phenomena called lock-in, where the vortex shedding frequency locks into the natural frequency of the structure (Faltinsen, 1998). The reduced velocity is defined as,

$$U_R = \frac{U}{f_n D}, \quad (3.6)$$

where  $f_n$  is the natural frequency in surge/sway measured in  $Hz$ . The theory mentioned so far in this section mainly concerns a single structural element, that does not interact with other structural elements.

Structural interaction is however something that has to be considered when dealing with nets-structures, as the twines in the net might be treated equivalent to several small cylinders in close proximity to one another organized in a mesh. As a result the drag force presented in Equation 3.1 has to be adjusted in order to account for inflow angle, solidity and speed-up between twines. In the most simple case the drag force acting on a net-panel, with inflow angle  $\theta = 0$ , might be found by,

$$F_D = \frac{1}{2} \rho C_D^{c.c} U^2 A_{net}, \quad (3.7)$$

where  $A_{net}$  is the projected area of the net,  $U$  is the fluid velocity and  $C_D^{c.c}$  is the drag coefficient for a circular cylinder. In this case speed-up between twines is not considered and the solidity is assumed to be very small. This however can be taken care of by introducing a new velocity based on conservation of mass,

$$U_s = \frac{U}{1 - S_n}, \quad (3.8)$$

where  $S_n$  is the solidity of the net. According to Lader (2019) the solidity can be defined as,

$$S_n = \frac{A_{net}}{A}. \quad (3.9)$$

where  $A$  is the total area enclosed by the net-panel. Applying these formulations results in the following expression for the drag force:

$$F_D = \frac{1}{2} \rho C_D^{c.c} U_s^2 A_{net} = \frac{1}{2} \rho C_D^{c.c} \frac{S_n}{(1 - S_n)^2} U^2 A, \quad (3.10)$$

However Equation 3.10 does not account for different inflow angles and has proven to overestimate the drag, according to Kristiansen and Faltinsen (2012), who instead proposed a screen-type load model generalizing the drag force on nets to be valid for arbitrary inflow angles. The screen-type load model has therefore been used in this thesis for calculating the drag forces acting on nets, both in current and in waves. A detailed description of the screen-type load model is provided in Section 3.2.11.



## 3.2 Wave loads on nets, slender elements and large-volume structures

In the following sections the equations of motion for the fish-farm in waves will be established. As a result theory regarding the loads acting on nets, slender elements and large-volume structures and how these loads fit into the equations of motion, will be presented. However first the coordinate system used and the degrees of freedom needed to describe a rigid body moving in waves will be defined.

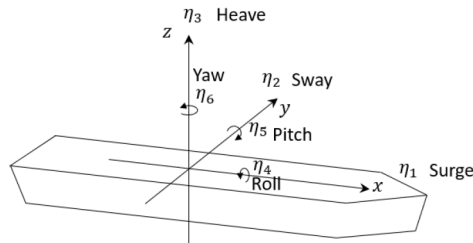
### 3.2.1 Definition of coordinate system and DOFs

In hydrodynamic problems it is quite convenient to start off with defining the coordinate system, both in terms of the location of origo and concerning the positive direction of the axes. Furthermore one must assess whether the structure studied should be considered rigid or flexible. There will be quite different degrees of freedoms to consider depending on the type of structure/problem that is examined. It is therefore important to define degrees of freedom that are able to describe the structure in the best possible manner.

In the seakeeping problem studied in this thesis, a rigid body was assumed. This implies that deformation of the net-panels was neglected, which can be justified as the net-panels were quite stiff, in addition to being tensioned on every side. When assuming a rigid body it is known that the motion of every point on the body might be described in terms of six degrees of freedom (DOF). Three translational DOF and three rotational. Translation along the  $x$ -,  $y$ - and  $z$ -axis are referred to as respectively surge ( $\eta_1$ ), sway ( $\eta_2$ ) and heave ( $\eta_3$ ). Rotation around the  $x$ -,  $y$ - and  $z$ -axis on the other hand are referred to as roll ( $\eta_4$ ), pitch ( $\eta_5$ ) and yaw ( $\eta_6$ ). According to Greco (2018), the motion of any given point on the body, assuming small motions, can then be described by,

$$\mathbf{s} = (\eta_1 + z\eta_5 - y\eta_6)\mathbf{i} + (\eta_2 - z\eta_4 + x\eta_6)\mathbf{j} + (\eta_3 + y\eta_4 - x\eta_5)\mathbf{k}, \quad (3.11)$$

where  $\mathbf{i}$ ,  $\mathbf{j}$  and  $\mathbf{k}$  are unit vectors pointing in the positive direction of the  $x$ -,  $y$ - and  $z$ -axis respectively, while  $x$ ,  $y$  and  $z$  provides the Cartesian coordinates of the point considered. An illustration of the degrees of freedom mentioned and their positive directions is provided in Figure 3.3.



**Figure 3.3:** Definition of coordinate system and degrees of freedom (Bachynski et al., 2019).

From the figure above it should be noted that the coordinate system and the positive direction of the six DOF follow the right-hand rule. Further it is stressed that the six DOF is defined in order to describe the motion of origo in the coordinate system. In hydrodynamic problems origo is usually located at the undisturbed free-surface at the centre of the body and this is where the coordinate system has been placed in this project. Using origo as the reference point and having it located at the free-surface, as opposed to at the centre of gravity, has some important implications, when it comes to the equations of motion. What these implication are and why it is crucial to be consistent with the use of reference point will be explained in the next section.

### 3.2.2 Equations of motion

In order to be able to analyze the dynamic behaviour of a structure, equations describing its motions have to be established. The equations of motion for the translational degrees of freedom, might be deduced from Newtons second law, by considering the entire mass of the structure to be represented by a single point mass located at the centre of mass. The equations of motions for the rotational degrees of freedom on the other hand are described by Eulers equations.

The aforementioned importance of being consistent with respect to the reference point comes into play when the coordinate system is located at a point that is not the centre of mass. For instance when origo is located straight above the centre of mass at the still waterline, Newtons second law in surge will be described as,

$$F_1 = Ma_1^{cm} = M(\ddot{\eta}_1 + z_G\ddot{\eta}_5) = M\ddot{\eta}_1 + Mz_G\ddot{\eta}_5, \quad (3.12)$$

where  $M$  is the mass,  $a_1^{cm}$  is the acceleration of the centre of mass along the  $x$ -axis,  $z_G$  is the vertical position of the centre of gravity,  $\ddot{\eta}_1$  is the acceleration in surge and  $\ddot{\eta}_5$  is the rotational acceleration in pitch. If instead the coordinate system had been located at the centre of mass, Newtons second law in surge would simply be,

$$F_1 = M\ddot{\eta}_1. \quad (3.13)$$

When it comes to the pitch motion, having the coordinate system located at the centre of mass, Eulers equation is just,

$$F_5^{cm} = I_{55}^{cm}\ddot{\eta}_5, \quad (3.14)$$

where  $I_{55}^{cm}$  and  $F_5^{cm}$  are respectively the moment of inertia in pitch and the sum of the moments calculated about the centre of mass. If instead the moments are summed about origo, Eulers equation then states

$$F_5^{origo} = I_{55}^{cm}\ddot{\eta}_5 + Ma_1^{cm}z_G = \underbrace{(I_{55}^{cm} + Mz_G^2)}_{I_{55}^{origo}}\ddot{\eta}_5 + Mz_G\ddot{\eta}_1. \quad (3.15)$$

Thus it is realized, that if one decides to express Newtons second law as in Equation 3.12, one must then use Equation 3.15 to describe the rotation. Alternatively if Newtons second law is expressed using Equation 3.13, then Equation 3.14 should be used for the rotation. The importance of being consistent with the equations used, should therefore be clear.

Going back to the equations of motion for a body in water. It is known that the system that is going to be analyzed will have stiffness forces trying to move the body back to its equilibrium position. There will be two main contributions to the stiffness, one will be from the change in hydrostatic pressure as the body moves out of equilibrium and the other will be due to the mooring system. There will also be energy will leaving the system, thus damping is present. Some of this energy will go to the generation of waves, which leads to radiation/potential damping, while some energy will be transformed into heat due to viscous effects, resulting in the presence of viscous damping. Furthermore the structure will have hydrodynamic added mass connected with it, as water particles will be accelerated as the body accelerates. The terms mentioned so far might be categorized as the reaction forces experienced by the structure.

In order for reaction forces to exist, the body has to experience some sort of excitation, which in this case will be provided by regular waves. For large-volume structures the main excitation will come from Froude-Krillof and diffraction forces. For more slender structures diffraction is no longer of importance, but in this case there will be inertia forces and drag forces, which might be calculated by Morison's equation. Lastly for nets it is expected that drag will be the dominating force and neither diffraction nor inertia forces will be of importance. By applying Newtons second law and using matrix notation the system of equations describing the motions of the fish farm will take the following form:

$$(\mathbf{M} + \mathbf{A}(\omega))\ddot{\eta} + \mathbf{B}(\omega)\dot{\eta} + \mathbf{B}_v\dot{\eta}|\dot{\eta}| + \mathbf{C}\eta = \underbrace{\mathbf{F}_{Morison}}_{Columns} + \underbrace{\mathbf{F}_{Diff} + \mathbf{F}_{FK}}_{Spar} + \underbrace{\mathbf{F}_D + \mathbf{F}_L}_{Nets} \quad (3.16)$$

The terms on the left-hand side  $\mathbf{M}$ ,  $\mathbf{A}(\omega)$ ,  $\mathbf{B}(\omega)$ ,  $\mathbf{B}_v$  and  $\mathbf{C}$  are in the general case of 6 DOF motions, matrices of dimension  $6 \times 6$  and will be referred to as mass matrix, frequency dependent added mass matrix, frequency dependent potential damping matrix, viscous damping matrix and stiffness matrix, respectively.  $\ddot{\eta}$ ,  $\dot{\eta}$  and  $\eta$  are vectors containing accelerations, velocities and displacements in 6 degrees of freedom. The terms on the right-hand side are vectors of the different force contributions.  $\mathbf{F}_{Morison}$  are forces provided by Morison's equation and will be used to describe the forces acting on the columns.  $\mathbf{F}_{Diff}$  and  $\mathbf{F}_{FK}$  are diffraction forces and Froude-Krillof forces which will act on the centre spar, however it should be mentioned that for sufficiently long waves drag should also be considered for the spar. Lastly  $\mathbf{F}_D$  and  $\mathbf{F}_L$  are the drag and lift forces acting on the nets. A more detailed description of the terms presented in Equation 3.16 will be provided in the sections to follow. As mentioned initially Equation 3.16 assumes regular waves, but if instead the excitation were provided by irregular waves, other terms such as slowly-varying forces and possibly wave-drift damping would also have to be considered. It should be stressed that in irregular waves slow-drift forces are of significant importance as they might excite resonant motions in surge, for a slack moored structure. However this is not studied in this project and won't be elaborated any further.

### 3.2.3 Mass matrix

First off, the mass matrix  $\mathbf{M}$  presented in Equation 3.16 will be considered. For a general non-symmetric structure without symmetric mass-distribution, there will be several inertia coupling terms (Bachynski et al., 2019). However the structure under consideration of this project have two planes of symmetry, the  $xz$ -plane and the  $yz$ -plane. Further assuming the structure to be ballasted symmetrically according to the aforementioned geometrical planes of symmetry, it is realized that several of the coupling terms will vanish. The mass matrix will then take the following form:

$$\mathbf{M} = \begin{bmatrix} M & 0 & 0 & 0 & Mz_G & 0 \\ 0 & M & 0 & -Mz_G & 0 & 0 \\ 0 & 0 & M & 0 & 0 & 0 \\ 0 & -Mz_G & 0 & I_{44} & 0 & 0 \\ Mz_G & 0 & 0 & 0 & I_{55} & 0 \\ 0 & 0 & 0 & 0 & 0 & I_{66} \end{bmatrix} \quad (3.17)$$

$M$  and  $z_G$  are respectively the total dry mass of the structure and the vertical position of the center of gravity.  $I_{44}$ ,  $I_{55}$  and  $I_{66}$  on the other hand are the moments of inertia in roll, pitch and yaw. As discussed in Section 3.2.2 it is noted that depending on your choice of reference point, the coupling terms present in the mass matrix above might also disappear. However since origo is assumed to be located at the undisturbed free-surface, this won't happen in this case. The moments of inertia presented in the mass matrix are given by,

$$I_{44} = \int_B (y^2 + z^2)dm, \quad I_{55} = \int_B (x^2 + z^2)dm, \quad I_{66} = \int_B (x^2 + y^2)dm, \quad (3.18)$$

where  $x$ ,  $y$  and  $z$  are understood to be the coordinates of the infinitely small mass  $dm$  according to the reference point chosen (Bachynski et al., 2019). Often in practical applications, as for ballasting purposes, the integration is replaced by a sum of point masses ( $M_i$ ) distributed around the body:

$$I_{44} = \sum_{i=1}^N (y_i^2 + z_i^2)M_i \quad I_{55} = \sum_{i=1}^N (x_i^2 + z_i^2)M_i \quad I_{66} = \sum_{i=1}^N (x_i^2 + y_i^2)M_i \quad (3.19)$$

### 3.2.4 Stiffness matrix

As mentioned previously, for a moored structure there will be two principal contributions to the stiffness of the system. First off, there will be hydrostatic stiffness, as result of the change in hydrostatic pressure as the body is displaced. The magnitude of which will depend on both the geometry and mass distribution of the structure. Secondly there will be stiffness due to the mooring system.

For a body symmetric about both the  $xz$ -plane and the  $yz$ -plane the hydrostatic pressure will contribute with stiffness terms in heave, roll and pitch. According to (Faltinsen, 1998) these terms can be found as,

$$C_{33}^{hs} = \rho g A_{wp}, \quad C_{44}^{hs} = \rho g \nabla \overline{GM}_T, \quad C_{55}^{hs} = \rho g \nabla \overline{GM}_L, \quad (3.20)$$

where  $A_{wp}$ ,  $\nabla$ ,  $\overline{GM_T}$  and  $\overline{GM_L}$  are respectively the area of the water-plane, the displaced volume of water, the transverse metacentric height and longitudinal metacentric height. The metacentric heights are determined by,

$$\overline{GM_T} = z_B + \frac{I_{xx}}{\nabla} - z_G, \quad \overline{GM_L} = z_B + \frac{I_{yy}}{\nabla} - z_G \quad (3.21)$$

where  $z_B$ ,  $z_G$ ,  $I_{xx}$  and  $I_{yy}$  are the vertical centre of buoyancy, vertical centre of gravity, second moment of area around the  $x$ -axis and second moment of area around the  $y$ -axis. For a double symmetric structure the hydrostatic restoring in pitch and roll will be equal.

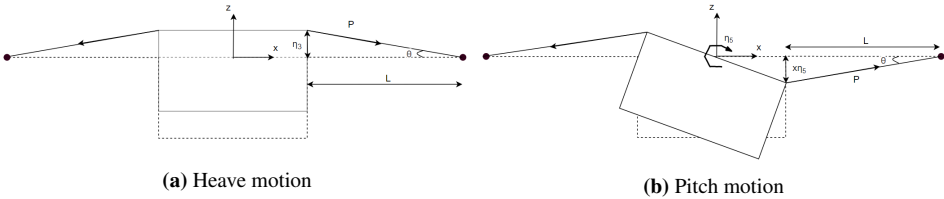
When mooring lines are present there will be additional stiffness terms. For a mooring system consisting of  $n$  mooring lines, positioned at  $(x_i, y_i)$  on the structure, angled at  $\psi_i$  with the  $x$ -axis, where each mooring line has a local stiffness of  $k_i$ , the global mooring system stiffness in surge, sway and yaw are found as described below according to Falinsen (1998):

$$C_{11}^{ms} = \sum_{i=1}^n k_i \cos^2 \psi_i \quad (3.22)$$

$$C_{22}^{ms} = \sum_{i=1}^n k_i \sin^2 \psi_i \quad (3.23)$$

$$C_{66}^{ms} = \sum_{i=1}^n k_i (x_i \sin \psi_i - y_i \cos \psi_i) \sin \psi_i \quad (3.24)$$

However there will be additional stiffness terms in heave, roll and pitch as well, due to the pretension of the mooring lines. For a horizontal taut mooring system, where each mooring line has pretension  $P_i$  and length  $l_i$ , and assuming small motions and neglecting the weight of the mooring lines, it is possible to deduce the terms mentioned.



**Figure 3.4:** Mooring line stiffness due to pretension.

Starting off with the heave motion, and looking at Figure 3.4a it is realized that the force acting in  $z$ -direction from a single mooring line is found as,

$$F_z = P_i \sin \theta. \quad (3.25)$$

As a result of the assumption of small motions and therefore also small angles,  $\sin \theta$  might be estimated by,

$$\sin \theta \approx \tan \theta = \frac{\eta_3}{l_i}, \quad (3.26)$$

thus the total stiffness in heave due to the mooring line pretension is given by,

$$C_{33}^{ms} = \sum_{i=1}^n \frac{P_i}{l_i}. \quad (3.27)$$

Now looking at the pitch motion from Figure 3.4b, it is obvious that there will be two moment contributions, both of which should be considered for this particular mooring system. The reason being that the largest force component has the shortest moment arm, while the smallest force component has the longest moment arm. For a single mooring line the vertical force component is given by,

$$F_z = P_i \sin \theta, \quad \text{where} \quad \sin \theta \approx \tan \theta = \frac{x_i \eta_5}{l_i}. \quad (3.28)$$

The force component in  $x$ -direction is given by,

$$F_x = P_i \cos \theta \cos \psi_i, \quad \text{where} \quad \cos \theta \approx 1. \quad (3.29)$$

Using the following moment arms  $dz = x_i \eta_5$  and  $dx = x_i$ , the total restoring moment for one mooring line is given by,

$$M_y = F_x dz + F_z dx = P_i x_i \eta_5 \cos \psi_i + P_i \frac{x_i^2}{l_i} \eta_5. \quad (3.30)$$

The total mooring system stiffness in pitch is then found as

$$C_{55}^{ms} = \sum_{i=1}^n P_i x_i \cos \psi_i + P_i \frac{x_i^2}{l_i}. \quad (3.31)$$

Similarly it can be shown that the total mooring system stiffness in roll will take the following form

$$C_{44}^{ms} = \sum_{i=1}^n P_i y_i \sin \psi_i + P_i \frac{y_i^2}{l_i}. \quad (3.32)$$

Once again it is noted that if the mooring system is double symmetric the stiffness in roll and pitch will be equal. The total system stiffness matrix is then obtained by adding the results from the hydrostatic stiffness and the mooring line stiffness, thus yielding the stiffness matrix provided below.

$$\mathbf{C} = \begin{bmatrix} C_{11}^{ms} & 0 & 0 & 0 & 0 & 0 \\ 0 & C_{22}^{ms} & 0 & 0 & 0 & 0 \\ 0 & 0 & C_{33}^{ms} + C_{33}^{hs} & 0 & 0 & 0 \\ 0 & 0 & 0 & C_{44}^{ms} + C_{44}^{hs} & 0 & 0 \\ 0 & 0 & 0 & 0 & C_{55}^{ms} + C_{55}^{hs} & 0 \\ 0 & 0 & 0 & 0 & 0 & C_{66}^{ms} \end{bmatrix} \quad (3.33)$$

### 3.2.5 Linear potential flow theory

Linear potential flow theory is commonly used to analyze large volume-structures in waves and is the foundation of most commercial hydrodynamic analysis software. The main assumptions of this theory is that the flow is inviscid, irrotational and incompressible (Greco, 2018). Due to the linearity of potential flow theory, the hydrodynamic problem for a floating body in waves is usually divided into two sub-problems, before taking advantage of the superposition principle by adding both solutions in order to get the complete solution.

The two problems mentioned are commonly referred to as the diffraction problem and the radiation problem. The diffraction problem concerns the wave excitation loads obtained when the body is restricted from moving and subjected to incident waves. These loads are further divided into Froude-Kriloff and diffraction loads. The radiation problem however, concerns the reaction forces/moments that are acting on the body, when it is forced to oscillate and there are no incident waves present. The hydrodynamic loads obtained from the radiation problem might be categorized as added mass, damping and restoring forces (Faltinsen, 1998).

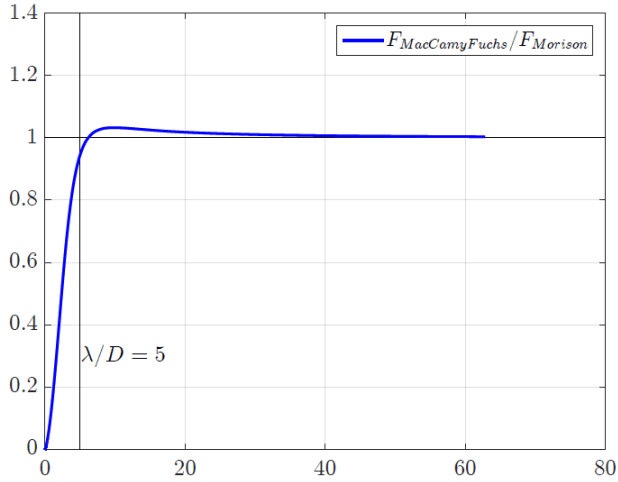
Depending on which one of the aforementioned problems you are looking at there will be different boundary conditions to consider, which will be discussed in the sections to follow. However there are some common criteria that have to be fulfilled in both cases, when using linear theory. For the linearized boundary value problem the following must be satisfied (Greco, 2018) (Bachynski et al., 2019).

- *Laplace equation*: The Laplace equation,  $\nabla^2\phi = 0$ , has to be satisfied inside the fluid domain. In short terms the Laplace equation ensures continuity, by demanding that there is no divergence in the velocity-field of the potential flow. As continuity is ensured, conservation of mass and momentum is maintained.
- *Far-field radiation condition*: States that the disturbance from the diffracted and/or radiated waves dies out far away from the body. I.e the radiated and/or diffracted waves are propagating outwards and decaying.
- *Combined free surface condition*: The equation,  $-\omega^2\phi + g\frac{\partial\phi}{\partial z} = 0$ , has to be satisfied on  $z = 0$ , ensuring both that the pressure on the free surface is equal to the atmospheric pressure and that fluid particles on the free-surface remain there.

In the next sections both the radiation and diffraction problem and the resulting forces/-moments will be discussed in greater detail.

### 3.2.6 Diffraction

As mentioned in the previous section, the diffraction problem provides the hydrodynamic forces acting when the body is fixed and exposed to incident waves. Diffraction and reflection of waves are of importance when the wavelength is short relative to the cross-sectional dimensions of the body, i.e. for large-volume structures, where the presence of the body affects the incident waves. The disturbance of the incident waves is especially relevant in this thesis, as the presence of the spar might result in speed-up, altered phases and changed direction of the flow, which in turn will be affecting the surrounding nets and columns. An often used limit for when diffraction theory should be applied is,  $\frac{\lambda}{D} < 5$ . This limit is illustrated in Figure 3.5. With respect to the centre spar in this thesis, it is found that this limit will correspond to a wave period of 0.895 s, where shorter periods will result in significant diffraction and reflection. It is also observed from Figure 3.5 that it is important to take diffraction into account in order to not overestimate the forces acting on large-volume structures, which would be the case if Morison is applied.



**Figure 3.5:** Comparison between force estimation using diffraction theory and Morison (Bachynski et al., 2019).

The diffraction theory for vertical circular cylinders was presented by MacCamy and Fuchs (1954). This theory is widely used today. The theory starts off with the incident velocity potential using complex notation,

$$\Phi_0 = \Re\{\phi_0 e^{i\omega t}\}, \quad \phi_0 = \frac{ig\zeta_a}{\omega} \frac{\cosh(k(z+h))}{\cosh(kh)} e^{-ikx}, \quad (3.34)$$

where  $\zeta_a$ , is the amplitude of the waves,  $\omega$  is the wave frequency,  $k$  is the wavenumber,  $g$  is the gravitational acceleration and  $h$  is the water depth. It is further assumed that the diffraction potential will have the same variation in  $z$ -direction as the incident wave potential, but will have a different horizontal variation.



The variation in the horizontal direction is given by the function  $\psi(x, y)$ . Further  $\psi(x, y)$  is expressed in terms of polar coordinates,  $\psi(x, y) \Rightarrow \psi(R, \theta)$ , and the diffraction potential  $\phi_7$  is required to satisfy the Laplace equation. Then it is imposed boundary conditions on the surface of the structure, such that there is zero flux of fluid through the surface. In mathematical terms the boundary condition in the diffraction problem is described by,

$$\frac{\partial \phi_7}{\partial n} = -\frac{\partial \phi_0}{\partial n}, \quad (3.35)$$

thus ensuring that the normal velocity on the boundary is zero. As a result of the boundary conditions and introducing an identity to the horizontal variation of the incident wave potential, while also having to satisfy a far-field radiation condition and the Laplace equation, it is recognized that  $\psi(R, \theta)$  can be expressed in terms of the Hankel function of second kind. Then only some unknown constants have to be determined and these are found from the boundary conditions on the surface of the body. The total potential is then given as follows,

$$\begin{aligned} \Phi_D &= \Re\{\phi_D e^{i\omega t}\}, & \phi_D &= \phi_0 + \phi_7 & (3.36) \\ \phi_D &= \frac{ig\zeta_a}{\omega} \frac{\cosh k(z+h)}{\cosh kh} \left( \sum_{m=0}^{\infty} \epsilon_m \left[ J_m(kR) - \frac{J'_m(ka)}{H_m^{(2)'}(ka)} H_m^{(2)}(kR) \right] \cos m\theta \right) & (3.37) \end{aligned}$$

It is noted that in this case  $R$  and  $\theta$  denotes the polar coordinates considered, while  $a$  is the radius of the cylinder.  $J_m$  and  $H_m^{(2)}$  are the Bessel function of first kind and the Hankel function of second kind, while the prime notation used in Equation 3.37 denotes derivation. The waves resulting from  $\phi_7$  might be considered as three dimensional waves radiating outwards in all directions from the surface of the body, much like the waves created by a stone dropped in a calm pond. Having obtained the velocity potential, the water particle velocities and accelerations can be found. In the general case of an arbitrary velocity potential,  $\phi$ , these are found as:

$$u = \frac{\partial \phi}{\partial x}, \quad v = \frac{\partial \phi}{\partial y}, \quad w = \frac{\partial \phi}{\partial z} \quad (3.38)$$

$$a_x = \frac{\partial^2 \phi}{\partial x \partial t}, \quad a_y = \frac{\partial^2 \phi}{\partial y \partial t}, \quad a_z = \frac{\partial^2 \phi}{\partial z \partial t}. \quad (3.39)$$

The total hydrodynamic pressure is found from Bernoulli's equation, neglecting the quadratic term:

$$P = \Re \left\{ -\rho \frac{\partial}{\partial t} (\phi_D e^{i\omega t}) \right\} \quad (3.40)$$

Furthermore the total horizontal force, consisting of the Froude-Kriloff force and the diffraction force is found by integrating the pressure on the mean wetted surface of the body  $S_0$  (Bachynski et al., 2019):

$$F_k = \underbrace{\int_{S_0} \Re \left\{ -\rho \frac{\partial}{\partial t} (\phi_0 e^{i\omega t}) \right\} n_k dS}_{\text{Froude-Krilloff}} + \underbrace{\int_{S_0} \Re \left\{ -\rho \frac{\partial}{\partial t} (\phi_7 e^{i\omega t}) \right\} n_k dS}_{\text{Diffraction}}, \quad k = 1, 2, \dots, 6 \quad (3.41)$$

It should be noted that the normal vector components  $n_k$ , for  $k = 4, 5, 6$  are given by:

$$[n_4, n_5, n_6] = [x, y, z] \times [n_1, n_2, n_3] \quad (3.42)$$

A point worth making when integrating the dynamic pressure from  $\phi_D$  to find the horizontal force  $F_1$ , where  $n_1 = \cos \theta$ , is the orthogonality property of  $\cos \theta$ . The result of this property is that only one term in the summation from  $m = 0$  to  $m = \infty$ , specifically  $m = 1$ , is necessary to obtain the exact horizontal force. This property is shown in the equation below.

$$\int_0^{2\pi} \cos \theta \cos m\theta d\theta = \begin{cases} \pi, & m = 1 \\ 0, & m \neq 1 \end{cases} \quad (3.43)$$

Thus if only the horizontal force is of interest, then the diffraction theory might be implemented in a computer program quite efficiently for a vertical cylinder. To get a more detailed derivation of the diffraction theory, see Appendix B.1.

### 3.2.7 Radiation

For a body moving in waves it is necessary to consider the radiation problem, where the body is forced to oscillate and no incident waves are present. The total radiation potential is found by dividing the radiation problem into six sub-problems, one for each degree of freedom, resulting in:

$$\phi_R = \sum_{j=1}^6 \phi_j \quad (3.44)$$

It is then necessary to impose boundary conditions on the body in order to ensure impermeability, i.e. there is no fluid flow through the body. Meaning that the velocity of the fluid is equal to the velocity of the body everywhere on the body. In mathematical terms this is described by,

$$\frac{\partial \phi_j}{\partial n} = V_j, \quad \text{on } S_0 \quad (3.45)$$

where  $S_0$  is the mean wetted surface of the body,  $V_j$  is the normal velocity of the body and  $\frac{\partial \phi_j}{\partial n}$  is the normal velocity of the fluid on the body (Bachynski et al., 2019).

In order to actually solve for the velocity potentials, panel methods are often used, as is the case with programs such as WAMIT (Bachynski et al., 2019). When the radiation problem is solved and the radiation potentials have been determined the added mass and damping coefficients are found from the dynamic pressure acting on the body.

$$F_{kj} = -\rho \int_{S_0} \frac{\partial \phi_j}{\partial t} n_k dS = -A_{kj} \ddot{\eta}_j - B_{kj} \dot{\eta}_j \quad j = 1, \dots, 6 \quad k = 1, \dots, 6. \quad (3.46)$$

$F_{jk}$ ,  $A_{jk}$  and  $B_{jk}$  are respectively the force, added mass and damping in degree of freedom  $k$  due to motion in degree of freedom  $j$ , while  $n_k$  is the unit normal vector component in degree of freedom  $k$ . The added mass and damping will be discussed in greater detail in the next sections.

### 3.2.8 Added mass

Added mass might be considered as a fictional hydrodynamic mass that increases the inertia of a body in water, due to acceleration of water particles around the body, as the body moves. However strictly speaking the added mass is found from the radiation problem, as mentioned in the previous section, as the hydrodynamic force acting on the structure that is  $180^\circ$  out of phase with the body acceleration (Greco, 2018).

A characteristic with the added mass obtained from the radiation problem in linear theory is that it is frequency dependent, since the water will respond differently at different frequencies of oscillation. For instance for a surface-piercing body at high frequencies, the water particles will tend to cling to the body at the free surface, while at lower frequencies the water particles at the free surface will rather disperse horizontally (Bachynski et al., 2019). When the radiation problem is solved and the radiation potentials have been determined the added mass is found as:

$$A_{kj}(\omega) = \Re \left[ \rho \int_{S_0} \phi_j n_k dS \right] \quad (3.47)$$

As a result coupling terms will appear in the cases where  $j \neq k$ . However with respect to the structure considered in this project, it is realized that several of these cross-terms goes to zero, due to the double symmetry of the fish farm. The resulting added mass matrix will therefore be as described below:

$$\mathbf{A} = \begin{bmatrix} A_{11} & 0 & 0 & 0 & A_{15} & 0 \\ 0 & A_{22} & 0 & -A_{24} & 0 & 0 \\ 0 & 0 & A_{33} & 0 & 0 & 0 \\ 0 & -A_{42} & 0 & A_{44} & 0 & 0 \\ A_{51} & 0 & 0 & 0 & A_{55} & 0 \\ 0 & 0 & 0 & 0 & 0 & A_{66} \end{bmatrix} \quad (3.48)$$

For elongated bodies, such as for the circular and square columns that make up the frame-work around the centre spar, the total added mass might be calculated from a sum of 2-dimensional added masses. Having an elongated body implies in principle that the length of the body is substantially larger than its cross-sectional dimensions. Assuming the 3D-problem as a sum of 2D-problems is justified by the fact that for an elongated body, the largest flow variation occurs in the cross-sectional plane. For flow perpendicular to the length of the body there will only be small flow variations along the its longitudinal axis, mainly due to flow moving around the ends of the body. The more elongated the body is, the less will the longitudinal flow variation matter. The result of this assumption can be summarized as follows,

$$A_N^{3D} = \int_L A_N^{2D} dl, \quad (3.49)$$

where  $A_N^{3D}$  and  $A_N^{2D}$  denotes respectively the two-dimensional and three-dimensional added mass, normal to the longitudinal axis of the body.

Strip theory is further often used in combination with the cross-flow principle. The cross flow principle states that the flow separates due to cross-flow past the body and that longitudinal flow components does not influence the transverse force on a cross-section (Faltinsen, 1998). Essentially in the context of the forces acting on the columns this means that only the flow components normal to the longitudinal axis of the body will contribute to the forces acting on it. However it should be noted that this assumption gets progressively worse as the inflow angle increases, because then the longitudinal force components become increasingly important relative to the normal component. The result of this assumption is mathematically described by,

$$A_{jk} = A_N n_j n_k, \quad (3.50)$$

where  $A_{jk}$  is the added mass in degree of freedom  $j$  as a result of motion in degree of freedom  $k$ ,  $A_N$  is the added mass assuming inflow perpendicular to the longitudinal axis of the body, while  $n_j$  and  $n_k$  are the components of the unit normal vector in respectively degree of freedom  $j$  and  $k$ .

### 3.2.9 Potential damping

Potential damping, which is often also referred to as radiation damping, is a type of linear damping, that is connected with the waves generated by a structure oscillating in a fluid. The principle behind the radiation damping is that as waves are generated, energy is dissipated from the system in the form of waves radiating/propagating away from the structure, thus damping out the motions. It should be noted that the potential damping is frequency dependent, as the capability of generating waves will vary depending on the frequency of the oscillatory motion. In the limiting cases as the frequency goes to zero and infinity respectively, it is clear that no waves will be generated and the damping goes to zero. On the other hand, when the period of oscillation is close to any natural periods and large motions are excited, then there will be generated significant waves, which are important for limiting the resonant motions.

As the names potential damping/radiation damping suggests, this type of damping is determined from the velocity potentials obtained from the radiation problem. When the radiation velocity potentials  $\phi_j$  are known, the damping coefficients are found from the following equation(Greco, 2018):

$$B_{kj}(\omega) = -\omega \Im \left[ \rho \int_{S_0} \phi_j n_k dS \right] \quad (3.51)$$

Once again it is observed that cross terms will be present when  $j \neq k$ . However, as with the added mass described previously, many of these terms will be zero for a structure with  $xz$ -plane and  $yz$ -plane symmetry. The potential damping matrix will therefore in this case take the following form:

$$\mathbf{B} = \begin{bmatrix} B_{11} & 0 & 0 & 0 & B_{15} & 0 \\ 0 & B_{22} & 0 & -B_{24} & 0 & 0 \\ 0 & 0 & B_{33} & 0 & 0 & 0 \\ 0 & -B_{42} & 0 & B_{44} & 0 & 0 \\ B_{51} & 0 & 0 & 0 & B_{55} & 0 \\ 0 & 0 & 0 & 0 & 0 & B_{66} \end{bmatrix} \quad (3.52)$$

For surface piercing large-volume structures the radiation damping will in many cases be the dominating damping contribution. For slender structures and nets on the other hand, waves will not be generated to the same extent and the majority of the damping provided will be as a result of viscous effects. The forces acting on slender structures and nets will be discussed in greater detailed in the next sections.

### 3.2.10 Wave excitation forces on slender elements

Morison's equation is often used to calculate the forces acting on slender structures with circular cross-section. For a moving vertical cylinder, the horizontal force on a strip with length  $dz$ , is determined as follows, according to Faltinsen (1998).

$$dF_1 = \frac{1}{2}\rho C_D D(u - \dot{\eta}_1)|(u - \dot{\eta}_1)|dz + \rho C_m \frac{\pi D^2}{4} a_x dz - \rho(C_m - 1)\frac{\pi D^2}{4} \ddot{\eta}_1 dz \quad (3.53)$$

Applying this to a net-structure, means using strip theory and integrating  $dF_1$  on each twine independently, thus not taking into account interaction between twines. These interactions being specifically, shading effect of downstream twines from upstream twines at large inflow angles and local speed-up between twines. Other deficiencies is that it highly over-predicts the drag force for large inflow angles( $\theta$ ) and thus can't be justified for  $\theta > 45^\circ$  (Kristiansen and Faltinsen, 2012). For the circular and square columns in the framework on the other hand Morison might provide an accurate prediction of the forces and moments acting on them.

In this project Equation 3.53 is altered slightly in order to account for heave and pitch motion of the body, in addition to different inclinations of the columns. First off, the last term in Equation 3.53, which accounts for the added mass of the columns, is moved to the left side of Equation 3.16. Further the relative velocity,  $(u - \dot{\eta}_1)$ , is replaced by  $\mathbf{U}_{\text{rel}}$  providing the relative velocity at each discretized point.

$$\mathbf{U}_{\text{rel}} = \mathbf{U}_{\infty} - \mathbf{u}_i, \quad (3.54)$$

where  $\mathbf{U}_{\infty}$  is the velocity vector of the ambient flow found from the velocity potential considered and  $\mathbf{u}_i$  is the velocity of the discretized point  $i$ . By assuming that the cross flow principle holds, only the normal component of the relative flow is considered and is found by,

$$\mathbf{U}_n = (\mathbf{U}_{\text{rel}} \cdot \hat{\mathbf{n}})\hat{\mathbf{n}}, \quad (3.55)$$

where  $\hat{\mathbf{n}}$  is the unit normal vector of the columns. The normal vectors are defined in terms of the tangential unit vectors  $\hat{\mathbf{t}}$  of the columns and the relative velocity vectors  $\mathbf{U}_{\text{rel}}$ :

$$\hat{\mathbf{n}} = \frac{\mathbf{U}_{rel} - (\mathbf{U}_{rel} \cdot \hat{\mathbf{t}})\hat{\mathbf{t}}}{|\mathbf{U}_{rel} - (\mathbf{U}_{rel} \cdot \hat{\mathbf{t}})\hat{\mathbf{t}}|} \quad (3.56)$$

The tangential unit vectors were determined based off of the discretized geometry of the columns, but also in terms of the relative velocity vectors in order to get the correct direction. Initially the tangential vectors are found by subtracting the position vector of two adjacent points and dividing by the length of the resulting vector:

$$\mathbf{t} = \frac{\mathbf{x}_{i+1} - \mathbf{x}_i}{|\mathbf{x}_{i+1} - \mathbf{x}_i|}, \quad (3.57)$$

Here  $\mathbf{x}_{i+1}$  and  $\mathbf{x}_i$  denotes vectors containing the Cartesian coordinates of two neighbouring points. Finally  $\hat{\mathbf{t}}$  is found as,

$$\hat{\mathbf{t}} = \text{sign}(\mathbf{U}_{rel} \cdot \mathbf{t})\mathbf{t}, \quad (3.58)$$

thus ensuring that the tangential unit vector and consequently the normal velocity vector at all times points in the direction of the relative velocity. Similarly as with the drag term, only the normal component of the acceleration vector, denoted  $\mathbf{a}_n$ , is used to find the contribution of the inertia force, therefore using,

$$\mathbf{a}_n = (\mathbf{a} \cdot \hat{\mathbf{n}}_a)\hat{\mathbf{n}}_a, \quad (3.59)$$

where  $\mathbf{a}$  is the water particle acceleration vector and  $\hat{\mathbf{n}}_a$  is the normal vector defined in terms of the water-particle acceleration vector. The procedure of determining  $\hat{\mathbf{n}}_a$  is quite similar as for  $\hat{\mathbf{n}}$ . First the tangential vector is forced to point in the direction of the acceleration,

$$\hat{\mathbf{t}}_a = \text{sign}(\mathbf{a} \cdot \mathbf{t})\mathbf{t}. \quad (3.60)$$

Thereafter the normal vector for the water particle acceleration is found as:

$$\hat{\mathbf{n}}_a = \frac{\mathbf{a} - (\mathbf{a} \cdot \hat{\mathbf{t}}_a)\hat{\mathbf{t}}_a}{|\mathbf{a} - (\mathbf{a} \cdot \hat{\mathbf{t}}_a)\hat{\mathbf{t}}_a|} \quad (3.61)$$

Combining both strip theory and the cross-flow principle, assuming that the framework is divided into  $N$  strips, the total force acting on the framework is found as described below:

$$\mathbf{F}_{Morison} = \sum_{i=1}^N \left( \frac{1}{2} \rho C_D |\mathbf{U}_n|^2 A_i \hat{\mathbf{n}} + \rho C_m V_i \mathbf{a}_n \right) \quad (3.62)$$

$A_i$  and  $V_i$  are respectively the projected area and the volume of strip  $i$ . It is important to note that the mass coefficient ( $C_m$ ) and the drag coefficient ( $C_D$ ) used should be defined based on flow perpendicular to the length of the column. Further the total moment acting is found from,

$$\mathbf{M}_{Morison} = \sum_{i=1}^N (\mathbf{r}_i \times \mathbf{F}_i), \quad (3.63)$$

where  $\mathbf{F}_i$  is the force acting on one single strip, as described inside the parenthesis of Equation 3.62 and  $\mathbf{r}_i$  is the position vector containing the coordinates of the centre of the strip.

### 3.2.11 Wave excitation forces on nets

To calculate the drag and lift forces acting on nets, a screen-type load model is often used. In a screen-type load model, the geometry of the net is represented by several screens that the load acts on. This load model might be used in combination with deformation of the nets, but since the net-panels used in this project were tensioned and fixed on every side, deformation was neglected. The screen-type load model used in this project was presented by Kristiansen and Faltinsen (2012) and will be outlined in detail throughout this section. The idea of this model is to take into account local speed-up between twines, shading effects and generalizing the calculated forces to hold for arbitrary inflow angles.

The starting point is the formula for drag force on a net provided in Equation 3.10. Then the lift and drag forces are generalized for arbitrary inflow angles( $\theta$ ), based on the normal and tangential drag force. The mathematical relation between the normal and tangential force and the global  $x$ -,  $y$ - and  $z$ - component of the force is given by,

$$\mathbf{F} = \begin{bmatrix} F_x \\ F_y \\ F_z \end{bmatrix} = F_N \hat{\mathbf{n}} + F_T \hat{\mathbf{t}}, \quad F_N = \frac{1}{2} \rho A C_N |\mathbf{U}_{rel}|^2, \quad F_T = \frac{1}{2} \rho A C_T |\mathbf{U}_{rel}|^2. \quad (3.64)$$

The normal and tangential coefficients,  $C_N$  and  $C_T$ , are found as described in Equation 3.77 and 3.75. The normal vector of a screen is found from,

$$\hat{\mathbf{n}} = \text{sign}(\mathbf{U}_{rel} \cdot \mathbf{n}) \mathbf{n}, \quad \text{where } \mathbf{n} = \frac{\mathbf{s}_1 \times \mathbf{s}_2}{|\mathbf{s}_1 \times \mathbf{s}_2|}. \quad (3.65)$$

The equations above assume that the vectors  $\mathbf{s}_1$  and  $\mathbf{s}_2$  are orthogonal to one another, which will be the case for the fish farm in this project.  $\mathbf{s}_1$  and  $\mathbf{s}_2$  can be found based on the geometry of the net as,

$$\mathbf{s}_1 = \frac{\mathbf{x}_{i+1,j} - \mathbf{x}_{i,j}}{|\mathbf{x}_{i+1,j} - \mathbf{x}_{i,j}|} \quad \text{and} \quad \mathbf{s}_2 = \frac{\mathbf{x}_{i,j+1} - \mathbf{x}_{i,j}}{|\mathbf{x}_{i,j+1} - \mathbf{x}_{i,j}|}, \quad (3.66)$$

where  $\mathbf{x}_{i,j}$  is the position of the node  $i, j$ . An illustration of the vectors are provided below.

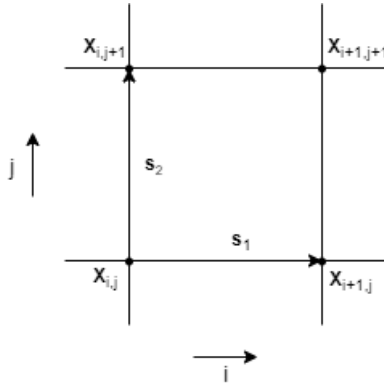


Figure 3.6: Illustration of  $\mathbf{s}_1$  and  $\mathbf{s}_2$ .

The tangential unit vector  $\hat{\mathbf{t}}$  is found by subtracting the the normal component of the relative velocity vector from the relative velocity vector and normalizing:

$$\hat{\mathbf{t}} = \frac{\mathbf{U}_{rel} - (\hat{\mathbf{n}} \cdot \mathbf{U}_{rel})\hat{\mathbf{n}}}{|\mathbf{U}_{rel} - (\hat{\mathbf{n}} \cdot \mathbf{U}_{rel})\hat{\mathbf{n}}|} \quad (3.67)$$

The relative velocity vector is found from,

$$\mathbf{U}_{rel} = \mathbf{U}_{\infty} - \mathbf{u}_{i,j}, \quad (3.68)$$

where  $\mathbf{U}_{\infty}$  is the ambient flow velocity vector and  $\mathbf{u}_{i,j}$  is the velocity of node  $i, j$ . An illustration of  $\mathbf{U}_{rel}$ , together with  $\hat{\mathbf{t}}$  and  $\hat{\mathbf{n}}$  is provided in Figure 3.7.

There is also possible to describe the forces on a screen locally in terms of the drag and lift direction as seen on the right side of Figure 3.7. The drag direction is then defined as the direction of  $\hat{\mathbf{u}}$  which is a unit vector pointing in the direction of the relative velocity.

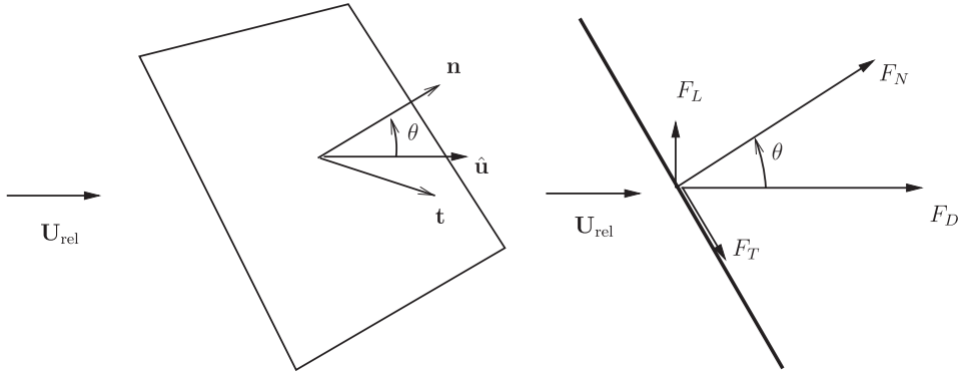
$$\hat{\mathbf{u}} = \frac{\mathbf{U}_{rel}}{|\mathbf{U}_{rel}|} \quad (3.69)$$

The lift direction given by the unit vector  $\hat{\mathbf{l}}$ , which is defined in terms of  $\hat{\mathbf{n}}$  and  $\hat{\mathbf{u}}$  as follows:

$$\hat{\mathbf{l}} = \frac{\hat{\mathbf{u}} \times (\hat{\mathbf{n}} \times \hat{\mathbf{u}})}{|\hat{\mathbf{u}} \times (\hat{\mathbf{n}} \times \hat{\mathbf{u}})|} \quad (3.70)$$

The drag and lift coefficients can be found by the following relations:

$$C_D = C_N \cos(\theta) + C_T \sin(\theta), \quad C_L = C_N \sin(\theta) - C_T \cos(\theta) \quad (3.71)$$



**Figure 3.7:** Illustration of unit vectors and force components Kristiansen and Faltinsen (2012).

The inflow angle  $\theta$  is found as,

$$\theta = \cos^{-1} \left( \frac{\mathbf{U}_{rel} \cdot \hat{\mathbf{n}}}{|\mathbf{U}_{rel}|} \right). \quad (3.72)$$



The explicit equations for the normal and tangential coefficients are found by first looking at the characteristic cross-flow velocity between the twines, taking local speed up into account. It is deduced from the principle of conservation of mass and is given as shown below.

$$U_s = \frac{|\mathbf{U}_{rel}| \cos \theta}{1 - Sn}, \quad 0 \leq \theta \leq \pi/4 \quad (3.73)$$

Assuming the force proportional to  $U_s^2$ , as seen in Equation 3.10, the normal force coefficient can now be expressed as,

$$C_N(\theta) = C_D^{c.c} \frac{Sn}{(1 - Sn)^2} \cos^2 \theta, \quad 0 \leq \theta \leq \pi/4. \quad (3.74)$$

$C_D^{c.c}$  is the Reynolds dependent drag coefficient of a circular cylinder. It is understood that the solidity  $Sn$  in the numerator is a result of  $A_{net} = SnA$ . Further  $C_T$  is used as given by Schubauer et al. (1950).

$$\frac{C_T(\theta)}{\theta} = \frac{4C_N(\theta)}{8 + C_N(\theta)}, \quad 0 \leq \theta \leq \pi/4 \quad (3.75)$$

Since Equation 3.74 seems to be conservative and overestimates the drag, one therefore look at an alternative expression based on experimental data to determine  $C_N$  provided by Blevins (2003).

$$C_N^B(0) = \frac{\beta Sn(2 - Sn)}{(1 - Sn)^2}, \quad 0.2 \leq Sn \leq 0.95 \quad (3.76)$$

where  $\beta$  is given in tabular form for different Reynolds numbers up to 400. Because of the fact that there are non-negligible variations for Reynolds numbers higher than 400,  $\beta$  is exchanged with  $0.5C_D^{c.c}$ . Thus yielding the following expression:

$$C_N(\theta) = \frac{C_D^{c.c} Sn(2 - Sn)}{2(1 - Sn)^2} \cos^2 \theta, \quad 0 \leq \theta \leq \pi/4 \quad (3.77)$$

The reasoning behind this change is that as  $Sn \rightarrow 0 \Rightarrow C_N(0) = C_D(0) \rightarrow C_D^{c.c} Sn$ . Implying there are no hydrodynamic interaction between the twines, as would be the correct in that asymptotic case. Thus Equation 3.74 is replaced with Equation 3.77 and the dependency of solidity, Reynolds number and inflow angle is maintained as desired. It is assumed that Equation 3.77 holds for  $Sn \leq 0.5$ .

In order to determine  $C_D^{c.c}$  an empirical formula based on experimental data from Goldstein (1965) is used, which should be valid for Reynolds numbers in the range  $10^{3/2} \leq Re \leq 10^4$ . The resulting equation for  $C_D^{c.c}$  is given as:

$$\begin{aligned} C_D^{c.c} = & -78.46675 + 254.73873(\log_{10} Re) - 327.8864(\log_{10} Re)^2 + 223.64577(\log_{10} Re)^3 \\ & - 87.92234(\log_{10} Re)^4 + 20.00769(\log_{10} Re)^5 - 2.44894(\log_{10} Re)^6 + 0.12479(\log_{10} Re)^7 \end{aligned} \quad (3.78)$$

The Reynolds number is defined by,

$$Re = \frac{d_w |\mathbf{U}_{rel}|}{\nu(1 - Sn)}, \quad (3.79)$$

where  $d_w$  is the diameter of the twines and  $\nu$  is the kinematic viscosity of water.

Further the model is extended to be valid for angles  $\pi/4 \leq \theta \leq \pi/2$ , by representing  $C_D$  and  $C_L$  by their Fourier series,

$$C_D(\theta) = C_D(0) \sum_{n=1}^{\infty} a_{2n-1} \cos((2n-1)\theta) \quad \text{and} \quad C_L(\theta) = C_L(\pi/4) \sum_{n=1}^{\infty} b_{2n} \sin(2n\theta). \quad (3.80)$$

$a_{2n-1}$  and  $b_{2n}$  are the Fourier coefficients, only considering odd and even modes respectively. Implying that  $C_D$  will have maximum at  $\theta = 0$  and  $C_L$  is equal to zero for  $\theta = 0$  and  $\theta = \pi/2$ , as is required. Depending on the accuracy desired, several terms in the series might be used, but as an initial approximation, one could decide to only keep the first term, resulting in,

$$C_D(\theta) = C_D(0) \cos(\theta) \quad \text{and} \quad C_L(\theta) = C_L(\pi/4) \sin(2\theta). \quad (3.81)$$

Here  $C_D(0)$  and  $C_L(\pi/4)$  are given as described in Equation 3.71. In the case of pure current, there will be a reduction of the free stream velocity behind the net due to turbulence in the wake. As long as the distance between the nets are not too large, it is possible to use the following engineering formula,

$$U_{reduced} = rU_{\infty}, \quad (3.82)$$

where  $U_{\infty}$  is the free stream velocity and  $r$  is the reduction factor as presented by Løland (1991), and is given by,

$$r = 1.0 - 0.46C_D(0). \quad (3.83)$$

It should be mentioned that the reduction factor does not take into account that flow might be forced to travel around the entire structure.

To summarize the total local lift and drag force on an entire net panel, taking solidity, inflow angle and Reynolds number into account, is done by adding up the forces acting on each screen. Assuming that the net-panel divided into  $N \times M$  screens, results in the following lift and drag forces acting on the entire net-panel:

$$\mathbf{F}_D = \sum_{i=1}^N \sum_{j=1}^M \frac{1}{2} \rho C_D(\theta) A_{i,j} |\mathbf{U}_{rel}|^2 \hat{\mathbf{u}}, \quad \mathbf{F}_L = \sum_{i=1}^N \sum_{j=1}^M \frac{1}{2} \rho C_L(\theta) A_{i,j} |\mathbf{U}_{rel}|^2 \hat{\mathbf{l}} \quad (3.84)$$

$C_D(\theta)$  and  $C_L(\theta)$  are given by Equation 3.81. In these formulations it is implicitly understood that  $\theta$  and  $\mathbf{U}_{rel}$  will vary from screen to screen, based on how they are defined in Equation 3.72 and 3.68. In the case of this fish farm, the net does not deform, meaning the area of each screen is simply given by,

$$A_{i,j} = \frac{A}{NM}, \quad (3.85)$$

where  $A$  is the total area of the net panel, while  $N$  and  $M$  are the number of screens in the transverse and vertical direction, respectively.

### 3.2.12 Viscous damping

As mentioned in Section 3.2.2 viscous damping has been considered in the equations of motion, however only for the centre spar in heave, to account for viscous effects at the bottom of the structure. As can be understood from the two previous sections, one can rarely consider pure viscous damping for slender structures and nets. Mainly because the drag force will be contributing to a significant amount of excitation and any dampening effect is taken into account by means of the relative velocity, as can be seen in both Equation 3.53 and 3.84.

The main reason why pure viscous damping might be considered for a large-volume structure is that there will be little to no excitation from drag forces compared to other excitation forces. Even though the viscous excitation is small, it does not necessarily mean that viscous effects should be neglected altogether, as there will be excited viscous reaction forces by the body motions. For instance the viscous damping forces from the heave motions of the spar might be described by,

$$F = -\frac{1}{2}\rho C_D |\dot{\eta}_3| \dot{\eta}_3 A, \quad (3.86)$$

where  $\eta_3$  is the heave motion,  $A$  is the area of the bottom of the spar and  $C_D$  is the drag coefficient for flow parallel to the longitudinal axis of a cylinder of finite length.

## 3.3 Natural periods

Having determined the mass, added mass and stiffness of the system in the degrees of freedom of interest, one is able to calculate the natural period. The natural period is defined as the period of oscillation were the inertia and stiffness forces cancel each other out assuming undamped free oscillation (Bachynski et al., 2019). This period is of interest, as large resonant motions might be excited if the system is exposed to external forces that oscillate with a frequency close to the natural frequency. For a single degree of system this can be deduced quite simply from the equations of motion. Undamped free oscillation implies that there are no external forces acting and obviously no damping is present. For instance if heave motion is considered the equations of motion becomes:

$$(M + A_{33})\ddot{\eta}_3 + C_{33}\eta_3 = 0 \quad (3.87)$$

Assuming harmonic motions,  $\eta_3 = \eta_{3a} \sin \omega t$ , makes it possible to rewrite the equations of motion and solve for the natural frequency:

$$-\omega^2(M + A_{33}) + C_{33} = 0 \quad \Rightarrow \quad \omega = \omega_3 = \sqrt{\frac{C_{33}}{M + A_{33}}} \quad (3.88)$$

The natural period in heave is then found simply from,  $T_3 = \frac{2\pi}{\omega_3}$ . In the case of coupled equations, as with coupled surge and pitch motion, the procedure is still the same, in terms of assuming harmonic motion and having no damping and no external force. However in this case one winds up with a system of coupled equations (Greco, 2018).

Assuming origo at the waterline, the system of equations takes the following form:

$$\underbrace{\begin{bmatrix} -\omega^2(M + A_{11}) + C_{11} & -\omega^2(Mz_G + A_{15}) \\ -\omega^2(Mz_G + A_{51}) & -\omega^2(I_{55} + A_{55}) + C_{55} \end{bmatrix}}_{\mathbf{A}} \begin{bmatrix} \eta_{1a} \\ \eta_{3a} \end{bmatrix} = \begin{bmatrix} 0 \\ 0 \end{bmatrix} \quad (3.89)$$

The only non-trivial solution to this equation system is when the determinant of the system matrix ( $\mathbf{A}$ ) is set equal to zero. By doing this, it is possible to solve for the natural frequency and consequently the natural period of the coupled system:

$$|\mathbf{A}| = 0 \quad \Rightarrow \quad \omega = \omega_{15} = \frac{2\pi}{T_{15}} \quad (3.90)$$

Alternatively the natural period might be found experimentally from decay tests. The damping ratio might be found from the principle of logarithmic decrement. The logarithmic decrement ( $\delta$ ) is defined as the natural logarithm of two successive peaks of the decaying oscillatory signal. From the solution of the damped free vibration equation of motion of a dynamic system, with subcritical damping, it is found that the logarithmic decrement can be set equal to the following,

$$\delta = \ln \left( \frac{u_t}{u_{t+T_d}} \right) = \lambda \omega_n T_d = 2\pi \frac{\omega_n}{\omega_d} \lambda = 2\pi \frac{\lambda}{\sqrt{1 - \lambda^2}}, \quad (3.91)$$

where  $u_t$ ,  $u_{t+T_d}$ ,  $\omega_n$ ,  $\omega_d$  and  $\lambda$  are respectively the response peaks at time  $t$  and  $t + T_d$ , natural frequency, damped natural frequency and damping ratio (Langen and Sigbjornsson, 1986). Equation 3.91 can be solved with respect to the damping ratio,

$$\lambda = \frac{\delta}{\sqrt{4\pi^2 + \delta^2}}. \quad (3.92)$$

Furthermore the natural frequency is found as follows,

$$\omega_n = \frac{\omega_d}{\sqrt{1 - \lambda^2}}, \quad (3.93)$$

where the damped natural frequency is found by measuring the time between the successive peaks ( $T_d$ ) and inserting it in the relation  $\omega_d = \frac{2\pi}{T_d}$ . It should be mentioned that the logarithmic decrement by definition assumes linear damping. The problem then arises as there will be quadratic viscous damping present during the decay tests. However it is possible to work around this by only performing the calculations for peaks corresponding to relatively small motions and thus small velocities. By doing this the linear damping will dominate, as the non-linear damping will more or less vanish as it is proportional to the velocity squared.

## 3.4 Additional non-linear effects

Besides the obvious non-linearity in the equations of motion due to the presence of quadratic drag, there are in fact other non-linear phenomena expected to occur for the fish farm in waves. Examples being mean drift forces arising from the waves, in addition to  $KC$ -number dependency of the drag and mass coefficients used in Morison's equation. These non-linearities will therefore be described in greater detail in the following sections.

### 3.4.1 Mean wave-drift forces

Mean wave-drift forces is a non-linear phenomena and refers to the mean forces from the waves acting on the body, which for a floating body will push the body in the direction of the propagating waves. In a potential flow model, the main reason for mean drift forces are connected to the body's capability of generating waves, concerning both radiated waves and diffracted/reflected waves. This can be understood intuitively from Maruo's formula seen in Equation 3.96, where the horizontal mean-drift force ( $\bar{F}_i$ ) is a function of the amplitude of the reflected waves ( $A_R$ ). Maruo's formula is obtained by starting out with the generalized mean-drift force for finite water depth (Faltinsen, 1998).

$$\bar{F}_i = \frac{\rho g}{4} (\zeta_a^2 + A_R^2 - A_T^2) \left( 1 + \frac{2kh}{\sinh(2kh)} \right), \quad i = 1, 2 \quad (3.94)$$

$\zeta_a$  and  $A_T$  are the amplitude of the incident waves and the transmitted waves respectively.  $\rho$ ,  $g$ ,  $k$  and  $h$  on the other hand denotes the density of the fluid, gravitational acceleration, wave number and water depth. By assuming zero energy flux through the surface of the body ( $S_B$ ), it is found that:

$$\zeta_a^2 = A_R^2 + A_T^2 \quad (3.95)$$

Further combining Equation 3.94 and 3.95, and assuming deep water results in Maruo's formula:

$$\bar{F}_i = \frac{\rho g}{2} A_R^2, \quad i = 1, 2 \quad (3.96)$$

However this will only be a small contribution if inertia or drag forces dominate, that is when the cross-sectional dimension of the body is small relative to the wavelength. On the other hand if the wavelengths are very short compared to the cross-sectional dimensions of the body (Diffraction region in Figure 3.1), then the incident waves might be fully reflected and thus  $A_R = \zeta_a$ , which gives the maximum value of the mean-drift force according to Maruo,  $\bar{F}_i = \frac{\rho g}{2} \zeta_a^2$ . The asymptotic value of Maruo's formula might be generalized to hold for any structure with vertical sidewalls, by integrating along the non-shadow part of the waterplane curve Faltinsen (1998):

$$\bar{F}_i = \frac{\rho g \zeta_a^2}{2} \int_{L_1} \sin^2(\theta + \beta) n_i dl, \quad i = 1, 2, 6 \quad (3.97)$$

$\beta$  and  $n_i$  denotes respectively the wave propagation direction and the normal vector in direction  $i$ , while  $\theta$  represents the angular coordinate.

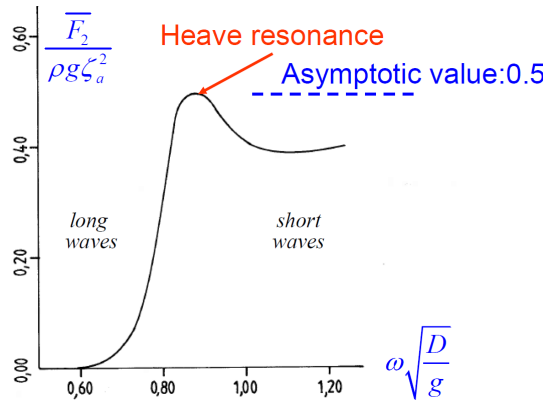
In the case of a circular cylinder in head sea, at finite water depth, the asymptotic value of Maruo's formula is given by:

$$\bar{F}_1 = \frac{2}{3} \rho g R \zeta_a^2 \left(1 + \frac{2kh}{\sinh(2kh)}\right) \quad (3.98)$$

In general it is also possible to add up the different second order contributions to the mean wave loads. For irregular waves this might be done as follows:

$$\bar{F}_i^s = \sum_{j=1}^N \left( \frac{\overline{F_i(\omega_j, \beta)}}{\zeta_a^2} \right) A_j^2 \quad i = 1, \dots, 6 \quad (3.99)$$

Where  $A_j$  denotes the the wave amplitude from the wave spectra corresponding to the frequency  $\omega_j$ .  $\frac{\overline{F_i(\omega_j, \beta)}}{\zeta_a^2}$  represents the second order transfer function for the mean wave-drift forces in direction  $i$  as a function of the direction of the waves relative to the body( $\beta$ ) and the wave frequency( $\omega_j$ ). An example of such a transfer function is provided in the Figure 3.8, where the transfer function for the mean wave-drift force in sway is presented.



**Figure 3.8:** Second order transfer function for mean wave-drift force in sway (Greco, 2018).

It is observed that there is a peak for the mean drift force around heave resonance, meaning there are large relative vertical motions, with a lot of radiated waves, thus increasing the mean force. As the frequency increases and the waves get shorter, diffracted waves becomes important and the mean drift force converges towards the maximum value from Maruo's formula. It should also be noted that for the longest waves, the mean drift force goes to zero. This occurs because the body will follow the waves and not generate any waves of importance (Greco, 2018).

For most surface piercing structures, for instance those not prone to diffraction, the largest contribution to the horizontal wave drift force would be the relative vertical motion between the waves and the body. This will result in a non-symmetric pressure distribution about the transverse axis of the instantaneous wetted surface of the body. Meaning that the average surface elevation in the front part of the structure during one period of oscillation, is greater than in the aft part(Faltinsen, 1998).

As mentioned previously the mean drift forces are a non-linear phenomena, but it is possible to calculate it correct to the second order( $\propto \zeta_a^2$ ), solely from the first order velocity potential. This can be supported by examining the different second order contributions of the wave loads, while neglecting current and forward speed (Greco, 2018).

- Integrating the 1.order pressure( $-\rho \frac{\partial \phi_1}{\partial t}$ ) from  $z = 0$  to  $z = \zeta$ . Assuming the body motions to be small, due to short waves, where diffraction effects dominate(Maruo). This will be the main contribution to mean forces on large-volume structures.
- Integrating the 1.order pressure( $-\rho \frac{\partial \phi_1}{\partial t}$ ) on the instantaneous wetted surface, from  $z = 0$  to  $z = \eta$ , due to the body motions. This will contribute the most when radiated waves are important. Resulting in a modification of the first order pressure and a time varying normal vector on the body wetted surface due to rotations and consequently result in mean forces.
- Integrating the quadratic pressure term in Bernoulli ( $-\frac{1}{2}\rho |\nabla \phi_1|^2$ ), on the mean wetted surface.
- Integrating the linear pressure term in Bernoulli( $-\rho \frac{\partial \phi_2}{\partial t}$ ), on the mean wetted surface of the body, from the second order velocity potential. Since  $\phi_2$  is periodic and oscillates with  $2\omega$ , this second order contribution will provide a zero mean force during one period of oscillation.

From the list provided above it is observed that the only second order contributions to the mean drift force arise from the first order velocity potential.

Another non-linear mean drift force that should be considered when the wave height gets sufficiently large, are those due to viscous effects. Mainly because the mean drift force due to viscous forces is proportional to the wave amplitude cubed ( $\propto \zeta_a^3$ ). This mean force contribution might be found by considering a vertical surface piercing cylinder. First it is assumed that the horizontal drag force might be split into two contributions, one integrating from  $z = -\infty$  to  $z = 0$  and the second from  $z = 0$  to  $z = \zeta$ , as described below.

$$F_{x_1} = \int_{-\infty}^0 \frac{1}{2} \rho C_D D U_{rel} |U_{rel}| dz \quad (3.100)$$

$$F_{x_2} = \int_0^{\zeta} \frac{1}{2} \rho C_D D U_{rel} |U_{rel}| dz \quad (3.101)$$

Time averaging of Equation 3.100 over one period will result in a zero mean, while Equation 3.101 will result in a non-zero mean. This might be estimated by the following.

$$\overline{F_{x_2}} = \frac{1}{2} \rho C_D D \overline{\zeta U_{rel} |U_{rel}|} \quad (3.102)$$

Where  $\overline{\zeta U_{rel} |U_{rel}|}$  denotes the time-averaging of the wave elevation and the relative velocity (Faltinsen, 1998). Depending on the phase between the body motions and the waves, this might actually result in a negative drift force, meaning the body might move in the opposite direction of the wave propagation. This is a phenomena that would be impossible according to Mauros formula in Equation 3.96, where the drift force always would act in the direction of the waves (Greco, 2018).

### 3.4.2 KC-number dependency of $C_D$ and $C_m$

When subjected to an oscillatory flow, both the drag coefficient  $C_D$  and the mass coefficient  $C_m$  for a circular cylinder will be dependent on the amplitude of this flow. This dependency is commonly expressed in terms of the Keulegan-Carpenter number, which is also often referred to as the  $KC$ -number. The  $KC$ -number is defined as,

$$KC = \frac{U_M T}{D}, \quad (3.103)$$

where  $D$ ,  $U_M$  and  $T$  are respectively the characteristic body length, velocity amplitude of the oscillatory flow and period of the oscillatory flow. Intuitively the  $KC$ -number might be understood as the distance water particles travel compared to the characteristic length of the structure. The  $KC$ -number also provides information of the relative importance of drag and inertia loads as seen in the equation below.

$$\frac{F_D}{F_I} = \frac{KC}{\pi^2} \frac{C_D}{C_m} \quad (3.104)$$

It should be noted that the definition of the  $KC$ -number may vary depending on the problem studied. For instance in the case of deep-water waves, the Keulegan-carpenter number might be expressed as,

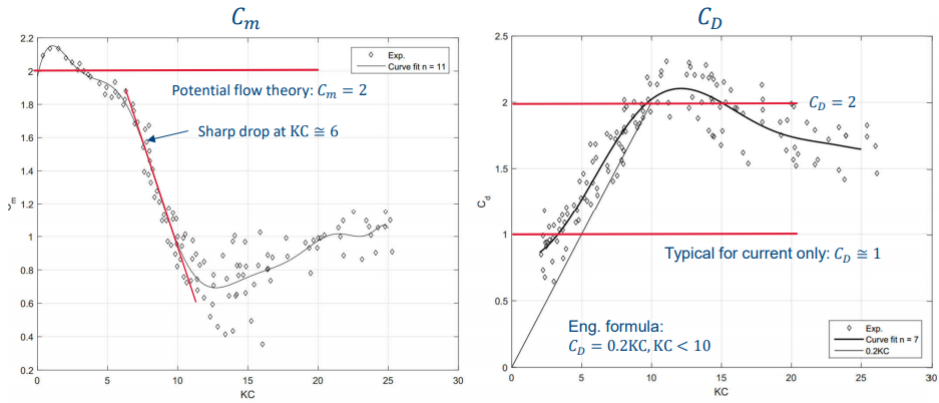
$$KC = \frac{2\pi\zeta_a}{D}, \quad (3.105)$$

where  $\zeta_a$  is the amplitude of the waves. Alternatively  $\zeta_a$  might be replaced by the motion amplitude if only oscillatory motions are considered (Greco, 2018). In the case of this project the  $KC$ -number used has been defined in terms of the relative velocity between the waves and the body, perpendicular to the strip considered, as seen in Equation 4.3.

For low  $KC$ -numbers there will be no vortices shed and potential flow theory holds. For larger  $KC$ -numbers ( $KC \geq 6$ ) there will be flow separation resulting in increased drag and a corresponding reduction in the added mass coefficient ( $C_m$ ), as depicted in Figure 3.9 (Kristiansen, 2019). As the  $KC$ -number gets sufficiently large ( $KC \geq 40$ ) the flow can be considered as a quasi-steady flow and the drag coefficient will be more or less only dependent on the Reynolds number (Greco, 2018).



If this is considered in terms of the fish farm in waves only, it can be assumed that the  $KC$ -number of the nets will be so large that the drag coefficient of the nets only will be dependent on the Reynolds number. For the centre spar the  $KC$ -number will in many cases be so small that one might consider  $C_D = 0$ . With respect to the framework columns on the other hand, it is likely that they will depend significantly on the  $KC$ -number.



**Figure 3.9:** Experimental data of mass coefficient( $C_m$ ) and drag coefficient( $C_D$ ) for a circular cylinder at different  $KC$ -numbers (Kristiansen, 2019).



# Chapter 4

## Numerical Method

In the sections to follow there will be presented a more detailed description of how the numerical calculations were performed both in current and in waves. Regarding discretization, choice of tabulated values for coefficients and in general the reasoning behind the choices made with reference to the theory presented previously.

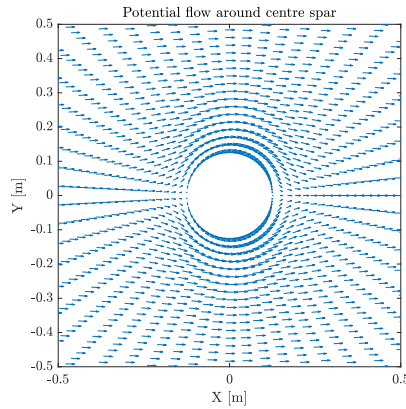
### 4.1 Steady current

The calculations were performed for current velocities in ranging from 0.04 m/s to 0.16 m/s with steps of 0.01 m/s. In full scale this would correspond to velocities ranging from 0.5 m/s to 2.0 m/s, when using Froude scaling. Calculations were performed for the fish farm both with and without nets. The model was in practice divided into several different main components consisting of the centre spar, the circular framework columns, the square framework columns and the nets.

#### 4.1.1 Modelling of flow

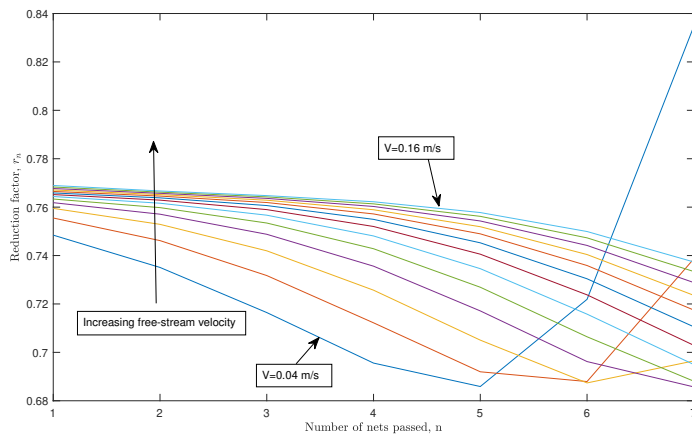
In order to be able to get a relatively good estimation of the drag, the main characteristics of the flow surrounding the fish farm had to be taken into account. One such characteristic being flow moving around the centre spar. Another one appearing in the case of nets being attached, is the reduction of the flow velocity as it passes through the nets.

To account for flow moving around the centre spar, non-separated potential flow was used, as described by Equation 3.3. In reality there will be separation and circulation of the flow affecting the velocity field, but non-separated potential flow was deemed adequate to describe the flow acting on the fish farm components surrounding the centre spar. An illustration of the velocity field of the non-separated potential flow can be seen in Figure 4.1 below.



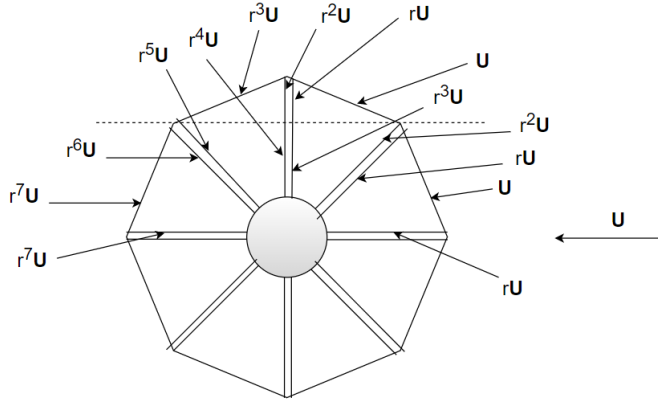
**Figure 4.1:** Top view illustration of velocity field around centre spar, by assuming non-separated flow .

To describe the reduction of the free-stream velocity due to the nets, Equation 3.82 was used. As is obvious from Equation 3.82 the reduction factor will be dependent on the Reynolds number, and therefore several different reduction factors will be present, depending on the free-stream velocity and on how many nets the flow has passed through. The reduction factors used are presented in Figure 4.2. As indicated in Figure 4.2 each line represent the reduction factors as a function of how many nets the flow has passed through, for one particular free-stream velocity. The free-stream velocities range from 0.04 m/s to 0.16 m/s with steps of 0.01 m/s as you move upwards from the bottom line to the top line as shown on the figure.



**Figure 4.2:** Reduction factors as function of the number of nets passed, for different free-stream velocities.

Figure 4.3 provides a visualization of the implementation of the reduction factors. In this figure only one reduction factor is used, as it makes it easier to get an overview of how the implementation was carried out.



**Figure 4.3:** Top view of fish farm illustrating the implementation of reduction factors,  $r$ , on each net-panel.

### 4.1.2 Spar

For the centre spar it is necessary to account for its finite length. Since the draft of the spar is comparable to its diameter using a two-dimensional drag coefficient cannot be justified in steady current, as there will be substantial flow beneath the bottom of the spar. To account for the finite length of the centre spar the two-dimensional drag is adjusted by a reduction factor ( $\kappa$ ) such that,

$$C_D = \kappa C_D^\infty, \quad (4.1)$$

where  $C_D^\infty$  is the two-dimensional drag coefficient for an infinitely long cylinder. Since the Reynolds number of the spar ranged from  $10^4$  to  $4 \cdot 10^4$  there will not be significant changes in the two-dimensional drag coefficient as function of Reynolds number as can be seen from Figure 3.2a. Therefore  $C_D^\infty = 1$  is used for the spar, which according to Blevins (1984) should be valid for  $Re \sim 10^5$ . The reduction factor due to finite length were found by interpolating in tabulated values provided by Blevins (1984), seen in Table 4.1, resulting in a drag coefficient of  $C_D = 0.5847$ .

It should be noted that since the spar only has one free end for the flow to pass around, namely the bottom, the length ( $L$ ) used in the interpolation of the values in Table 4.1, is twice the draft of the centre spar. Using the free surface as a plane of symmetry, it is realized that from a hydrodynamic point of view, the flow around the centre spar with one free end, is equivalent to the flow around a cylinder with length equal to twice the draft of the centre spar with two free ends.

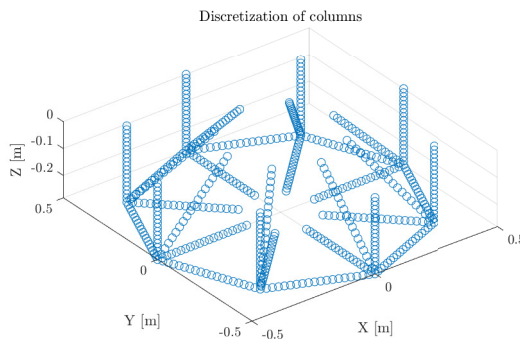
**Table 4.1:** Reduction factors due to finite length (Blevins, 1984).

$L/D$	$\kappa (Re < 10^5)$	$\kappa (Re > 5 \cdot 10^5)$
2	0.58	0.80
5	0.62	0.80
10	0.68	0.82
20	0.74	0.90
40	0.82	0.98
50	0.87	0.99
100	0.98	1.00

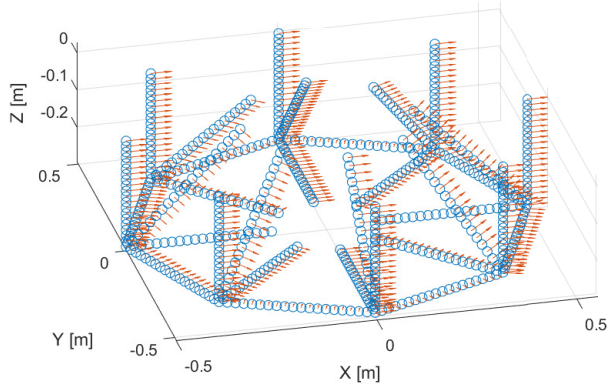
### 4.1.3 Columns

As opposed to the centre spar, the drag coefficients of the circular columns of the framework should not be considered independent of the Reynolds number, as the Reynolds numbers are in a completely different range. For the circular columns the Reynolds numbers will be spanning from approximately 100 to 2560 and the two-dimensional drag coefficient were instead determined from Equation 3.78, which should be valid for this range of Reynolds numbers. Furthermore reduction factors are implemented similarly for the circular columns as for the centre spar using Table 4.1.

For the square columns, which makes out the octagonal bottom of the frame, Reynolds number variation was not considered. This might be justified to some extent as the variation will not be as great due to the sharp corners. Therefore a drag coefficient provided by DNV (2011) was used, with  $C_D = 2.2$ . Another point worth mentioning is that of all the columns on the bottom of the frame only the front half of the bottom octagon was considered. The reason for this is to not over estimate the drag as there will be substantial back-flow and thus reduced flow velocities on the remaining bottom columns. To further be able to take into account the many different orientations of the columns and the spatial variation of the flow, the columns were discretized as depicted Figure 4.4 below.

**Figure 4.4:** Discretization of framework columns.

Each column was discretized by means of 19 points each with equal spacing, which when added to the 8 junction points, resulted in a total of 616 elements. Furthermore the cross-flow principle was applied to the columns, such that only the normal component of the force acting on the columns has been applied when calculating the drag. Figure 4.5 provides a depiction of the normal vectors acting on each individual column.



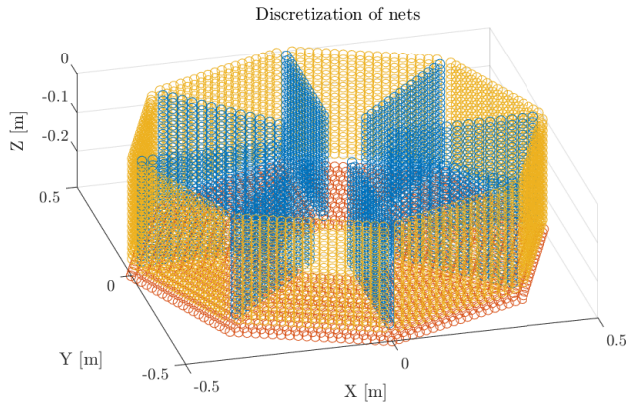
**Figure 4.5:** Illustrations of frame unit normal vectors.

#### 4.1.4 Nets

As with the framework columns, the nets were also discretized, as shown in Figure 4.6. The nets were further divided into three main groups, respectively the bottom net, external nets and internal nets, because a discretized screen in each of these groups will have different areas connected to them. With regards to the internal nets it should be noted that one discretized net-panel, as seen in blue in Figure 4.6, represent what in reality would be two parallel nets in close proximity to one another, and is located at what would be the middle of those two nets. This is done in order to reduce the computational effort and is justified as long as reduction of flow through the neighbouring parallel net is considered. There will be a minor difference between the numeric and experimental model, because of the spatial variation of the potential flow, but since the nets in reality would be very close, the consequence of this simplification was assumed to be negligible. The nets were discretized as described in the Table 4.2.

**Table 4.2:** Discretization scheme for nets.

Net component	Number of discretized nets	Screens per net	Total number of screens
Internal net	8	$19 \times 14$	2128
External net	8	$19 \times 18$	2736
Bottom net	1	1677	1677
<i>Total</i>	<i>17</i>	-	<i>6541</i>

**Figure 4.6:** Discretization of bottom net(red), internal nets(blue) and external nets(orange).

Furthermore the forces acting on the nets were calculated as described in Section 3.2.11 and the reduction of flow through the nets were taken into account as outlined in Section 4.1.1.

#### 4.1.5 Wave resistance

For bodies moving with constant forward speed in calm water, one often have to consider the wave resistance, which arises from the generation of waves as the object moves through the water. The wave resistance coefficient is often expressed as a function of the Froudes number to the  $n$ 'th power, where  $n$  typically is in the range of 3-7 (Steen, 2011). Thus intuitively enough it is realized that for larger Froude numbers the wave resistance should be considered. However according to Steen (2011) the wave resistance coefficient tends towards zero for low Froude numbers and might be neglected for Froude numbers lower than approximately 0.1-0.15. Since the largest current speed considered for the fish farm does not correspond to a Froude number larger than approximately 0.1, no waves of importance will be generated by the centre spar. The wave resistance was therefore considered negligible.



## 4.2 Regular waves

There were performed calculations analyzing the fish farm in regular waves, to obtain excitation forces, RAOs and their respective phases in surge, pitch and heave. The calculations were performed for the fish farm both with and without nets attached. The water depth was assumed to be 0.8 m. The wave periods used ranged from 0.5 s to 1.8 s, which in full scale would correspond to wave periods ranging from 6.3 s to 22.8 s. Further three different wave steepnesses 1/100, 1/60 and 1/30 were examined to assess amplitude dependency. The wave steepness,  $\epsilon$ , is defined as,

$$\epsilon = \frac{H}{\lambda}, \quad (4.2)$$

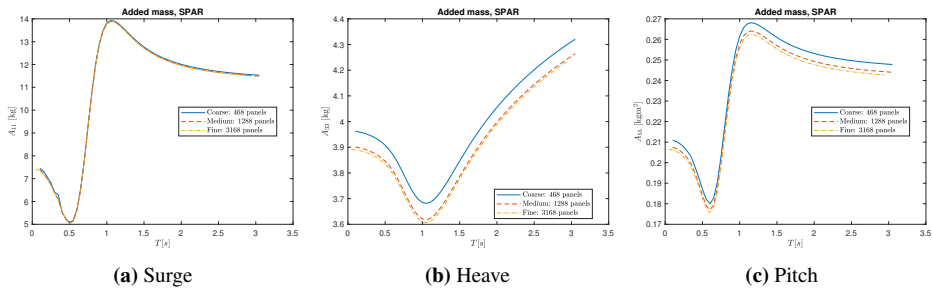
where  $H$  is the wave height and  $\lambda$  is the wavelength. All calculations were performed on the mean wetted surface of the fish farm. It should be mentioned that as a result of the two different test configurations, two different ballast schemes had to be used. In addition there were some minor differences in the pretension of the mooring lines for the tests performed with and without nets. As a result two different mass and stiffness matrices had to be used in the calculations. These matrices can be found in Appendix D.

### 4.2.1 Modelling of flow

Two different types of flow have been examined for the forces acting on the geometry surrounding the centre spar of the fish farm. First off were undisturbed incident waves described by Equation 3.34. The other flow considered was a velocity field based on the combination of the incident wave potential and the diffracted wave potential of the centre spar. This velocity field was obtained by the use of WAMIT for what would be the coordinates of the mean position of the discretized nets and columns. In practice this velocity field should be very similar to the one provided by the velocity potential described in Equation 3.37. Furthermore the reduction of the fluid flow due to nets, were assumed to only significantly impact the internal net panels, specifically the neighbouring parallel nets and reduction factors were therefore only implemented on these nets.

### 4.2.2 Spar

The centre spar was analyzed in WAMIT and discretized by means of 3168 quadrilateral elements as seen in Figure 4.8. This type of discretization is necessary in order for the panel method algorithm in WAMIT to be able to solve the radiation and diffraction problem discussed in Section 3.2.6 and 3.2.7. The number of elements used were determined based on performing a convergence test in order to make sure that the hydrodynamic quantities of interest had converged. Quantities being added mass, potential damping and excitation forces (Froude-Kriloff and diffraction), in addition to the diffracted velocity field. The results of the convergence test for the added mass in surge, heave and pitch can be seen in Figure 4.7, while the convergence of the other hydrodynamic quantities can be seen in Appendix F.



**Figure 4.7:** Convergence of added mass in surge, heave and pitch from WAMIT, with centre spar discretized by means of respectively 468, 1288 and 3168 quadrilateral panels.

A consequence of only analyzing the spar in WAMIT, is that only the added mass of the spar will be frequency dependent. In addition, the spar will contribute to the entirety of the radiation damping of the system. The latter might be justified as the spar will be the component of the structure which will generate the most waves.

Since WAMIT provides outputs described by linear potential theory, this means that contributions like drag or pure viscous damping is not considered to be acting on the spar initially. For the shortest periods excitation from drag is not of importance, however there will be some viscous damping due to motions of the spar. For the longest waves, excitation from drag might also start to be significant enough for it to be considered. Therefore drag has been accounted for in pitch and surge as described in Equation 3.62 and 3.63, but without the inertia term. For heave on the other hand, pure viscous damping is considered. Mainly because there will be little drag excitation acting vertically on the sides of the spar. Concerning the bottom of the spar, even for the longest waves, there will only be minor excitation as the drag force excitation decreases with a factor of approximately  $e^{2kz}$ , the further below the free-surface you move.

For pure viscous damping in heave, a drag coefficient for flow parallel to the longitudinal axis of a cylinder of finite length provided by DNV (2011) has been used. It was determined by interpolation in Table 4.3, resulting in  $C_D = 0.8535$  being used in heave.

**Table 4.3:** Drag coefficients for flow parallel to cylinder of finite length (DNV, 2011).

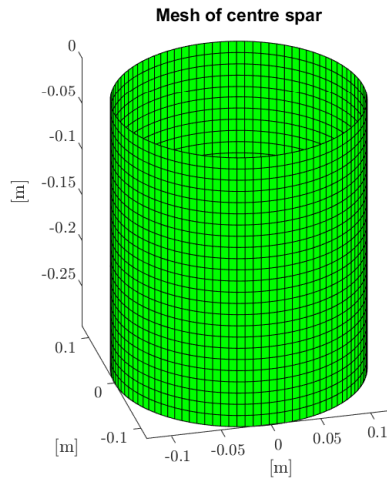
$L/D$	$C_D$
0	1.12
1	0.91
2	0.85
4	0.87
7	0.99

For the drag force acting in surge and pitch, strip theory in combination with the cross-flow principle was used. Using strip theory for the shortest waves and smallest motions is rather questionable, but in this case the drag force will be small to not impact the results significantly. For the longer waves and larger motions, strip theory might be justified to a greater extent, as the flow variation perpendicular to the length of the spar will be less prominent, but it is still not ideal.

Since the relative motions are oscillatory it was decided to use drag coefficients in surge depending on the  $KC$ -number. These were found by calculating the  $KC$ -number of each strip and interpolating in experimental values provided by both Faltinsen (1998) and Kristiansen (2019). The experimental data of the latter can be seen in Figure 3.9. The  $KC$ -number of each strip were calculated by,

$$KC = \frac{(\mathbf{U}_{rel} \cdot \hat{\mathbf{n}})T}{D}, \quad (4.3)$$

where  $\mathbf{U}_{rel}$  is the relative velocity at the strip,  $\hat{\mathbf{n}}$  is the unit normal vector,  $T$  is the period of oscillation and  $D$  is taken as the diameter of the strip.



**Figure 4.8:** Discretization of centre spar with 3168 panels used in WAMIT.

### 4.2.3 Columns

The columns were discretized similarly for the calculations in waves as for steady current as seen in Figure 4.4. The excitation forces acting on the columns were calculated using Morisons equation as described by Equation 3.62 in Section 3.2.10.

The  $KC$ -numbers were calculated for each strip using Equation 4.3. For  $KC$ -numbers ranging from 0 to 25, the drag coefficients of the circular columns were determined by interpolating in experimental data provided by Faltinsen (1998) and Kristiansen (2019). For  $KC$ -numbers larger than 40, the flow might be considered quasi-steady and the drag coefficients will be significantly more dependent on the Reynolds number than the  $KC$ -number. As a result, for  $KC \leq 40$  the drag coefficients were calculated using Equation 3.78, with Reynolds numbers for each strip defined by,

$$Re = \frac{(\mathbf{U}_{rel} \cdot \hat{\mathbf{n}})D}{\nu}, \quad (4.4)$$

where  $D$  is the diameter of the circular columns,  $\nu$  is the kinematic viscosity,  $\hat{\mathbf{n}}$  is the normal vector on the strip and  $\mathbf{U}_{rel}$  is the relative velocity vector on the strip. In the range  $25 < KC < 40$  a weighted linear function was used, changing the drag coefficient from being completely determined by the  $KC$ -number at  $KC = 25$  to being only a function of the Reynolds number at  $KC = 40$ .

The mass coefficient ( $C_m$ ) used for the circular cylinders were also considered  $KC$ -dependent and was determined from the experimental values provided by Kristiansen (2019) seen in Figure 3.9 for  $0 < KC < 25$ . In the range  $25 < KC < 40$  the mass coefficient was taken to be increasing linearly to the asymptotic value of  $C_m = 1.6$  provided by DNV (2010), which was used for  $KC > 40$ .

For the square columns both the drag and mass coefficients were only considered to be a function of the inflow angle ( $\theta$ ), in order to take into account for the change in geometry experienced by the flow as the inflow angle changes. Once again tabulated values from DNV (2010) were used to determine the coefficients and the values which were used for interpolation is presented in Table 4.4.

**Table 4.4:** Inflow angle dependent drag and mass coefficients for square section (DNV, 2010).

$\theta$	0°	5°	10°	15°	20°	25°	30°	35°	40°	45°
$C_D$	2.2	2.1	1.8	1.3	1.9	2.1	2.2	2.3	2.4	2.4
$C_m$	2.186	—	—	—	—	—	—	—	—	2.194

The contribution from the columns to the total added mass of the system were calculated using strip theory and the cross-flow principle as described by Equation 3.49 and 3.50 respectively. The two-dimensional added masses used for the square and circular columns were provided by DNV (2010) and are listed in Table 4.5.

**Table 4.5:** Two-dimensional added mass (DNV, 2010).

	$A_N^{2D}$
Square columns	$1.51\rho\pi(h/2)^2$
Circular columns	$\rho\pi a^2$

In the table above  $a$  is the radius of the circular columns and  $h$  is the height/width of the square section.

#### 4.2.4 Nets

The nets were discretized similarly for the calculations in waves as in steady current, and can be seen in Figure 4.6. The main reason behind the fine discretization of the nets in waves, is because even though the velocity of the water particles decay exponentially as one moves further beneath the free-surface, one still have to consider the velocity of the screen due to the body motions. The result of this discretization scheme should therefore be that both excitation and damping due to the drag will be described correctly, since relative velocities are considered. The excitation forces acting on the nets were calculated using the screen-type load model outlined in Section 3.2.11. It was further assumed that the nets are completely dominated by drag and viscous effects. The added mass of the nets were therefore considered negligible. Further reduction factors were only implemented on the internal nets, as mentioned in Section 4.2.1.

#### 4.2.5 Solving the equations of motion using ODE45

Because of the presence of drag and amplitude-dependent mass and drag coefficients, there will be strong non-linearities in the equations of motions, thus frequency domain analysis is no longer an option. In order to solve the non-linear differential equations in time-domain, the Runge-Kutta solver *ODE45* was used in MATLAB. In practice what this solver requires are defined state variables, and further it is necessary to define the derivative of the state variables, in terms of the state variables. Since the fish farm is subjected to head-sea, the only degrees of freedom that will be excited are surge, pitch and heave. Furthermore there is a strong coupling between pitch and surge. The practical procedure of coping with this using *ODE45* will therefore be described next. First the state variable vector  $\mathbf{s}$  is defined in terms of the degrees of freedom that are of interest.

$$\mathbf{s} = [s_1, s_2, s_3, s_4, s_5, s_6]^T = [\eta_1, \dot{\eta}_1, \eta_3, \dot{\eta}_3, \eta_5, \dot{\eta}_5]^T \quad (4.5)$$

The derivative of the state variable vector  $\dot{\mathbf{s}}$ , then takes the following form

$$\dot{\mathbf{s}} = [\dot{s}_1, \dot{s}_2, \dot{s}_3, \dot{s}_4, \dot{s}_5, \dot{s}_6]^T = [\dot{\eta}_1, \ddot{\eta}_1, \dot{\eta}_3, \ddot{\eta}_3, \dot{\eta}_5, \ddot{\eta}_5]^T \quad (4.6)$$

Expressing  $\dot{\mathbf{s}}$  in terms of  $\mathbf{s}$  yields,

$$\dot{\mathbf{s}} = [s_2, \dot{s}_2, s_4, \dot{s}_4, s_6, \dot{s}_6]^T \quad (4.7)$$

In order to solve for  $\dot{s}_2$ ,  $\dot{s}_4$  and  $\dot{s}_6$  which are still unknown, it is necessary to turn to the equations of motion, which for surge, heave and pitch will be as described below.

$$(M + A_{11})\ddot{\eta}_1 + (Mz_G + A_{15})\ddot{\eta}_5 + B_{11}\dot{\eta}_1 + B_{15}\dot{\eta}_5 + C_{11}\eta_1 = F_1^{exc} \quad (4.8)$$

$$(M + A_{33})\ddot{\eta}_3 + B_{33}\dot{\eta}_3 + B_v\dot{\eta}_3|\dot{\eta}_3| + C_{33}\eta_3 = F_3^{exc} \quad (4.9)$$

$$(I_{55} + A_{55})\ddot{\eta}_5 + (Mz_G + A_{51})\ddot{\eta}_1 + B_{55}\dot{\eta}_5 + B_{51}\dot{\eta}_1 + C_{55}\eta_5 = F_5^{exc} \quad (4.10)$$

$F_1^{exc}$ ,  $F_3^{exc}$  and  $F_5^{exc}$  denotes the total excitation forces acting on the structure in respectively surge, heave and pitch. Equation 4.9 can be with solved with respect to  $\dot{\eta}_3$  and expressed in terms of the state variables, thus resulting in,

$$\dot{s}_4 = \dot{\eta}_3 = \frac{1}{M + A_{33}}(F_3^{exc} - B_{33}s_4 - B_v s_4 |s_4| - C_{33}s_3) \quad (4.11)$$

Since Equation 4.8 and 4.10 are coupled, some algebra have to be performed. Solving Equation 4.10 with respect to  $\ddot{\eta}_5$  and then inserting the expression obtained for  $\ddot{\eta}_5$  into Equation 4.8 and finally solving with respect to  $\ddot{\eta}_1$  yields:

$$\dot{s}_2 = \ddot{\eta}_1 = \frac{F_1^{exc} - B_{11}s_2 + B_{15}s_6 - C_{11}s_1 - \frac{Mz_G + A_{15}}{I_{55} + A_{55}}(F_5^{exc} - B_{55}s_6 - C_{55}s_5 - B_{51}s_2)}{M + A_{11} - \frac{(A_{15} + Mz_G)(A_{51} + Mz_G)}{I_{55} + A_{55}}} \quad (4.12)$$

Inserting Equation 4.12 into Equation 4.10 then makes it possible to express  $\dot{s}_6$  in terms of the state variables

$$\dot{s}_6 = \dot{\eta}_5 = \frac{1}{I_{55} + A_{55}}(F_5^{exc} - B_{55}s_6 - B_{51}s_2 - C_{55}s_5 - (A_{51} + Mz_G)\dot{s}_2) \quad (4.13)$$

In order to increase the readability, only  $\dot{s}_2$  is inserted into Equation 4.13 and not the entire expression from Equation 4.12. However it is understood that  $\dot{s}_6$  is expressed only in terms of the state variables, since that is the case for  $\dot{s}_2$ . Having expressed the derivatives of the state variables, in terms of the state variables, the only thing that remains are initial conditions for the state variables and the time period one wants to solve for. With regards to the initial conditions, the fish farm was assumed to be at rest at time  $t = 0$ , meaning that:

$$[s_1(0), s_2(0), s_3(0), s_4(0), s_5(0), s_6(0)]^T = [0, 0, 0, 0, 0, 0]^T, \quad (4.14)$$

Having obtained the time-series of the DOFs of interest, the RAO( $H(\omega)$ ) and phase( $\phi$ ) are simply found from,

$$H(\omega) = \frac{\eta_a}{\zeta_a}, \quad \text{and} \quad \phi = \omega\tau, \quad (4.15)$$

where  $\eta_a$  is the amplitude of the DOF of interest,  $\zeta_a$  is the wave amplitude,  $\omega$  is the wave frequency and lastly  $\tau$  is the time-difference between the peak of the motion and the peak of the surface elevation. It is important to mention that these calculations should be performed when transients have died out and steady state conditions are achieved.

# Experimental Method

The model used in this project consists of a large-volume spar in the centre, encircled by an orthogonal framework made out of quadratic and circular cylinders. When nets were used, these were attached between the framework and the spar, as well as on the exterior of the framework. Thus enclosing eight individual fish cages. The model tests were performed in "Lilletanken" at NTNU campus Tyholt in the spring of 2020. The experiments performed were towing tests, decay tests and tests in regular waves. All of which were performed both with and without net-panels. In the following sections a more detailed description of the model, the tests and instrumentation used, will be presented.

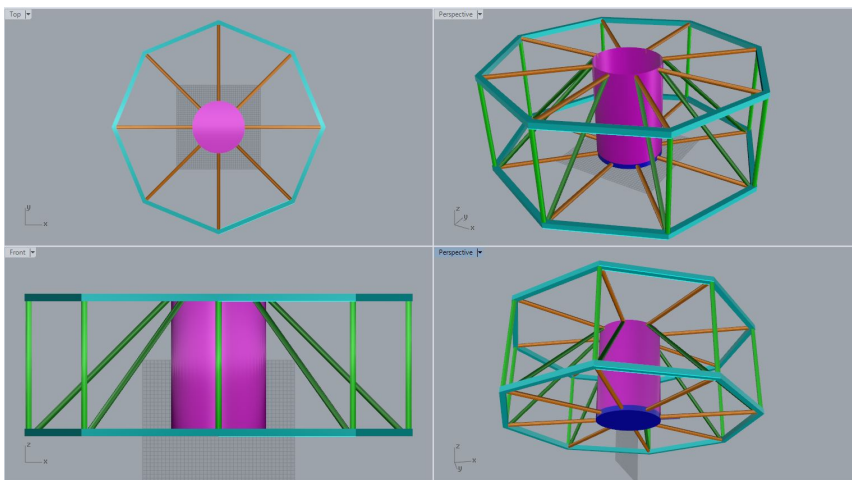
## 5.1 Description of model

The model was scaled with a factor of 1:160 compared to what would be the full-scale construction. This is done in order to reduce the wall effects present during testing since the towing tank is only about 2.5 m wide. The centre spar was made out of aluminium, while the surrounding framework was made out of carbon-fiber, in order to make the structure rigid. When it comes to the net-panels, these were made out of a type of steel netting and fastened with tension on every side using small cable ties as seen in Figure 5.6. As a result the deflection of the nets are kept to a bare minimum. A description of the various structural details of the model is presented below:

- At the centre of the model, is a vertical spar with diameter of 25 cm and length of 37.5 cm.
- The model consist of one octagonal top-frame and one octagonal bottom-frame, both of which have a quadratic cross-section of 20 mm × 20 mm. The total diameter of the octagon is 100 cm.

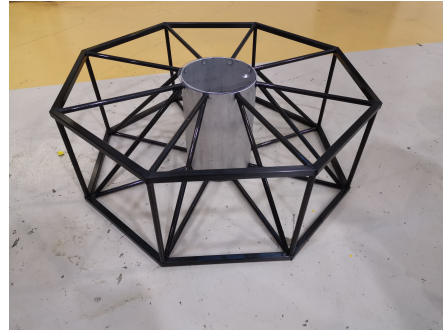
- The octagonal top- and bottom-frame are connected with each other by a total of eight vertical circular cylinders with diameter of 16 mm and length 33.5 cm.
- From each corner of both the top- and bottom-frame horizontal circular cylinders with diameter of 16 mm and length 36.1 cm connects the octagonal frames to the top and bottom of the spar, respectively.
- From each corner of the bottom-frame there are diagonal circular cylinders, angled at  $45^\circ$ , with diameter of 16 mm, connecting the corners of the bottom frame to the top of the spar.
- In reality instead of eight external vertical net-panels with height and width of  $33.5\text{ cm} \times 38.3\text{ cm}$ , which was assumed in the numerical model, one large net-panel was wrapped around the structure. Measuring roughly  $33.5\text{ cm} \times 310\text{ cm}$ .
- One large external, octagonal, horizontal net panel was located the bottom of the structure. The total diameter of the bottom net was 100 cm. At the centre of the bottom net was a circular hole with a diameter of 25 cm.
- On each side of the diagonal cylinders, there were internal vertical net-panels with height and width of  $33.5\text{ cm} \times 36.1\text{ cm}$ . Meaning there was a total of sixteen internal net-panels.
- All of the net-panels had the same solidity, which was measured to 0.166. Furthermore the twine diameter of the net was measured to be 1.1 mm.
- The operational draft of the structure used was 29.4 cm.

A 3D-model was made of the fish farm without net-panels by Trond Innset, based on the information provided above. Screenshots of the 3D-model from various angles can be seen below.



**Figure 5.1:** 3D-model of fish farm without net-panels.





(a) Model with nets, after being painted and ballasted (b) Model without nets, before ballasting and painting

**Figure 5.2:** Experimental model with and without nets.

## 5.2 Experimental setup towing tests

Towing tests were performed in order to emulate steady current acting on the fish farm. With towing speeds ranging from 0.04 m/s to 0.16 m/s.

The towing setup consisted of four poles with pulleys at the ends, that were fastened to the towing carriage. From these poles, through the pulleys, spanned ropes angled horizontally at  $45^\circ$ , thus connecting the fish farm to the towing carriage. The four ropes used were tensioned significantly in order to ensure that any motions of the fish farm relative to the towing carriage was kept at a bare minimum. The towing setup used can be seen in Figure 5.3. Furthermore the fish farm was ballasted in order to obtain the desired draft, with no trim and no heel.

From Figure 5.3 it is also possible to observe the instrumentation used. There were used four force transducers, in order to measure the force acting on the fish farm, which were located at each of the mooring line attachment points on the fish farm. Pitch/trim and roll/heel angles were measured by an inclinometer located on top of the centre spar. Lastly there was used a wave-probe in front of the centre spar to get an indication of whether significant waves were generated or not.



Figure 5.3: Towing setup.

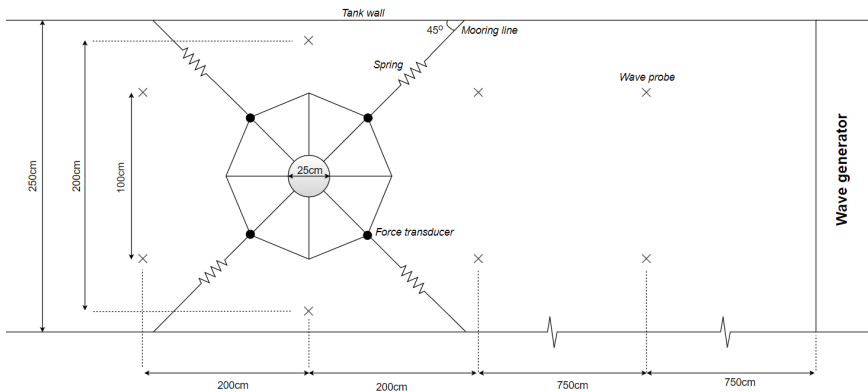
### 5.3 Experimental setup regular wave tests

The tests in regular waves were performed for wave steepnesses of  $1/30$ ,  $1/60$  and  $1/100$ , with wave periods ranging from  $0.4\text{ s}$  to  $1.8\text{ s}$ , at a water depth of  $0.8\text{ m}$ . This was done in order to obtain amplitude dependent RAOs, mooring line forces and their respective phases, in heave, pitch and surge. In addition the regular wave tests made it possible to obtain mean wave-drift forces as a function of the wave period. An overview of the experimental setup used during the wave tests, in addition to a picture of the setup as seen in reality are provided in Figure 5.4 and 5.5 respectively.

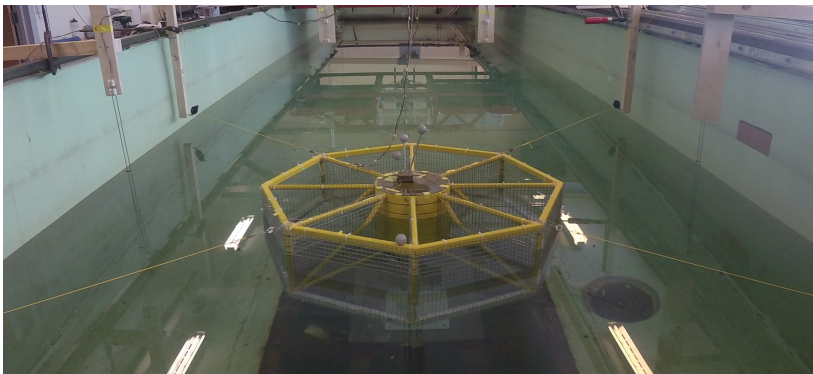
The model was moored symmetrically with four horizontal mooring lines, angled at  $45^\circ$ , each one connected with a spring and a force transducer. The mooring lines were made horizontal by using poles with pulleys attached to the ends, fastened on the tank walls. The springs used were relatively soft, each with a measured stiffness of  $29.1\text{ N/m}$ , in order for the fish farm to act as if it had a slack mooring system. As can be seen on Figure 5.5 there were also used "Oqus". "Oqus" is a motion capture system provided by Qualisys and was used to obtain the RAOs. The motion capture system works by having cameras tracking reflective spheres on the model. A point worth making when using "Oqus", is that one have to choose a reference point that defines the rigid body motions. To ensure that the calculations and experiments are comparable, the centre of the waterplane was used as the reference point.

"Oqus" was also used in combination with the force transducers in order to obtain the total mooring system force. By knowing the exact position of the mooring line connection points at any given time and knowing where the mooring line is fixed at the tank wall, it was possible to obtain the total mooring system force by decomposing and adding together the force acting on each individual mooring line. In addition, this enabled the possibility of quantifying the mean wave-drift force by simply taking the mean of the resulting mooring system force time-series.

Furthermore a total of eight wave probes were used. Two pairs of parallel wave probes were located in front of the fish farm, one pair behind it and one pair aligned with the centre of the fish farm. Thus enabling the possibility of establishing phases, but also ensuring that the actual incoming waves are known. With respect to the phases, it should be mentioned that to account for the presence of mean forces, the phases obtained had to be adjusted according to the mean offset of the fish farm position.



**Figure 5.4:** Overview of experimental setup for testing in waves.



**Figure 5.5:** Experimental setup for testing in waves.

Since the model was tested both with and without nets, two different ballast configurations had to be used in order to obtain the same draft. The fish farm was ballasted by using several small 5 mm thick steel weights, most of which were placed evenly around all edges of the octagonal bottom-frame as seen in Figure 5.2a. The remaining ballast needed was located in the centre of spar for the fish farm without nets. For the fish farm without nets, most of the remaining ballast was located inside the centre spar, while some of the weights were placed on the octagonal top-frame as seen in Figure 5.7. All ballast was fastened in order to keep it from moving. What is important to note is that the ballast located under water was equal for the two test configurations to ensure comparability. The two ballast schemes resulted however in different centre of gravity, moment of inertia and mass displacement. The differences in these parameters are provided in Table 5.1. It is noted that the values for the centre of gravity and moment of inertia are defined based on a coordinate system with origo at the centre of the waterplane area. It is further mentioned that the difference in mass displacement occurs as a result of the submerged volume of the nets.

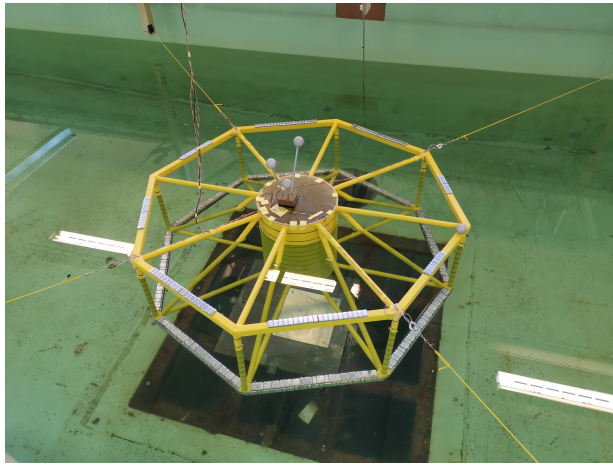
**Table 5.1:** Results of different ballast configurations.

	$I_{55}$ [ $kgm^2$ ]	$\Delta$ [ $kg$ ]	$z_G$ [ $m$ ]	Draft [ $m$ ]
With nets	2.0527	18.43	-0.186	0.294
Without nets	1.7943	17.95	-0.2024	0.294

It should be mentioned that the thickness of the steel weights was accounted for in all numeric calculations by considering a cross-section of 30 mm  $\times$  30 mm instead of 20 mm  $\times$  20 mm for the square columns, since the weights covered the entire octagonal bottom-frame on all sides.



**Figure 5.6:** Close up picture illustrating the use of cable ties for fastening of the nets.



**Figure 5.7:** Picture of the fish farm without nets set up for testing in regular waves.

## 5.4 Decay test setup

When it comes to the decay tests, these were performed using the test setup described for regular waves. The procedure of performing the decay tests were relatively straight forward. In heave there was used a stick to push down at the centre of the fish farm in order to excite heave motions only. Since surge and pitch are coupled in this problem, the excitation was done by simply pushing the fish farm forward with the aforementioned stick.

## 5.5 Experimental sources of error

Both during the experimental tests in steady inflow and in regular tests there are several possible errors that should be considered. For instance during towing, there are bias errors as a result of human errors in the setup, for instance regarding the heading of the fish farm and the symmetry of the towing setup. There were also some leakage at the wave-generator and water behind the wave generator was pumped to the other end of the towing tank. This would therefore result in a minor flow towards the wave generator. Since the towing speeds were very low, there will also be random errors as a result of measurement noise and vibrations in the towing carriage.

In the regular wave tests there will be bias errors as a result of asymmetry in the mooring setup, inaccuracies in the heading of the fish farm, inaccurate measurement of the position of the reflective spheres used for motion tracking and errors related to tank wall reflections. Other sources of error at the longest wave periods and steepest waves relates to mooring lines both going slack and getting submerged. Another issue is connected to the force transducers, as their measurements may drift if the force transducers experience a change in temperature, which will occur if they get wet.



## Results and Discussion

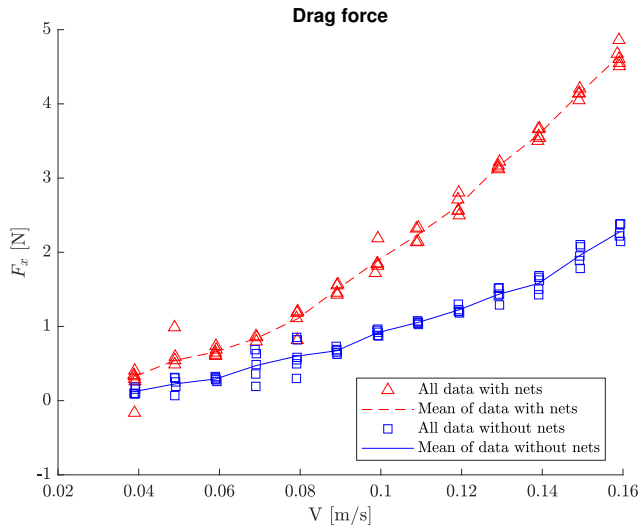
In the following sections the results obtained from the experiments and numerical calculations, will be presented and discussed. Providing comparisons between the model with and without nets attached and further discussing how the numerical results compared to the experimental results.

### 6.1 Current forces

#### 6.1.1 Experimental results

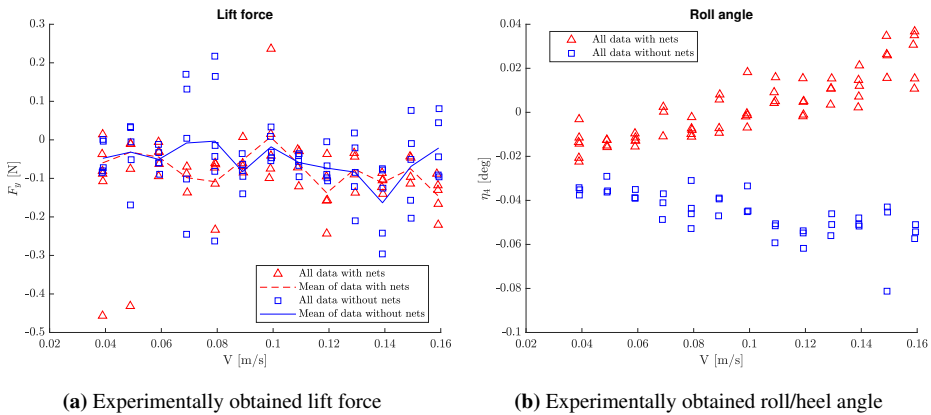
The experimental results from the towing tests were obtained by time-averaging of the different measurements, in a time-interval where the velocity was more or less constant and where transients had died out.

Figure 6.1 provides the the experimental drag force obtained as a function of the towing speed. The results show that the drag force was approximately doubled, when nets were attached, compared to without. Since the towing speed were quite slow, compared to the speeds normally used in this particular towing tank, several repetitions were necessary to obtain credible results and it was therefore performed five repetitions of all towing speeds. It is observed that there were some scattering in the results, however not to significant. The greatest deviations are seen at the lower towing speeds. The main reason for this is most likely connected to vibrations in the towing carriage and to the fact that there were very small forces being measured. Other than that the deviations are no larger than what would be expected and the results seem reasonable.



**Figure 6.1:** Experimentally obtained mean drag force from towing of the two models; with and without nets attached. The models are shown in Figure 5.2. The mean curves represent the mean of all five repetition tests.

However to further validate the results, the mean force acting perpendicular to the towing direction was also measured, in addition to the roll/heel angle. The results of this can be seen in Figure 6.2.



(a) Experimentally obtained lift force

(b) Experimentally obtained roll/heel angle

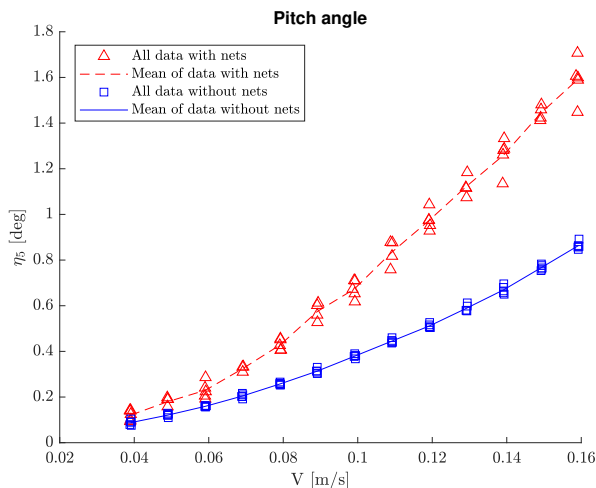
**Figure 6.2:** Experimentally obtained mean lift forces and mean roll/heel angles for all five repetition tests. The results indicate that the experimental towing setup was relatively symmetric, both with and without nets attached.



From the measurements of the mean lift force it is observed that the force mostly varies in the range of 0.1 N to  $-0.2$  N and that the mean lift force lies at around  $-0.05$  N. Indicating that there is some asymmetry in the towing configuration, but not anything major. It is expected that there will be some lack of symmetry, due to human errors in the setup of the towing system, both when it comes to getting the heading of the fish farm precise, but also when it comes to the angles of the four towing lines. As mentioned in Section 5.2 four force-transducers were used and the total force was thereby obtained by decomposing and adding together the forces in each towing line. To account for the fact that each towing line was not angled at precisely  $45^\circ$ , each angle had to be measured by hand, which might have resulted in some inaccuracy.

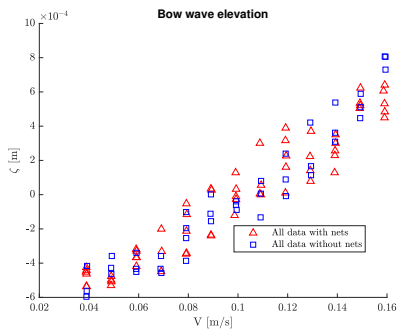
Looking at the roll/heel angles, it is observed that it spanned from  $-0.08^\circ$  to  $0.02^\circ$ , which might be considered as insignificant, thus implying that the heading of the fish farm was not too far off. If the heading had not been parallel to the towing tank, there would have been measured significantly larger roll angles as the fish farm pitched, since the inclinometer was placed at the center of the fish farm aligned with its transverse and longitudinal axis. Meaning pitch and roll were measured relative to these axes, independent of the actual heading of the fish farm relative to the towing tank. This further contributes to increase the reliability of the measured pitch/trim angles, which will be discussed next.

In addition to evaluating the symmetry of the system, it is also necessary to get an indication of the comparability between the two test configurations. In order to ensure that the flow conditions for each test configuration were as similar as possible, the fish farm was pretensioned significantly in order to minimize the pitch angle. The results achieved can be seen from the measured pitch angles in Figure 6.3.

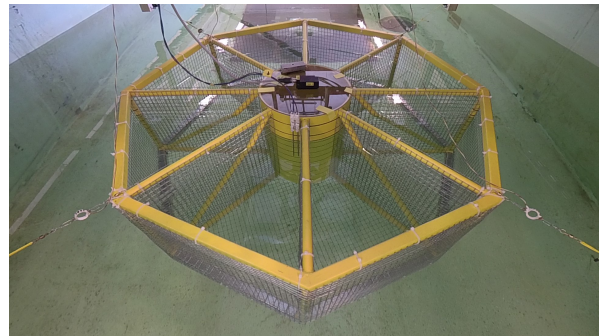


**Figure 6.3:** Experimentally obtained pitch/trim angle from towing of the two models; with and without nets attached. The models are shown in Figure 5.2. The mean curves represent the mean of all five repetition tests.

The measurements show that the the pitch angle increases with increased velocity and that the pitch angle becomes larger when nets are attached. Both of these tendencies are to be expected as the moment induced by the drag force will increase with higher velocity, as well as the drag force itself increases when nets are attached. It is further possible to observe that the largest difference in pitch angle between the two test configurations is no more than about  $1^\circ$  and one might therefore argue that the flow conditions for the fish farm with and without nets were quite similar. Even the largest pitch angle measured at  $1.8^\circ$ , could be considered as comparable to a case where there is no pitch at all, as the resulting error would be less than 1%. This is of relevance when it comes to the assumptions made in the calculations of the drag forces, which will be presented in the next section, as these assumed a model without any trim. The numeric calculations also assumed that the wave resistance could be neglected. To make sure that this was a valid assumption to make, the wave elevation at the front of the centre spar was measured and the results can be observed in Figure 6.4a.



(a) Measured surface elevation



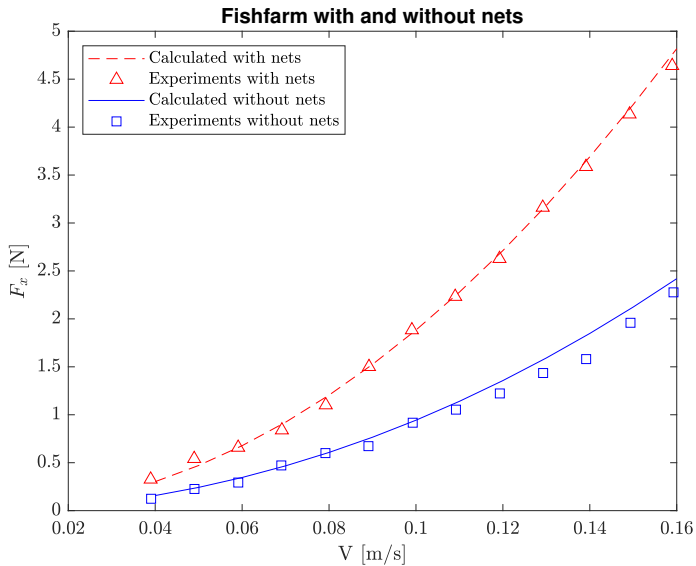
(b) Fish farm with nets during tow,  $V = 0.16$  m/s

**Figure 6.4:** Assessment of wave resistance in otherwise calm waters. Figure (a) presents the experimentally obtained surface elevation 2 cm in front of the centre spar from towing of the two models; with and without nets attached. The models are shown in Figure 5.2. The measurements account for the trim of the model. Figure (b) shows a picture of the model with nets being towed at the highest speed tested ( $V = 0.16$  m/s) and no significant waves can be seen.

Figure 6.4a presents the surface elevation at a point approximately 2 cm in front of the fish farm, taking pitch angle into account, since the wave probe was fastened to the spar. The results seem to indicate that no significant waves were created by the centre spar, as the measurements only range from  $-0.6$  mm to 1 mm. However this is only the results of the surface elevation at one single point and as the negative values indicates, this point is not necessarily measuring the peak of the bow wave. However the implications of the results was confirmed from visual observations, as no significant waves could be seen. A picture of the front of the fish farm during towing at the highest velocity, provided by Figure 6.4b, supports this further.

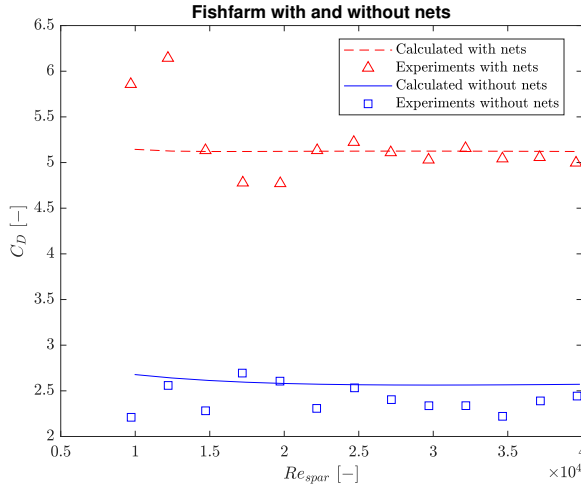
## 6.1.2 Comparison of experimental and numeric results

Numerical calculations were performed using the theory and numerical method as described in Section 4.1 in order to try and recreate the drag forces that were measured experimentally. As mentioned in the previous section, the numerical calculations assumed zero pitch/trim and neglected the wave resistance. Figure 6.5 below, provides a comparison between the calculated and experimental drag force, both with nets attached and without.



**Figure 6.5:** Comparison of experimentally obtained and numerically calculated drag forces in steady current, for the model with and without nets attached. The experimental values represents the mean of all repetition tests for the two models; with and without nets attached. The calculated values for the model without nets were obtained using drag coefficients for spar and columns as described in Section 4.1.2 and 4.1.3 and assuming non-separated potential flow. The calculations with nets used, in addition, screen-type load model for forces on nets and reduction factors as seen in Equation 3.82.

It is observed that the calculated drag force in both test configurations are in good compliance with the experimental results. What is curious is that the calculated drag force with nets seemed to predict even more accurate results than the calculations performed when nets were not present. A possible explanation for the slight overestimation of the drag force without nets, is most likely connected to the shading effects that some of the diagonal and vertical columns will experience, which was not taken into account in the calculations. To be more precise, some of the columns will be located directly in the wake of other columns, thus experiencing a reduced velocity, which in turn will reduce the drag force acting on them. While when nets were attached, reduction of the ambient flow velocity was taken into account for the columns, however not due to the presence of other columns, but rather the presence of the nets, as this was assumed to be dominating the characteristics of the flow in that case.



**Figure 6.6:** Comparison of experimental and calculated drag coefficients in steady current for model with and without nets attached. The drag coefficients are based on the results presented in Figure 6.5. The drag coefficients and Reynolds numbers are defined as described by Equation 6.1.

Having found the drag force both experimentally and numerically, it was further possible to calculate the drag coefficients, making it possible to observe how the drag changed with different Reynolds number. The results of which, are seen in Figure 6.6 above. Before moving forward it should be mentioned that the drag coefficient and Reynolds numbers presented in Figure 6.6 are defined as,

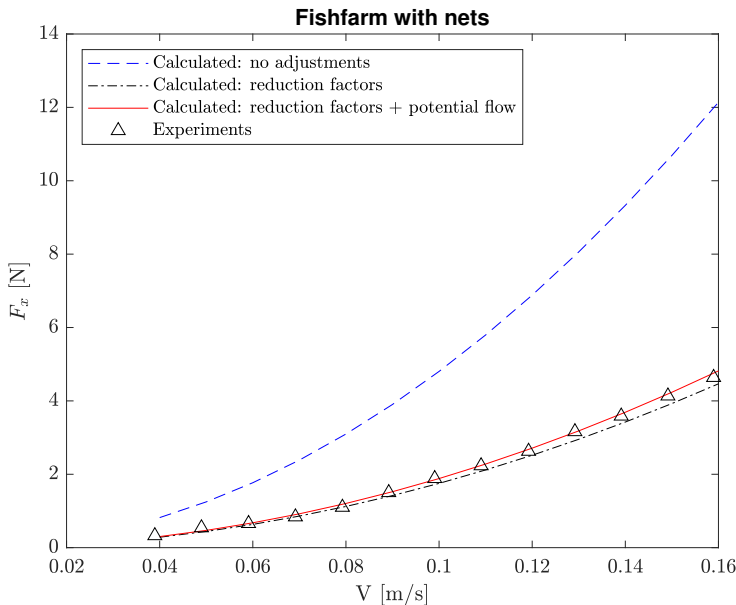
$$C_D = \frac{F_D}{\frac{1}{2}\rho V^2 A_{spar}} \quad \text{and} \quad Re_{spar} = \frac{D_{spar} V}{\nu}, \quad (6.1)$$

where  $V$  is the free-stream/towing velocity,  $A_{spar}$  is the projected area of the spar and  $D_{spar}$  is the diameter of the spar. From Figure 6.6 it is fairly easy to observe that the drag was approximately doubled when nets were attached, as mentioned previously. It is further observed from the experimental values that for both test configurations the variations with Reynolds number is greater at the lower velocities, where  $Re_{spar} < 1.75 \cdot 10^4$ , while it remain relatively unchanged at higher Reynolds numbers. In addition it is possible to see that the differences in the drag coefficient for  $Re_{spar} < 1.75 \cdot 10^4$  is greater when nets are attached, and that the drag coefficient of the fish farm with nets seem to increase with lower Reynolds numbers.

This is somewhat expected as the reduction of the velocity due to the nets will result in significantly lower Reynolds numbers for many of the columns, in addition to having very low Reynolds numbers for some of the nets. For instance, looking at Figure 3.2a the Reynolds numbers of the columns without nets will be in the range of  $640 - 2560$ , while the spar will be in the range of  $10^4 - 4 \cdot 10^4$  at the different towing speeds. In this range the columns and the spar will be in the subcritical flow regime and the drag coefficient does not change significantly.

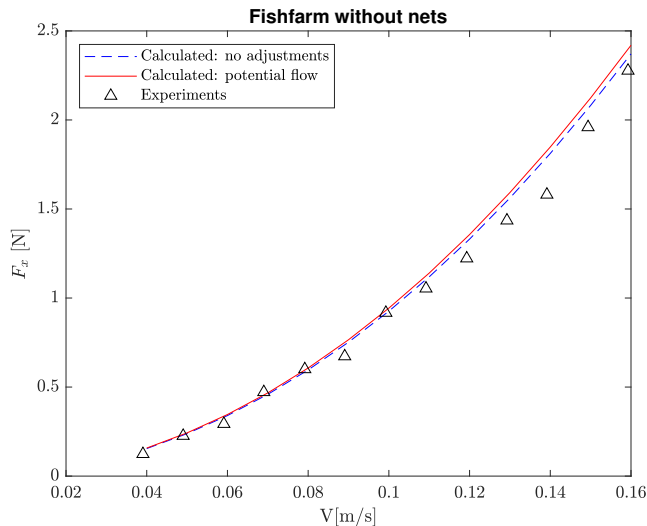
However when nets are attached, the Reynolds number for the columns will be as low as 100, meaning some of the columns will go from having a completely turbulent wake, to a laminar vortex street, thus increasing the drag. In addition the Reynolds number of the nets will vary from around 10 to approximately 210 at the different velocities and again looking at Figure 3.2a it is realized that the change in the drag coefficient gets more significant with lower Reynolds numbers. The very low Reynolds number of the nets might also be the reason that the numeric calculations of the drag coefficient with nets is not able to replicate the increased drag coefficients at the two lowest towing speeds. The reason being that Equation 3.78, which was used for the nets, is not valid for Reynolds numbers lower than 34. However it is still possible that the main reason for the deviations have to do with inaccuracies and noise in the measurements.

Further it is of interest to see how taking into account different assumptions regarding the flow, affects the numerical results. The calculations presented so far are the results of assuming a non-separated flow around the centre spar and taking into account reduction of flow velocities when nets were attached. Figure 6.7 and 6.8 presents the effect of different numerical approaches.



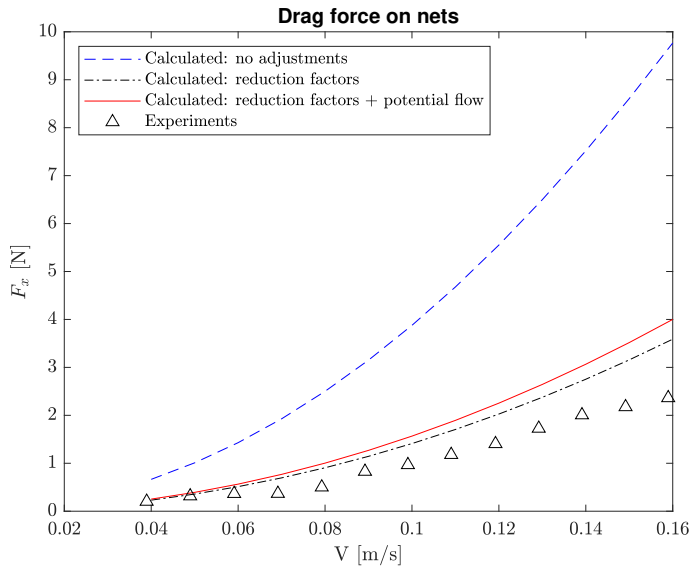
**Figure 6.7:** Comparison of different numerical approaches for calculating the drag of the fish farm with nets in steady current. The curves represents the calculated drag forces using respectively undisturbed flow, reduction factors and reduction factors, in combination with non-separated potential flow. The experimental values presented represent the mean of all five repetition tests for the fish farm with nets attached. A significant overestimation of the drag can be observed assuming undisturbed flow

Figure 6.7 shows how the different numerical approaches affected the calculated drag force for the fish farm with nets. The blue dashed line indicates the results obtained assuming an undisturbed uniform inflow on all of the structural components and it is observed that the total drag force was vastly overestimated, with a deviation of almost 160% compared to the experimental results. Building on this model, reduction factors were implemented and as the black dash-dotted line shows, the implementation of reduction factors resulted in a slight underestimation of the drag force. Further it was taken into account that the flow have to move around the centre spar, by assuming non-separated potential flow. This increased the total drag with approximately 7.4% and proved to yield results that were in quite good accordance with the experimental results. From the results one can clearly see that it is absolutely necessary to take into account flow reduction due to nets, in order to obtain good results. One can further state that there is a non-negligible increase in the drag forces, as a result of speed-up and change in flow direction around the centre spar, resulting in increased forces on the surrounding nets and columns. This increase however is mostly due to increased forces on the nets as will be clear from the next figures.



**Figure 6.8:** Comparison of different numerical approaches for fish farm without nets. The curves represents the calculated drag forces using respectively undisturbed flow and non-separated potential flow. The experimental values presented represent the mean of all five repetition tests for the fish farm without nets attached.

From Figure 6.8 it is observed that for the structure without nets, there is possible to obtain reasonable results, assuming an undisturbed flow. The effect of assuming a non-separated potential flow, was a minor increase in the total drag forces, mainly because of speed-up on the columns. The results further seem to suggest that in order to obtain even more accurate results at higher velocities, reduction of the flow due to wake interaction between columns and between spar and columns should be considered as well.



**Figure 6.9:** Comparison of different numerical approaches for calculating the forces on the net-panels. The curves represents the calculated drag forces using respectively undisturbed flow, reduction factors and reduction factors in combination with non-separated potential flow. The "experimental" values presented are found as the difference between the mean curves in Figure 6.1.

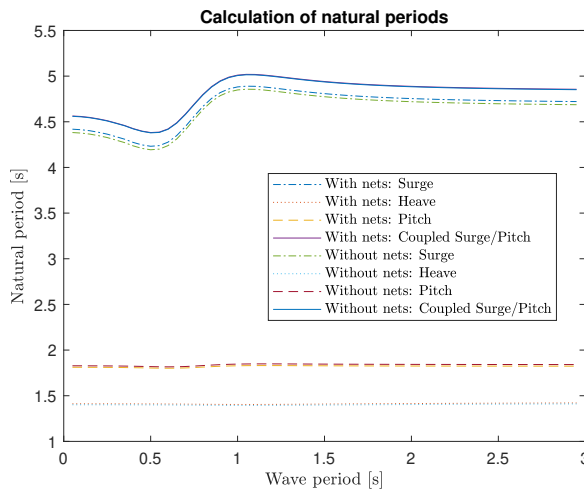
Figure 6.9 provides the calculated drag forces on nets only, assuming respectively undisturbed flow, reduced velocities due to nets and reduced velocities due to nets, in combination with non-separated potential flow. In addition what could be considered as the experimentally measured net-panel force, is presented. It is important to note that the "experimental" net-panel force is just found from the difference between the total drag forces with nets and without nets. Since the nets in reality results in decreased drag on the columns and the spar, the actual force on the nets will be larger than the measured difference between the two test configurations. This tendency might also be seen in Figure 6.9. Further it is observed that the net-panel forces are significantly overestimated when undisturbed flow is assumed. This force is however reduced greatly when reduction factors are implemented. Taking both reduction factors and flow around the centre spar into consideration, resulted in a noticeable increase in the drag force of roughly 10.8%, compared to when only reduction factors where used. The main reasons for the increased drag is due to local speed-up around the structure, in addition to the fact that the inflow will "hit" the internal nets in a more perpendicular manner when the flow moves around the spar, than what would be the case with assuming an undisturbed flow. It is also noticed that the net-panel forces obtained taking both reduction factors and flow around the centre spar into consideration, comprise of approximately 84.4% of the total drag force measured for the fish farm with nets.

### 6.1.3 Summary of experimental and calculated results in current

This section will summarize the most important results obtained from the towing tests and the corresponding numerical calculations. The experimental results showed that the total drag force on the structure is doubled when nets are attached. Furthermore the numerical calculations suggested that when nets are attached, the nets themselves comprise of approximately 84.4% of the total drag force. Furthermore it is realized that the implementation of reduction factors, when nets are present, is essential in order to not overestimate the drag forces. It is further understood that the effect of speed-up and change in the direction of the flow, due to the presence of a large-volume structure, should not be neglected when nets are in proximity to the structure, as this resulted in a noticeable increase of 10.8% on the net-panel forces. For the fish farm without nets on the other hand, assuming undisturbed flow proved to be adequate to achieve satisfactory results.

## 6.2 Natural periods

As mentioned previously the fish farm had to be ballasted with two different ballast configurations, one for when nets were attached and another one when the nets were taken off. The desired goal of the two ballast configurations were to obtain as equal natural periods as possible in order to ensure that the model without nets, could be considered comparable to the model with nets. Thus calculations, as described in Section 3.3, were performed to see if the aforementioned objective was achieved. The results of these calculations for the fish farm with and without nets can be seen in Figure 6.10.



**Figure 6.10:** Comparison of calculated natural periods in surge, heave, pitch and coupled surge/pitch for fish farm with and without nets, using the theory presented in Section 3.3. Depicting only minor differences in the natural periods for the two test configurations.



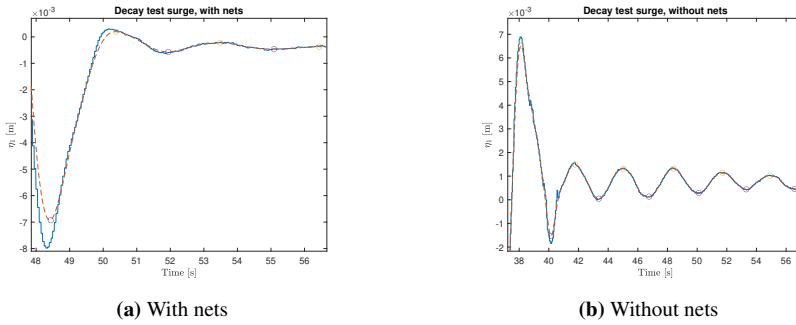
As seen from Figure 6.10 the calculated results suggested that the natural periods should be more or less equal for the two test configurations. It is also noted that as a result of the soft springs used in the mooring system, the fish-farm should act as if it was slack moored. Usually slack moored offshore structures, have a natural period in surge/sway of around 100 s. The calculations indicated that the natural period in surge should be approximately 4.7 s, which when scaled to full-scale corresponds to a period of roughly 59.5 s. Even though the natural period achieved is not as long as for most slack moored structures, it is still significantly longer than the wave periods examined. This should therefore result in mass-dominated response of the fish farm in surge, as desired.

Furthermore before testing in each configuration, there were performed decay tests in order to try and further validate the comparability between the different test configurations. This was done by using the principle of logarithmic decrement as described in Section 3.3, in order to obtain the natural periods. Figures from the calculations might be found in Appendix E. There should be mentioned that due to the coupling between surge and pitch, it was not possible to excite pure surge or pure pitch motion. Therefore it was only possible to obtain the coupled natural period between surge and pitch. Time-series of the decay tests performed depicting the surge, heave and pitch motion, both with and without nets, can be seen in Figure 6.11, 6.12 and 6.13 respectively. From the time-series it is observed that the motions decay significantly faster when nets are attached as opposed to when they are not, as a result of the increased damping provided by the nets. It is further noted that in general, the surge and pitch motion were damped out more rapidly than the heave motion, due to the coupling and more damping in these degrees of freedom. The results obtained for the natural periods from both analytical calculations and decay tests are presented in Table 6.1. The calculated natural periods presented in the table are taken from Figure 6.10, evaluated at the largest wave period.

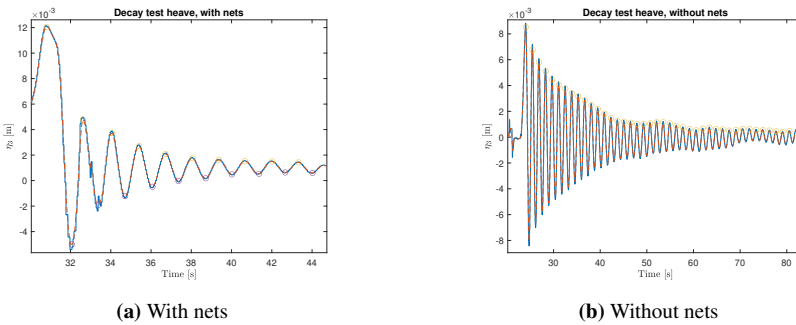
**Table 6.1:** Natural periods obtained from experimental decay tests and from analytical calculations. The calculated analytical values are taken from the curves in Figure 6.10, evaluated at longest wave period.

	With nets		Without nets	
	<i>Calculated</i>	<i>Experimental</i>	<i>Calculated</i>	<i>Experimental</i>
$T_1$ [s]	4.7213	3.2013(coupled)	4.6870	3.4840(coupled)
$T_3$ [s]	1.4210	1.3900	1.4104	1.4129
$T_5$ [s]	1.8237	3.3350(coupled)	1.8414	3.4282(coupled)
$T_{15}$ [s]	4.8559	3.2013/3.3350	4.8515	3.4840/3.4282

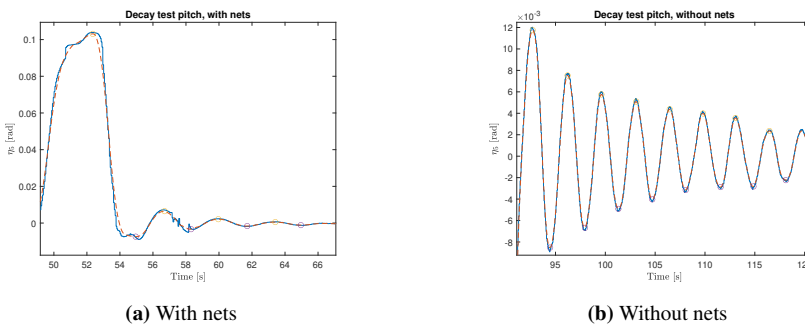
From the table above it is observed that both the calculated and the experimental values of the natural period in heave were in accordance with each other, both with and without nets. The coupled natural periods however indicated that there might be a difference between the numeric and experimental model, when it comes to the coupled surge and pitch motion. However this is hard to say with absolute certainty as the coupled natural periods from the decay tests were found based on a limited number of peaks and troughs as indicated by the circles in Figure 6.11 and 6.13. However the decay tests at least suggest that the coupled surge and pitch motion for the two test configurations, might be considered as comparable.



**Figure 6.11:** Time-series of surge motion during experimental decay tests, for model with and without nets attached. The circles indicate peaks/troughs used in calculation of the logarithmic decrement.



**Figure 6.12:** Time-series of heave motion during experimental decay tests, for model with and without nets attached. The circles indicate peaks/troughs used in calculation of the logarithmic decrement.



**Figure 6.13:** Time-series of pitch motion during experimental decay tests, for model with and without nets attached. The circles indicate peaks/troughs used in calculation of the logarithmic decrement.

## 6.3 Experimental and numerical results in regular waves

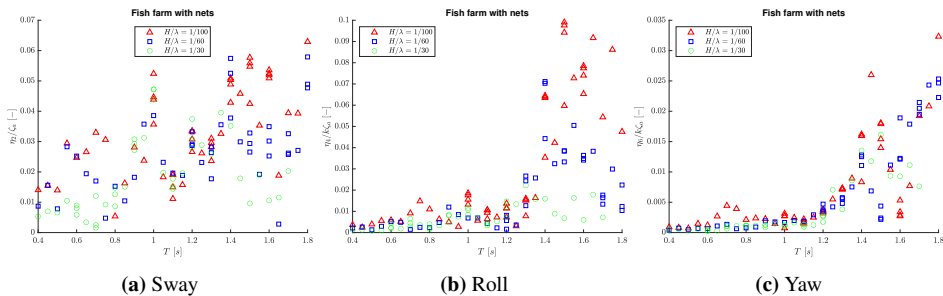
In the following sections the experimental results obtained from tests in regular waves with three different wave steepnesses and wave periods ranging from 0.4 s to 1.8 s, at a water depth of 0.8 m will be presented. Further there will be presented comparisons between the experimental results obtained for the fish farm with and without nets attached. In addition there will be presented numerical calculations assessing the importance of considering a diffracted wave profile versus undisturbed incident waves, to be acting on the nets and columns surrounding the centre spar, both in terms of the response on the entire structure and considering the forces acting on the nets.

### 6.3.1 Experimental results

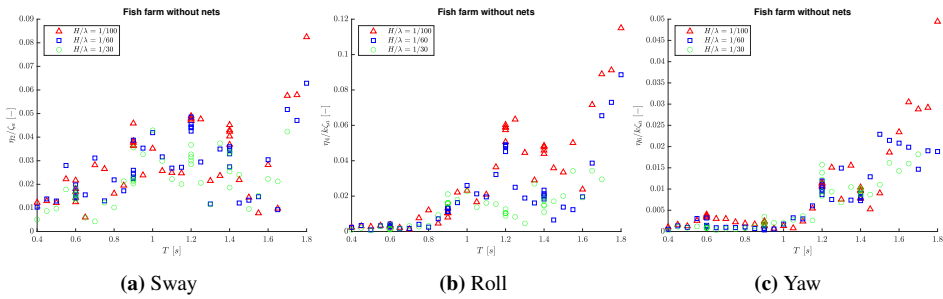
The experimental results presented in this section were obtained by generating 100 waves for each wave period and thereafter evaluating the measurement signals for the time periods where steady state conditions were reached. It is further noted that all phases presented are found relative to the wave elevation at the center of the fish farm. With respect to the phases it must also be mentioned that positive values indicate lag.

#### Assessment of symmetry

In order to be able to only excite surge, heave and pitch of the fish farm, symmetry both in the mooring system, heading and the test setup in general had to be achieved. Figure 6.14 and 6.15 provides the RAOs in sway, roll and yaw for the fish farm both with and without nets. All experimental results for roll, sway and surge might be found in Appendix C.



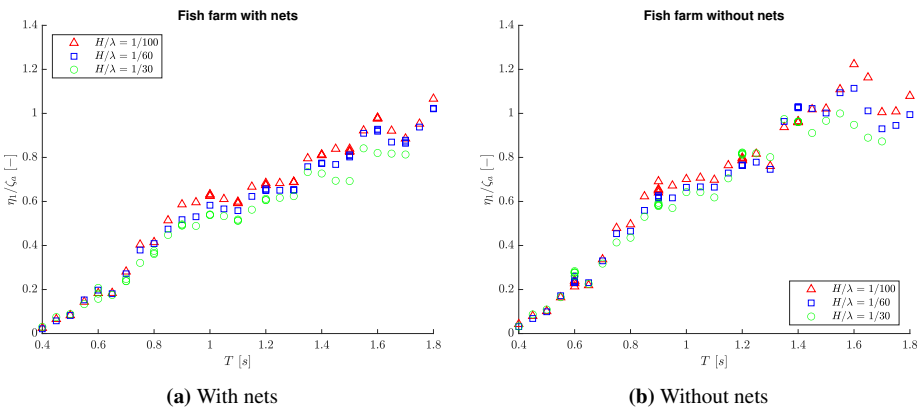
**Figure 6.14:** Experimental sway, roll and yaw RAOs for model with nets. Obtained for three different wave steepnesses;  $H/\lambda = 1/100$ ,  $H/\lambda = 1/60$  and  $H/\lambda = 1/30$ . Only minor response is observed in sway, roll and yaw, indicating adequate symmetry in the experimental setup.



**Figure 6.15:** Experimental sway, roll and yaw RAOs for model without nets. Obtained for three different wave steepnesses;  $H/\lambda = 1/100$ ,  $H/\lambda = 1/60$  and  $H/\lambda = 1/30$ . Only minor response is observed in sway, roll and yaw, indicating adequate symmetry in the experimental setup.

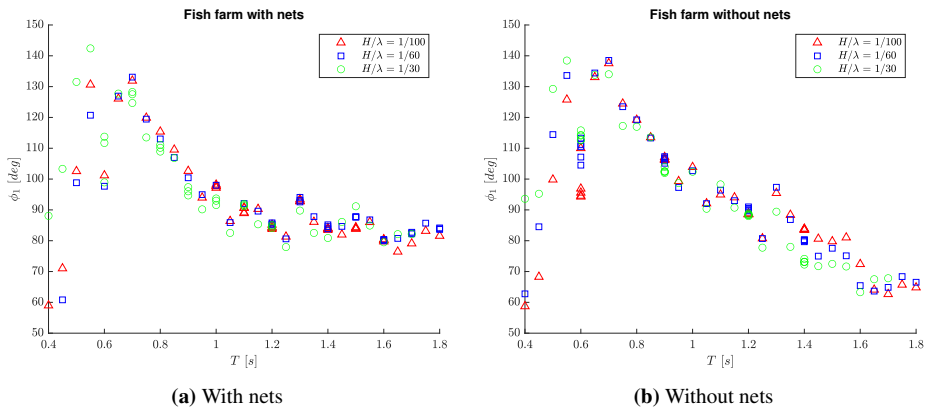
From Figure 6.14 and 6.15 it can be seen that there were very little sway and yaw motions, indicating that the heading and mooring system was relatively symmetric. For roll however it could be seen slightly larger motions especially at longer wave periods. This however is possibly more related to the measurement of the location of the placement of the reflective spheres used for tracking the motions. In any case the results seem to indicate that the symmetry of the test setup was relatively good, but that there is a minor inaccuracy in the results. However not any more than what would have been expected.

**Surge**



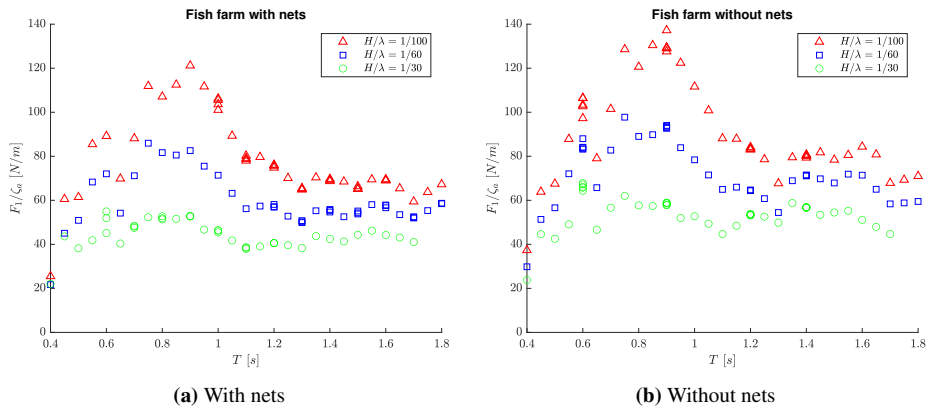
**Figure 6.16:** Experimental surge RAOs for model with and without nets. Obtained for three different wave steepnesses;  $H/\lambda = 1/100$ ,  $H/\lambda = 1/60$  and  $H/\lambda = 1/30$ . The results show a slight decrease in the surge motion when nets are attached and only a minor amplitude dependency for both models.

Looking at Figure 6.16 it can be seen that the surge motion increases slightly when nets are not attached to the model. Thus seemingly suggesting that the nets to a greater extent provides a dampening effect, as opposed to excite the fish farm any further in surge. Another possible reason for the reduced surge motion might be because of the increased inertia of the structure with nets. It can further be seen that the amplitude dependency in surge is not very pronounced, most likely since the wave period range considered will be in the mass-dominated response region as the natural periods in surge are significantly longer than the wave periods tested. Larger differences might be expected to occur both in terms of amplitude dependency and between the two test configurations if longer wave periods had been tested.



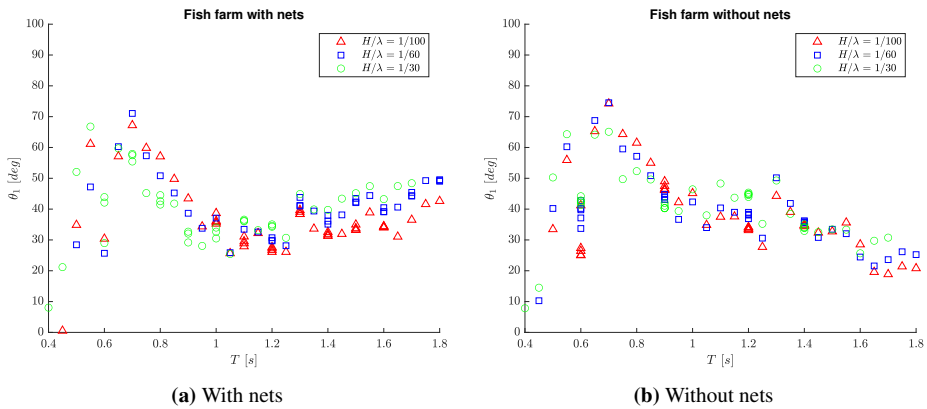
**Figure 6.17:** Experimental surge phases for model with and without nets. Obtained for three different wave steepnesses;  $H/\lambda = 1/100$ ,  $H/\lambda = 1/60$  and  $H/\lambda = 1/30$ . Scattered results are seen for  $T < 0.7s$ , likely due to diffraction and reflection of waves.

From Figure 6.17 it is seen that for both test configurations, the surge phases start to scatter for wave periods lower than about 0.7 s. The most likely explanation for this is that waves are being scattered and reflected by the centre spar, as wave diffraction should start playing a role for the centre spar for wave periods lower than about 0.9 s. However, apart from that, it is observed that for the lower wave periods, the response tends towards being  $180^\circ$  out of phase. Furthermore in both test configurations, the phases do not change significantly with different wave steepnesses. A clear distinction between the two test configurations can be seen for the longer wave periods, as the fish farm with nets is roughly  $90^\circ$  out of phase with the wave elevation, while the phase of the fish farm without nets continuous to decrease. It is expected that the phase of the surge motions should be lagging with about  $90^\circ$ . Since the surge excitation will be dominated by inertia forces, where the horizontal water particle acceleration leads the waves with  $90^\circ$  and knowing that the periods considered are much lower than the natural period which in turn should result in mass-dominated response. With mass dominated response the motions lag the excitation force with  $180^\circ$ , thus  $90^\circ$  lag in the surge motion should make sense. The main reason why the phase continuous to decrease for the fish farm without nets is likely to be related to coupling with large pitch motions.



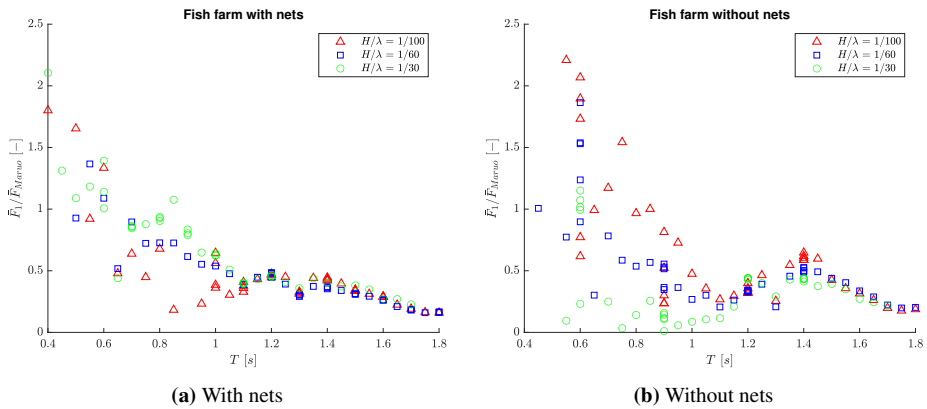
**Figure 6.18:** Experimental mooring system surge force RAOs for model with and without nets. Obtained for three different wave steepnesses;  $H/\lambda = 1/100$ ,  $H/\lambda = 1/60$  and  $H/\lambda = 1/30$ . The results depict a pronounced amplitude dependency, likely as a result of drag on nets and columns.

From the measurements of the mooring system force in surge provided in Figure 6.18, it is observed that both with and without nets, there is a clear peak for all wave steepnesses at a period of approximately 0.9 s. As mentioned previously this is the limit where diffraction forces starts to matter for the spar and these peaks might have some connection with that. Another perhaps more plausible explanation is that this wave period corresponds to a wavelength of 1.26 m, which is slightly larger than the total diameter of the fish farm, possibly resulting in an additive effect between the different excitation forces. It can further be seen that the mooring force is larger when nets are not attached, as is expected since the fish farm surged more without nets. There is also a pronounced amplitude dependency, where the forces decrease with increased wave steepness, as a result of drag on both nets and columns. Since this amplitude dependency seem to be quite similar in both test configurations around  $T = 0.9$  s, it is likely that this occurs as the drag coefficients of the columns increase with larger  $KC$ -numbers, as seen in Figure 3.9, thus increasing the damping and reducing the mooring system forces. From Figure 3.9 it is found that the  $KC$ -numbers of the vertical columns will range from around 5, with  $H/\lambda = 1/100$ , to about 16.5 for  $H/\lambda = 1/30$ , when  $T = 0.9$  s. This is a range where the drag coefficients of the columns increase drastically as a function of the  $KC$ -number.



**Figure 6.19:** Experimental mooring system surge force phases for model with and without nets. Obtained for three different wave steepnesses;  $H/\lambda = 1/100$ ,  $H/\lambda = 1/60$  and  $H/\lambda = 1/30$ .

Looking at the phases of the mooring system force in surge from Figure 6.19, it is observed that they are quite different from the phases of the surge motion, which is somewhat unexpected since the surge stiffness force from the mooring system should be in phase with the surge motion. However this is likely due to coupling with both heave and pitch, as the mooring system forces was found by decomposing the force of each mooring line and adding them together for each time instant. Thus the location of each attachment point and the direction of the mooring line will change each time-instant according to the motion in surge, pitch and heave. Other than that it is observed that the phases are relatively equal for wave periods ranging from 0.7 s to 1.2 s, and for wave periods lower than this range the phases start to scatter once again, likely due to the diffraction and reflection of waves by the centre spar. For periods longer than 1.2 s it is observed that the phases for the fish farm with nets start to increase, while without nets, the phases continuous to decrease, most likely as a result of large differences in the pitch motion at the longer periods.



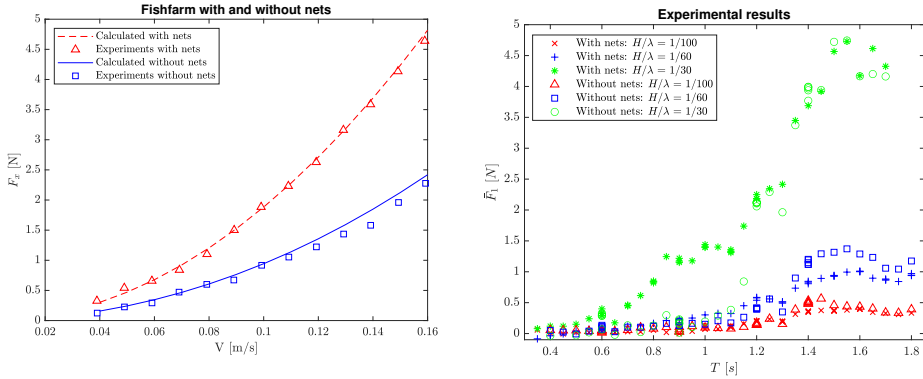
**Figure 6.20:** Experimental mean surge force for model with and without nets. Obtained for three different wave steepnesses;  $H/\lambda = 1/100$ ,  $H/\lambda = 1/60$  and  $H/\lambda = 1/30$ . Non-dimensionalized by dividing the mean of the measured mooring system force with the asymptotic value of Maruo's formula for a vertical cylinder in finite water depth provided in Equation 3.98.

The mean forces measured from the experiments are provided in Figure 6.20, and have been made dimensionless, by dividing the force with the asymptotic value for the mean force for a vertical spar at finite water depth, as described by Equation 3.98. It is observed that for both test configurations, there is a peak at wave period equal to 1.4 s, which coincides with the natural period in heave and it is observed that it corresponds to roughly half the asymptotic value provided by Maruo. The peaks are to be expected if one looks at Figure 3.8, since there will be generated a lot of waves at heave resonance, thus increasing the mean forces. This peak is slightly smaller when nets are attached, which might suggest that the nets actually decrease the mean force in surge, most likely due to the bottom net increasing the damping in heave, thus resulting smaller heave motions and less waves being generated. It can also be seen for both test configurations, that at longer wave periods the non-dimensionalized mean force is decreasing towards zero, as is expected.

For the shorter wave periods,  $T < 1.1\text{ s}$ , on the other hand there seems to be an increase in the mean forces in both cases as expected, however large scattering between the measurement is observed as well. The trends seem to indicate that for the fish farm with nets, the non-dimensionalized mean forces increase with increased wave steepness, possibly because of increased importance of drag on the nets contributing to increased mean forces. However when nets are not attached the trend is opposite, with increasing mean forces for less steep waves. The credibility of the results at the shortest wave periods are however somewhat questionable as the forces measured in these cases were quite small, as can be seen in Figure 6.21b. Thus any drift in the measurements from the force transducers will have a significant impact on the non-dimensionalized results.



It is further of interest to study the order of the mean drift forces compared to the current forces, especially in terms of dimensioning of mooring systems. The next figure presented will therefore provide a comparison of the two force components.



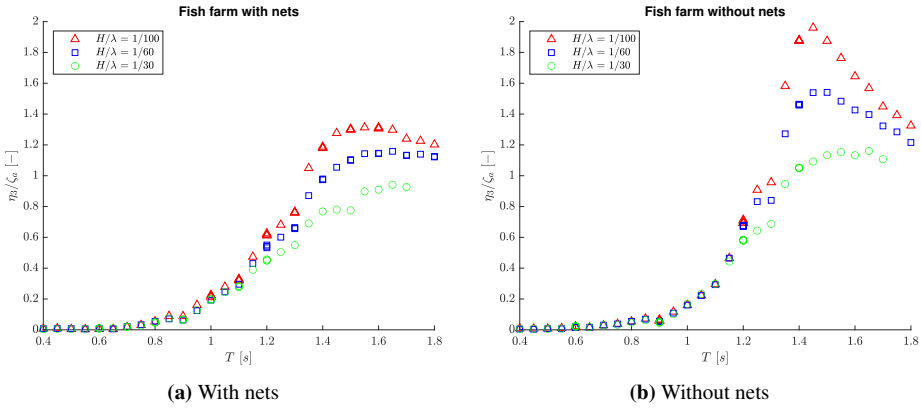
(a) Calculated and experimental drag force in steady current, for fish farm with and without nets

(b) Experimental mean drift forces

**Figure 6.21:** Comparison of the order of magnitude between mean drag forces and experimentally obtained mean wave-drift forces, for model with and without nets attached. The wave-drift forces were obtained for three different wave steepnesses;  $H/\lambda = 1/100$ ,  $H/\lambda = 1/60$  and  $H/\lambda = 1/30$ . It is observed that the two force contributions are in the same order of magnitude.

Looking at Figure 6.21 it is observed for the fish farm with nets, that for the steepest waves the mean wave-drift forces are almost as large as the drag forces from pure current. In addition it is observed that in this case, the mean wave-drift force increase with longer wave periods in a quite similar manner as the drag forces increase with larger current speeds. Thus implying that for many combinations of steep waves at different wave periods and different current speeds, there will be an equal importance between the two force contributions on the mean forces experienced by the mooring system. While for the fish farm without nets, the steepest waves result in mean forces almost twice as large as the largest current forces measured for the fish farm without nets. Indicating that, when large heave motions are excited, the wave-drift force might be significantly larger than the current forces. Even the mean wave-drift force for the least steep waves, in both test configurations, will close to heave resonance be comparable to the drag forces from current for a wide range of current velocities.

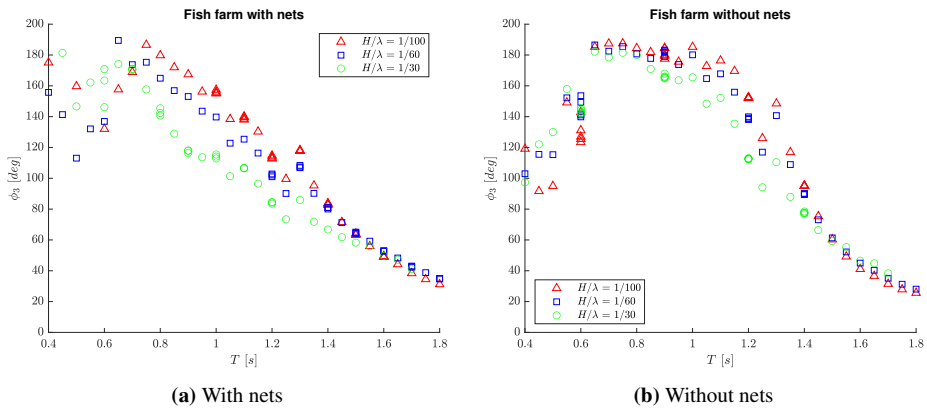
## Heave



**Figure 6.22:** Experimental heave RAOs for model with and without nets. Obtained for three different wave steepnesses;  $H/\lambda = 1/100$ ,  $H/\lambda = 1/60$  and  $H/\lambda = 1/30$ . The results show both increased response and increased amplitude dependency for the model without nets.

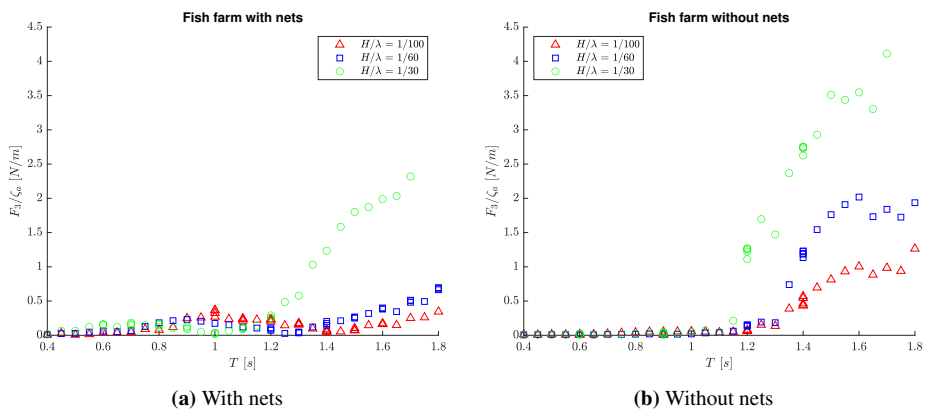
There can be seen a clear distinction between the model with nets and without nets, when looking at the heave RAOs in Figure 6.22. First off, the heave motion is significantly damped at resonance, when nets are attached, as expected due to increased viscous damping provided by the nets, the bottom net in particular. It can further be observed that the amplitude dependency is greater around resonance without nets, than with nets. The reason for this might be that when nets are not attached, the viscous damping will mostly be provided by the columns. Further it is known that the drag coefficients of the columns will be significantly more dependent on the amplitude than what would be the case for the nets. Thus it is to expect that the amplitude dependency is greater without nets attached to the model. Other than that the RAOs seem reasonable and all of them converges towards 1 for the longer wave periods, as should be expected.

### 6.3 Experimental and numerical results in regular waves



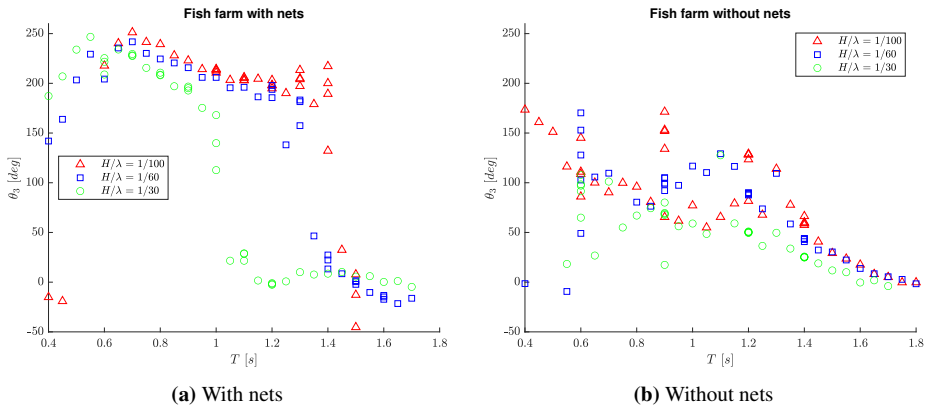
**Figure 6.23:** Experimental heave phases for model with and without nets. Obtained for three different wave steepnesses;  $H/\lambda = 1/100$ ,  $H/\lambda = 1/60$  and  $H/\lambda = 1/30$ . The results show that the phases approach  $0^\circ$  for longer wave periods more rapidly when nets are attached, mainly due to increased damping.

Looking at Figure 6.23 it is observed that the heave motion in both cases move from being  $180^\circ$  out of phase with the waves for the shortest wave periods, to being increasingly more in phase with the waves as the wave periods gets longer, as expected. It is further noted that in both cases the heave motion is approximately  $90^\circ$  out of phase with the waves at a wave period equal to the natural period in heave. It can also be seen that the transition from being  $180^\circ$  out of phase to being in phase with the waves occurs more smoothly for the fish farm with nets, than the fish farm without nets. This is most likely as a result of the increased damping the nets will provide.



**Figure 6.24:** Experimental mooring system heave force RAOs for model with and without nets. Obtained for three different wave steepnesses;  $H/\lambda = 1/100$ ,  $H/\lambda = 1/60$  and  $H/\lambda = 1/30$ . Pronounced differences between the two models can be seen at the longer wave periods.

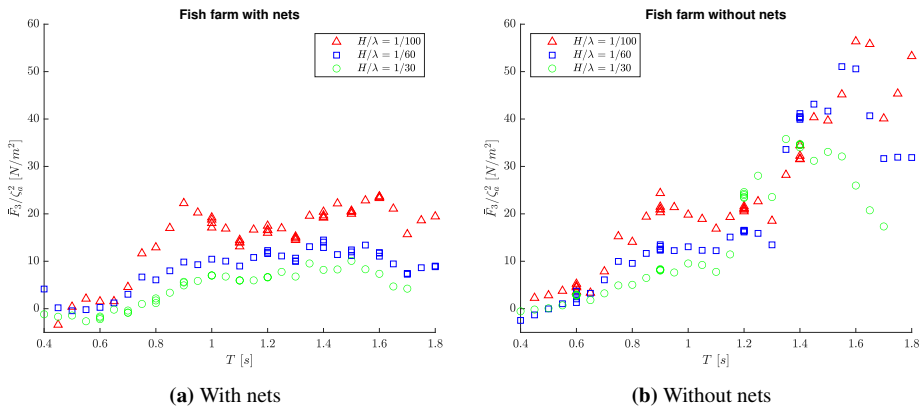
The mooring system heave force is presented in Figure 6.24 and as expected the forces measured are not very large, as the mooring system was more or less horizontal, with relatively long mooring lines. It can be seen that the measured heave force was larger for the fish farm without nets for wave periods longer than 1.2 s. In addition, for the fish farm without nets a distinct amplitude dependency at the longest wave periods could be observed. This is most likely connected with coupled heave, surge and pitch motions at the attachment points of the mooring system. It is suspected that large pitch motions could be the primary reason for these results. Looking at the results from the steepest waves, for the fish farm with nets it is observed that the force increased substantially, compared to the other wave steepnesses, and it is not quite clear what caused this to occur. It should be mentioned that since the forces measured in heave are so small, there is a chance that measurement noise, force transducer getting wet and possibly mooring lines getting submerged could have affected the results.



**Figure 6.25:** Experimental mooring system heave force phases for model with and without nets. Obtained for three different wave steepnesses;  $H/\lambda = 1/100$ ,  $H/\lambda = 1/60$  and  $H/\lambda = 1/30$ . Pronounced differences between the two models can be seen for the entire range of wave periods.

From the mooring system heave force phases in Figure 6.25 it is once again observed some strange behaviour for the fish farm with nets at the steepest waves. The results seem to indicate that the transition from being over  $180^\circ$  out of phase to being in phase with the waves, occur at a shorter wave period for the largest wave steepness. While for the two other wave steepnesses this transition occurs around the natural period in heave as expected. Further it can be seen that the heave force phases without nets, scatter significantly more than the phases with nets. This might have something to do with large pitch motions. Either in terms of a coupling effect or possibly because of force transducers getting wet, resulting in disruptions in the measurements.

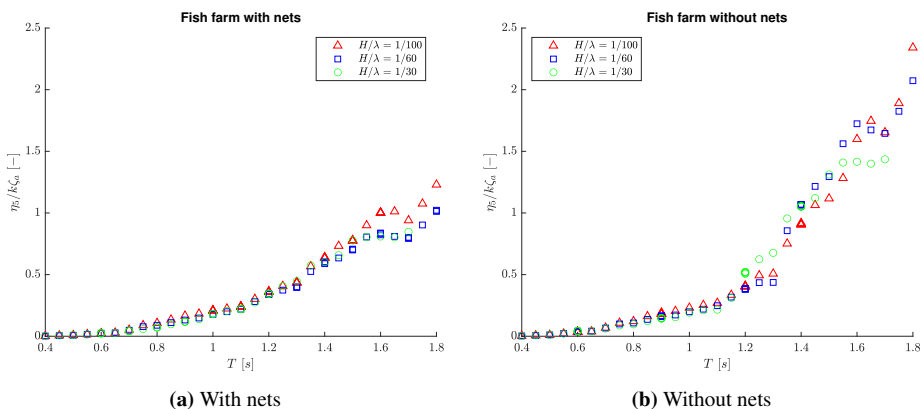
### 6.3 Experimental and numerical results in regular waves



**Figure 6.26:** Experimental mean heave force RAOs for model with and without nets. Obtained for three different wave steepnesses;  $H/\lambda = 1/100$ ,  $H/\lambda = 1/60$  and  $H/\lambda = 1/30$ . From (a) it is clearly seen that the mean forces increase with increased relative motions.

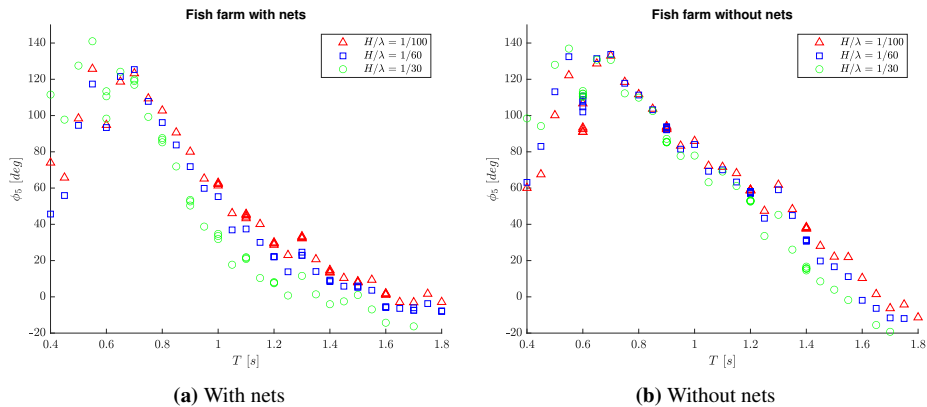
Looking at the measured mean forces in heave from Figure 6.26, it is observed that the mean forces for both test configurations are very similar for wave periods up to about 1.1 s and could be a result of comparable motions between the two test configurations for this range of wave periods. For longer wave periods the mean forces get larger for the model without nets attached, likely as a result of increased pitch motions. It is further noticed that the general trend in both cases, points towards the mean forces getting larger with less steep waves. All of these results seem to indicate that the mean heave forces are connected with the amplitude of the relative motions between the fish farm and the waves.

#### Pitch



**Figure 6.27:** Experimental pitch RAOs for model with and without nets. Obtained for three different wave steepnesses;  $H/\lambda = 1/100$ ,  $H/\lambda = 1/60$  and  $H/\lambda = 1/30$ . A substantial increase in the pitch motion is observed for the model without nets.

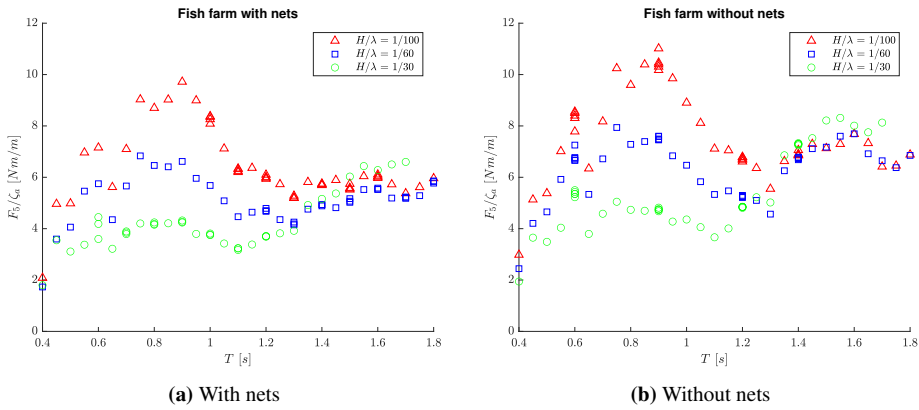
From the pitch RAOs provided in Figure 6.27 it is observed that the pitch motion is increased considerably, for the fish farm without nets, for wave periods larger than 1.2 s. For the wave period range from 1.2 s to about 1.5 s this is likely due to the fish farm with nets having a slightly larger moment of inertia in pitch than the fish farm without nets. The reason being that the response in this region still will be mass dominated. For periods larger than 1.5 s the response will tend towards getting more damping dominated, as it is approaching pitch resonance at about 1.8 s. Thus the reduced response for the fish farm with nets is expected to occur because of an increased damping in pitch caused by the nets. It is in addition possible to see that the only pronounced amplitude dependency is observed for wave periods larger than about 1.5 s, further supporting the expected increased importance of viscous damping in this upper region of wave periods.



**Figure 6.28:** Experimental pitch phases for model with and without nets. Obtained for three different wave steepnesses;  $H/\lambda = 1/100$ ,  $H/\lambda = 1/60$  and  $H/\lambda = 1/30$ . The results show that the phases approach  $0^\circ$  for longer wave periods more rapidly when nets are attached, mainly due to increased damping.

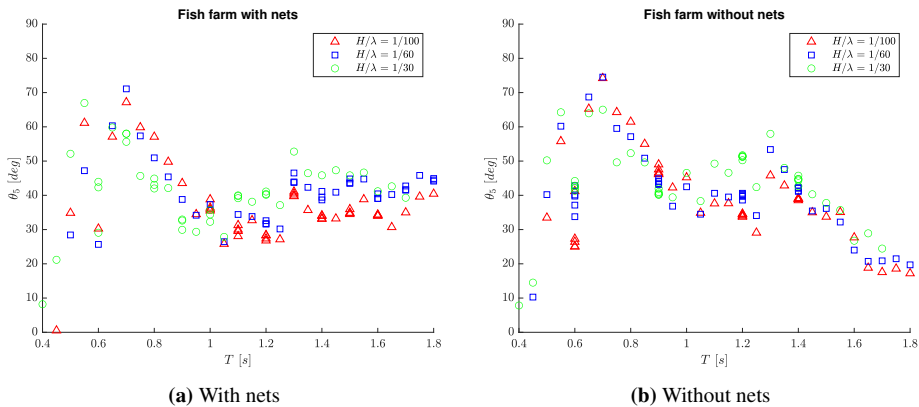
From the measured phases in pitch, it is seen that the response lags significantly, due to mass dominated response for the shortest wave periods, disregarding the phases measured for wave periods shorter than 0.7 s as diffraction and reflection of wave makes it hard to establish a definite phase in this region. As the wave periods approach pitch resonance, the pitch motion starts to move in phase with the waves. This might seem counter-intuitive at first, but one should realize that the pitch motion then in fact will be  $90^\circ$  out of phase with the wave slope, which should be expected at damping dominated response. It is further seen that with increased wave steepness and when nets are attached, the pitch phases seem to more quickly move towards being in phase with the waves, which likely is connected to increased viscous damping.

### 6.3 Experimental and numerical results in regular waves



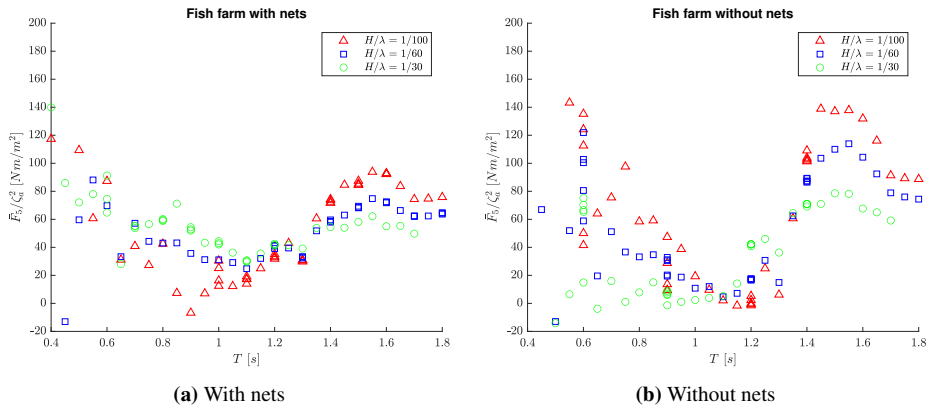
**Figure 6.29:** Experimental mooring system pitch moment RAOs for model with and without nets. Obtained for three different wave steepnesses;  $H/\lambda = 1/100$ ,  $H/\lambda = 1/60$  and  $H/\lambda = 1/30$ . Similarities with the surge force RAOs presented in Figure 6.18 can be observed.

From the measured mooring system pitch moments in Figure 6.29 it can be seen quite clearly that the pitch moment and surge forces presented in Figure 6.18 are coupled, as the same tendencies are observed for wave periods up to 1.3 s. For wave periods larger than this, the pitch moments increase, but this is possibly more related to the increased mooring system heave force that occurs in this wave period region. Other than that it is observed that the pitch moments in general were larger when the fish farm was tested without nets.



**Figure 6.30:** Experimental mooring system pitch moment phases for model with and without nets. Obtained for three different wave steepnesses;  $H/\lambda = 1/100$ ,  $H/\lambda = 1/60$  and  $H/\lambda = 1/30$ . Similarities with the surge force phases presented in Figure 6.19 can be observed.

From the measured mooring system pitch moment phases presented in Figure 6.30 it is once again observed significant coupling with surge, as the phases are very similar to the phases of the mooring system surge force phases seen in Figure 6.19.



**Figure 6.31:** Experimental mean pitch moment RAOs for model with and without nets. Obtained for three different wave steepnesses;  $H/\lambda = 1/100$ ,  $H/\lambda = 1/60$  and  $H/\lambda = 1/30$ . The results show distinct peaks at for all wave steepnesses around heave resonance.

From Figure 6.31 it is observed that the mean pitch moments measured is larger for for the fish farm without nets. For both test configurations it appears to be peaks in the mean pitch moment, that increase with lower wave steepness, for wave periods around 1.5 s. It is around this period that the largest heave motions were observed, which coincidentally also increase with lower wave steepness. Thus it is seen clearly that the mean forces increase with larger relative motions between the structure and the waves, as expected. There is further observed an increase in the mean pitch moments at the lower wave periods, which likely is related to the increased mean forces in surge as reflection of waves becomes increasingly important. However the issue of measurement noise and possible drift in the force transducer must be considered for the shortest wave periods as the measured forces were quite small for these wave periods.

### Summary of experimental results in waves

To summarize, the experimental results obtained seem reasonable. With respect to the motions it was observed that in general, these were larger for the fish farm without nets, where the most pronounced differences were in heave and in pitch. The increased motions further resulted in increased oscillatory forces on the mooring system, for the fish farm without nets. Concerning the mean forces these were in most cases smaller, when nets were attached to the fish farm and is possibly a result of reduced relative motions between the fish farm and the waves. However it was found that even when nets were attached, the wave-drift forces might still be just as important for the mean surge forces experienced by the mooring system, as the drag forces from pure current.



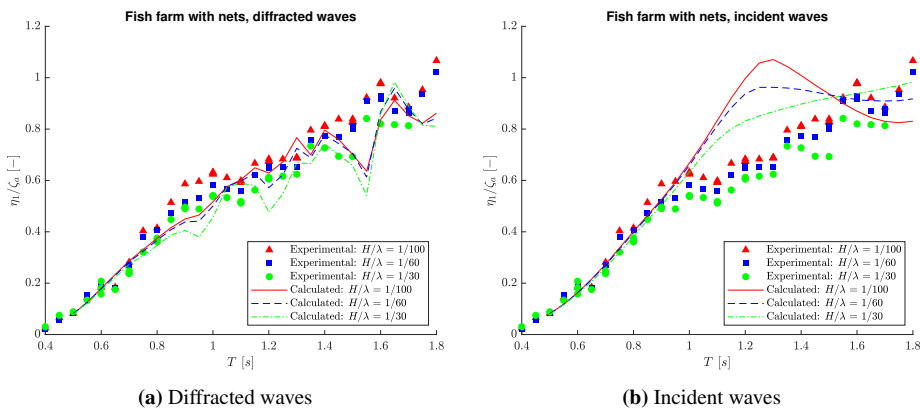
Still there are several uncertainties and possible errors related to the experiments. For instance, asymmetry with regards to the heading of the fish farm and with respect to the mooring system. The RAOs in sway, roll and yaw indicated that there were some asymmetry, but not any more than what would be expected. There were also observed for the longest wave periods and steepest waves, that the aft mooring lines went slack, while parts of the frontal mooring lines were submerged, in addition the frontal force transducers got wet.

All of this might have affected the measurements. There is also some uncertainty regarding the accuracy of the exact location of the reflective spheres used for tracking the motions of the fish farm. The reason being that the position of one of the spheres relative to the desired origo (centre of water-plane area), had to be measured by hand.

### 6.3.2 Comparison numerical and experimental results

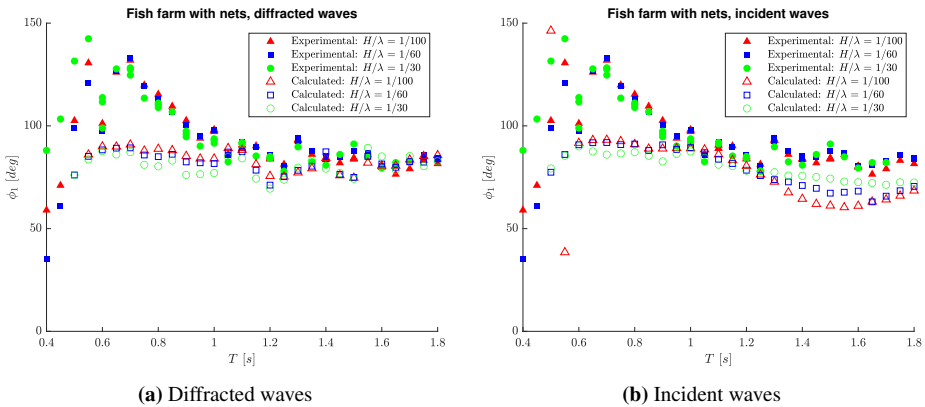
There were in addition performed calculations in order to try and validate the experimental results obtained and to assess the importance of considering a disturbed/diffracted wave profile, when calculating the forces acting on the columns and the nets surrounding the centre spar. As a result, a diffracted wave pattern taking into account the presence of the centre spar has been used and further compared to calculations assuming undisturbed incident waves. Calculated RAOs and phases in surge, heave and pitch for the fish farm with and without nets will therefore be presented next.

#### With nets



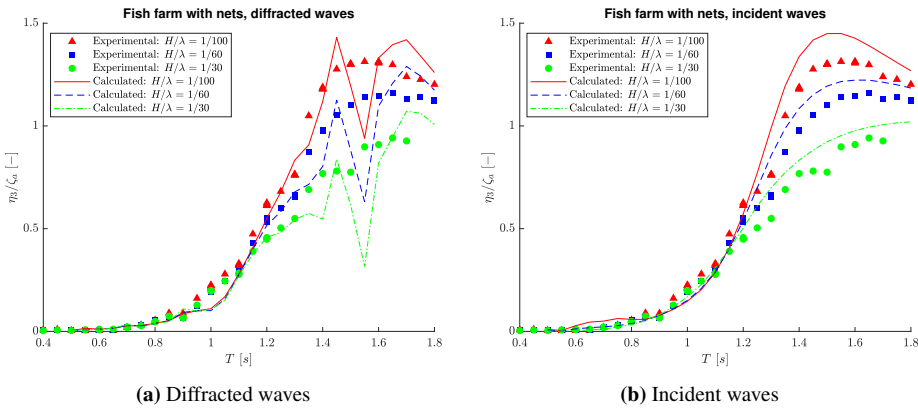
**Figure 6.32:** Comparison of numerically calculated surge RAOs, plotted alongside experimentally obtained surge RAOs, for model with nets attached. Three wave steepnesses are considered;  $H/\lambda = 1/100$ ,  $H/\lambda = 1/60$  and  $H/\lambda = 1/30$ . The numerical calculation methods assume respectively diffracted waves and undisturbed incident waves to be acting on the nets and columns surrounding the centre spar.

The surge RAOs in Figure 6.32a shows that assuming a diffracted wave profile managed to yield results that were in relatively good compliance with the experimental results, for the entire range of wave periods. However a deviation might be observed at roughly  $T = 1.5s$ , which might be a result of numeric instability or singularities in WAMIT, as a result of heave resonance occurring close to this wave period. Assuming incident waves as seen in Figure 6.32b seems to yield relatively good results up until  $T = 0.9s$ . For larger periods than that a significant increase in the surge motion is observed with a peak at  $T = 1.3s$ . This is likely a result of coupling with overestimated pitch motions, thus resulting in increased surge motions.



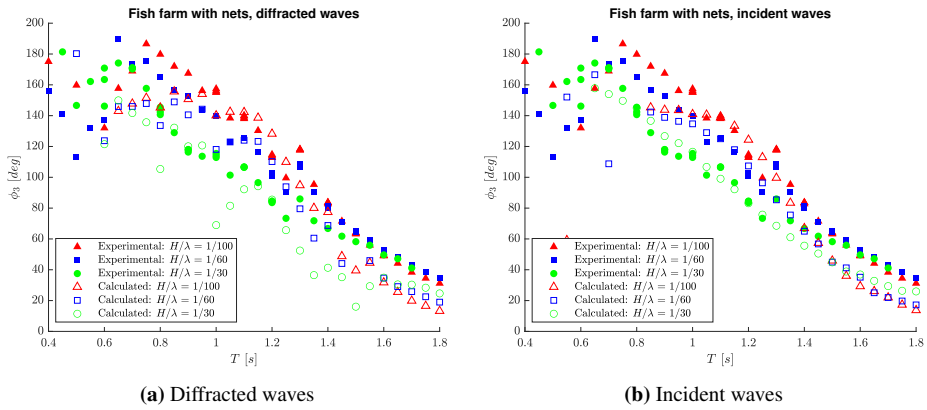
**Figure 6.33:** Comparison of numerically calculated surge phases, plotted alongside experimentally obtained surge phases, for model with nets attached. Three wave steepnesses are considered;  $H/\lambda = 1/100$ ,  $H/\lambda = 1/60$  and  $H/\lambda = 1/30$ . The numerical calculation methods assume respectively diffracted waves and undisturbed incident waves to be acting on the nets and columns surrounding the centre spar.

Looking at the surge phases in Figure it can be observed that assuming a diffracted wave pattern provided results in good compliance with the experiments for  $T > 1.1s$ . Assuming incident waves on the other hand resulted in greater deviations in that range of wave periods. In the range  $0.6s < T < 1.1s$  the phases calculated in both cases, were very similar, but did not comply with the experimental results. Whether this is because of uncertainties and inaccuracies in the experimental results for the shortest wave periods or inaccuracies in the numeric calculations is not known with absolute certainty.



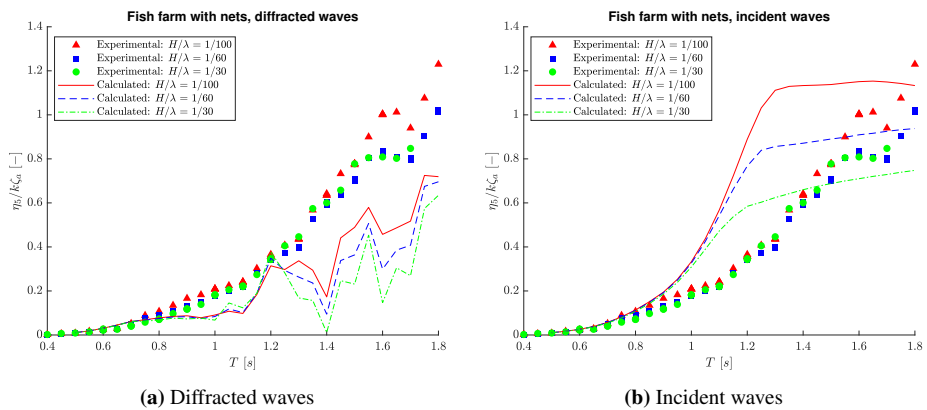
**Figure 6.34:** Comparison of numerically calculated heave RAOs, plotted alongside experimentally obtained heave RAOs, for model with nets attached. Three wave steepnesses are considered;  $H/\lambda = 1/100$ ,  $H/\lambda = 1/60$  and  $H/\lambda = 1/30$ . The numerical calculation methods assume respectively diffracted waves and undisturbed incident waves to be acting on the nets and columns surrounding the centre spar.

The calculated heave RAOs assuming diffracted waves resulted in relatively good results up until  $T = 1.3$ , even seemingly recreating small variations in the experimental results from  $1.1s < T < 1.3s$ . For longer periods the calculations start to diverge from the experiments, possibly due to some sort of numerical instability or singularity around heave resonance in WAMIT or MATLAB. This is illustrated by a significant reduction at  $T = 1.55s$  for all wave steepnesses. Assuming incident waves on the other hand yielded relatively good results, but overestimated the response at resonance slightly. This overestimation could maybe have been dealt with if radiated waves had been considered for periods close to heave resonance.



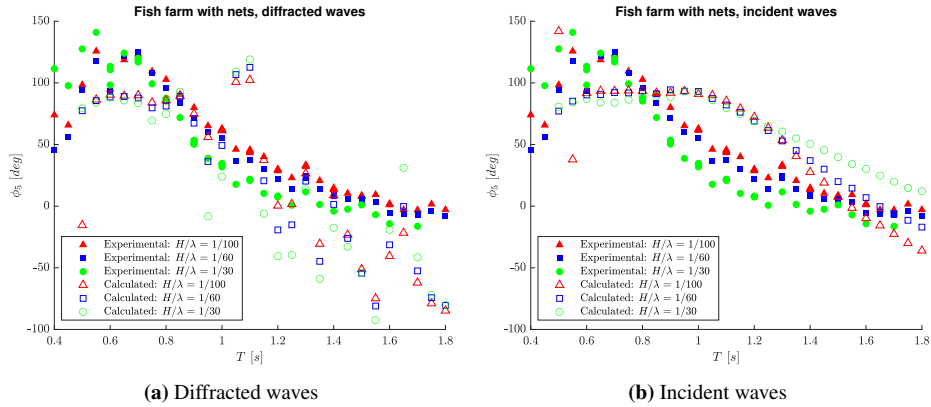
**Figure 6.35:** Comparison of numerically calculated heave phases, plotted alongside experimentally obtained heave phases, for model with nets attached. Three wave steepnesses are considered;  $H/\lambda = 1/100$ ,  $H/\lambda = 1/60$  and  $H/\lambda = 1/30$ . The numerical calculation methods assume respectively diffracted waves and undisturbed incident waves to be acting on the nets and columns surrounding the centre spar.

From the heave phases presented in Figure 6.35 it is seen that assuming incident waves yielded relatively good results, while assuming diffracted waves resulted in more scattered results, however mainly for the steepest waves. In both cases the general trend pointed towards the phases approaching  $0^\circ$  more quickly than what was the case in the experiments.



**Figure 6.36:** Comparison of numerically calculated pitch RAOs, plotted alongside experimentally obtained pitch RAOs, for model with nets attached. Three wave steepnesses are considered;  $H/\lambda = 1/100$ ,  $H/\lambda = 1/60$  and  $H/\lambda = 1/30$ . The numerical calculation methods assume respectively diffracted waves and undisturbed incident waves to be acting on the nets and columns surrounding the centre spar.

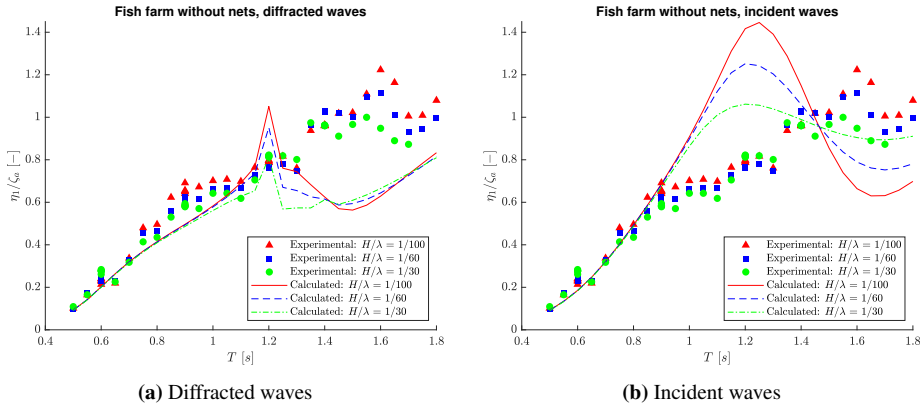
Large deviations from the experimental values was observed when calculating the pitch motions, both assuming incident waves and diffracted waves as can be seen in Figure 6.36. However assuming diffracted waves, yielded trends that might be considered comparable to the experimental results, but still with a noticeable underestimation. Errors in the numeric model and possibly inaccuracies in the velocity field provided by WAMIT might have something to do with the results. Other reasons for the deviations in both calculation methods could be related to inaccuracies in the calculations of moment of inertia, vertical centre of gravity and possibly also the drag acting on the centre spar.



**Figure 6.37:** Comparison of numerically calculated pitch phases, plotted alongside experimentally obtained pitch phases, for model with nets attached. Three wave steepnesses are considered;  $H/\lambda = 1/100$ ,  $H/\lambda = 1/60$  and  $H/\lambda = 1/30$ . The numerical calculation methods assume respectively diffracted waves and undisturbed incident waves to be acting on the nets and columns surrounding the centre spar.

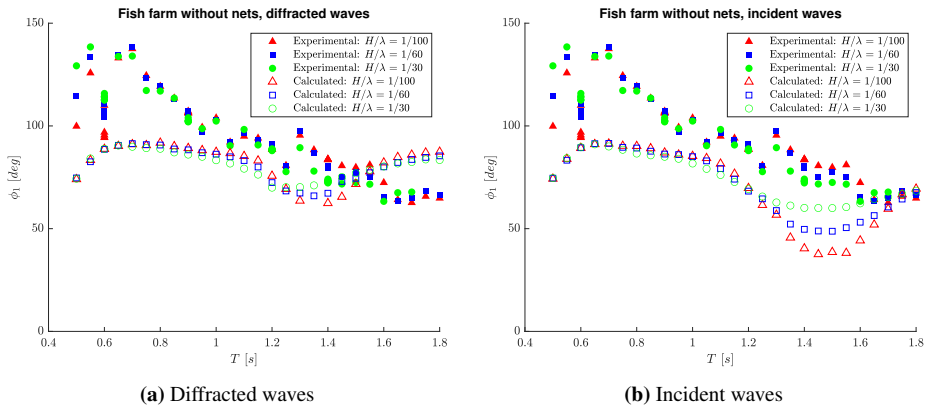
The calculated pitch phases seen in Figure 6.37 shows that large deviations from the measured phases were obtained in the calculations. The results from assuming diffracted wave yielded large scattering in the phases from one wave period to the next, while assuming incident waves provided smooth results, but with a trend that was not in accordance with the experimental results. As with the pitch RAOs it is not entirely clear why these results occurred in the calculations.

## Without nets



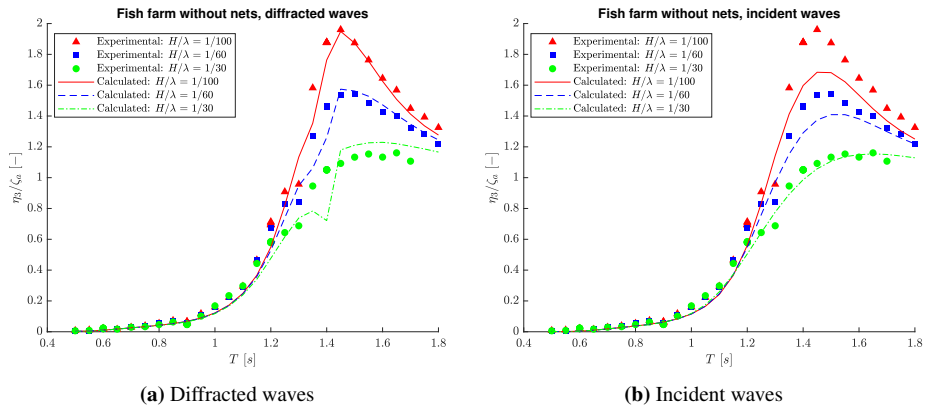
**Figure 6.38:** Comparison of numerically calculated surge RAOs, plotted alongside experimentally obtained surge RAOs, for model without nets attached. Three wave steepnesses are considered;  $H/\lambda = 1/100$ ,  $H/\lambda = 1/60$  and  $H/\lambda = 1/30$ . The numerical calculation methods assume respectively diffracted waves and undisturbed incident waves to be acting on the framework surrounding the centre spar.

From the surge RAOs there one could see relatively good results assuming diffraction up until a wave period of 1.1 s and up to 0.9 s assuming incident waves. At approximately 1.2 s there can be observed peaks in both calculation methods. The peaks from the calculations assuming undisturbed waves are significantly larger, than when assuming a diffracted wave profile. These peaks most likely comes from coupling with pitch. The most probable explanation for the deviations in the calculations relates to something being wrong in terms of the coupling. Either because of wrong centre of gravity, underestimated moment of inertia or inaccurate calculation of drag on the spar.



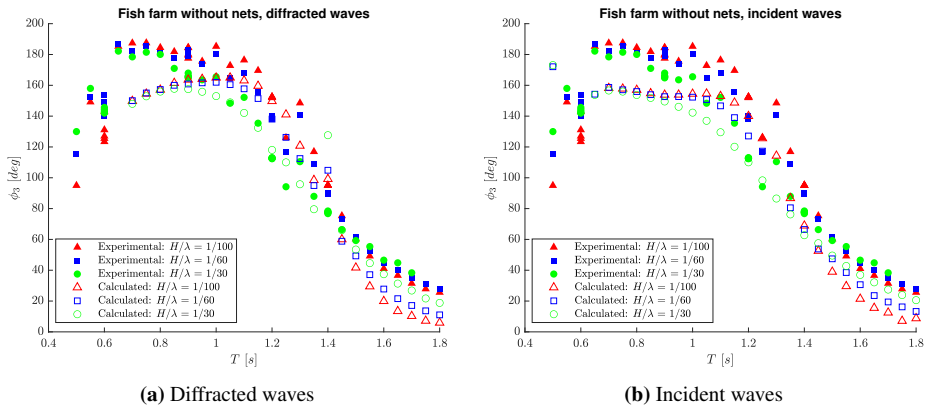
**Figure 6.39:** Comparison of numerically calculated surge phases, plotted alongside experimentally obtained surge phases, for model without nets attached. Three wave steepnesses are considered;  $H/\lambda = 1/100$ ,  $H/\lambda = 1/60$  and  $H/\lambda = 1/30$ . The numerical calculation methods assume respectively diffracted waves and undisturbed incident waves to be acting on the framework surrounding the centre spar.

As seen from Figure 6.39 the surge phases obtained in both of the calculation methods deviated quite a lot from the measurements and most noticeably for periods longer than 1.1 s. The deviations occurring at the longer wave periods is likely a result of wrongly estimated coupling between surge and pitch. While the results at the shortest periods, might in fact be more accurate than the measured phases, as  $90^\circ$  lag in the surge motions should be expected as explained previously.



**Figure 6.40:** Comparison of numerically calculated heave RAOs, plotted alongside experimentally obtained heave RAOs, for model without nets attached. Three wave steepnesses are considered;  $H/\lambda = 1/100$ ,  $H/\lambda = 1/60$  and  $H/\lambda = 1/30$ . The numerical calculation methods assume respectively diffracted waves and undisturbed incident waves to be acting on the framework surrounding the centre spar.

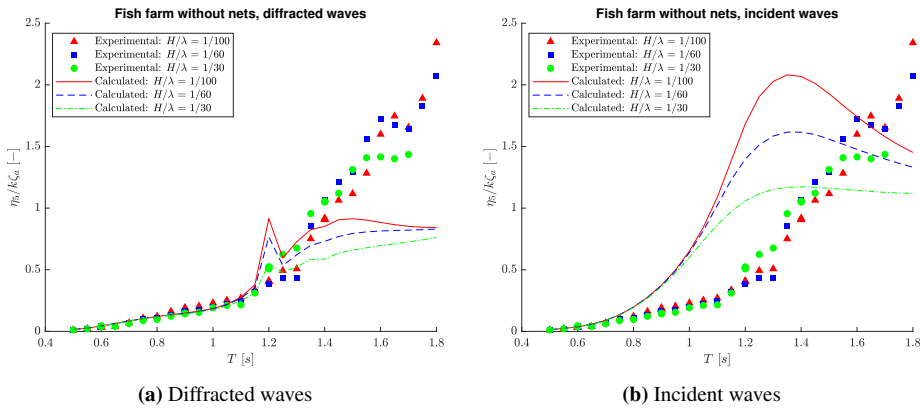
When it comes to the heave RAOs presented in Figure 6.40 very good compliance were obtained, assuming diffracted waves. In fact the results for the wave steepnesses of  $1/100$  and  $1/60$  were more or less spot on, while the calculations for the steepest waves overestimated the experimental results slightly. Assuming undisturbed incident waves on the other hand proved to yield very good results for the steepest waves, while the response at the two smallest wave steepnesses was slightly underestimated. In general the results show that taking diffraction into account on the geometry surrounding a large-volume structure, might in fact yield improved results, compared to assuming undisturbed waves. These results also seem to indicate that the implementation of the excitation forces on the spar and columns are correct and that the inaccuracies in the calculations of the surge and pitch force, without nets, relate to something being wrong in the coupling. Most likely related to the moment of inertia, vertical centre of gravity or possibly the implementation of drag on the spar, as mentioned previously.



**Figure 6.41:** Comparison of numerically calculated heave phases, plotted alongside experimentally obtained heave phases, for model without nets attached. Three wave steepnesses are considered;  $H/\lambda = 1/100$ ,  $H/\lambda = 1/60$  and  $H/\lambda = 1/30$ . The numerical calculation methods assume respectively diffracted waves and undisturbed incident waves to be acting on the framework surrounding the centre spar.

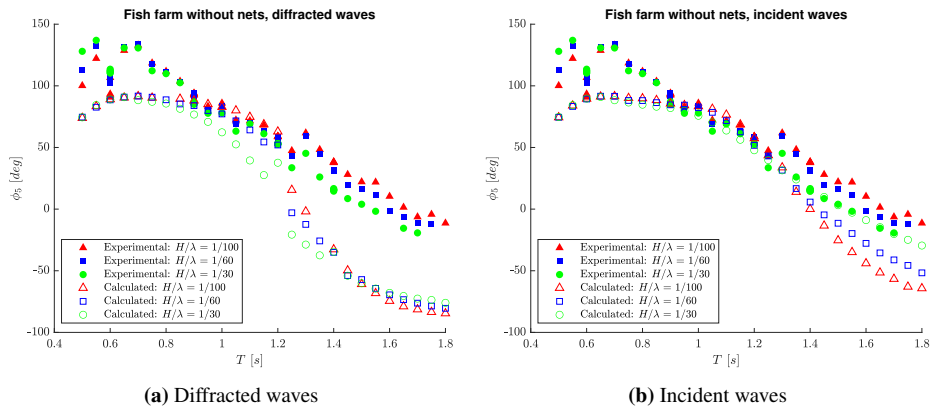
From the heave phases in Figure 6.41 it can be observed that relatively good compliance was achieved in both calculation methods, however with some deviation at the shortest wave periods. However this deviation might as well be a result of inaccuracies in the experimental phases, as the mean offset in the position of the fish farm had to be adjusted for in the post-processing of the experimental phases.





**Figure 6.42:** Comparison of numerically calculated pitch RAOs, plotted alongside experimentally obtained pitch RAOs, for model without nets attached. Three wave steepnesses are considered;  $H/\lambda = 1/100$ ,  $H/\lambda = 1/60$  and  $H/\lambda = 1/30$ . The numerical calculation methods assume respectively diffracted waves and undisturbed incident waves to be acting on the framework surrounding the centre spar.

The results from the pitch motions revealed surprisingly large differences between the calculation methods. Assuming diffracted waves yielded relatively good results up to periods of 1.1 s, before spiking slightly and further flattening out converging towards 1. The results from the incident waves also seemed to converge towards 1 for longer periods, but this however resulted in a large peak at a wave period of 1.3 s. This further increases the suspicion of the moment of inertia being underestimated, but possibly also something being wrong with the stiffness. The reason being that the peaks seem to indicate resonance, which should not occur for until the wave period is slightly larger than 1.8 s. Better results in the pitch and surge calculations, both with and without nets, might have been achieved if instead of adding stiffness due to the mooring system, there had been implemented continuous updates on the position of the mooring line attachment points and the direction of each mooring line, and further decomposed the force of acting on each one of them. As this might have provided a more realistic description of the dynamics of the mooring line forces.



**Figure 6.43:** Comparison of numerically calculated pitch phases, plotted alongside experimentally obtained pitch phases, for model without nets attached. Three wave steepnesses are considered;  $H/\lambda = 1/100$ ,  $H/\lambda = 1/60$  and  $H/\lambda = 1/30$ . The numerical calculation methods assume respectively diffracted waves and undisturbed incident waves to be acting on the framework surrounding the centre spar.

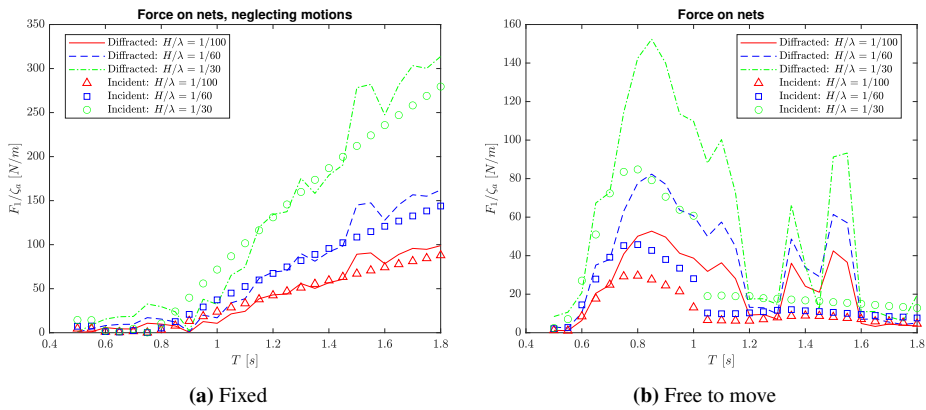
The calculated phases in pitch from Figure 6.43 further seems to indicate that pitch resonance occurs in the calculations at  $T = 1.3s$ , since the pitch phases around this wave period are close to  $0^\circ$ . Further the calculated phases converge towards  $-90^\circ$ , which would mean that that the pitch motion is in phase with the wave slope. This is the state one could expect the pitch motions to be in for wave periods significantly longer than the natural period in pitch. Thus it is likely that the pitch stiffness is slightly overestimated and the moment of inertia is somewhat underestimated, resulting in a natural period shorter than it was in reality.

### Summary of the comparisons between experimental and numerical results for fish farm in waves

The comparisons between the experimental and numerical experimental results seems to indicate that there are some errors and inaccuracies in the numeric model, especially when calculating the coupled pitch and surge motions for the fish farm without nets. However, what could be observed was that there were significant difference between assuming undisturbed incident waves and diffracted waves acting on the nets and columns. The results presented in Figure 6.32 and 6.40 even showed that in fact it is possible to obtain significantly improved results by taking diffraction into account.

### 6.3.3 Numerical assessment of the effect of diffraction on nets

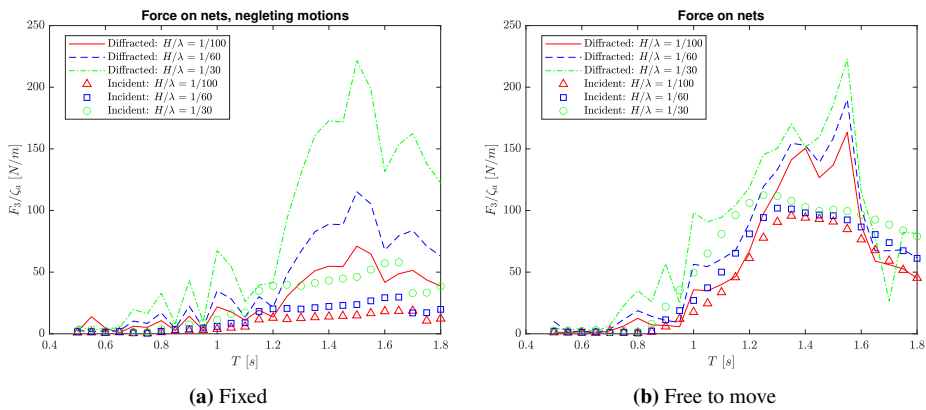
The effect of diffraction on the nets was studied by comparing the forces acting on nets, assuming respectively undisturbed incident waves and a diffracted wave-field created by the centre spar. These forces were obtained in two different ways. First off, they were obtained from the fish farm moving in waves, from the same calculations that provided the RAOs and phases. Secondly they were calculated as if the fish farm was fixed and did not move at all. The latter was done in order to try and account for any possible inaccuracies in the fish farm motions. The main reason why this was studied is because it might yield valuable information with regards to the interaction between nets and large-volume structures. It might also provide practical information concerning the dimensioning of the attachment points to the net-panels, as these have to be properly constructed in order to avoid the escape of fish.



**Figure 6.44:** Comparison of numerical calculation methods for the surge forces acting on the nets, with fish farm both fixed and free to move. Three wave steepnesses are considered;  $H/\lambda = 1/100$ ,  $H/\lambda = 1/60$  and  $H/\lambda = 1/30$ . The numerical calculation methods further assume respectively diffracted waves and undisturbed incident waves to be acting on the nets surrounding the centre spar.

First looking at the fish farm being restrained from moving in Figure 6.44a, assuming diffracted waves, it is found that there is a peak in the surge force  $T = 0.75s$  and a trough at  $T = 0.9s$ . These periods corresponds to wavelengths of approximately 0.88 m and 1.26 m. Indicating that there is an additive effect occurring for wavelengths slightly shorter than the total diameter of the fish farm and cancellation effects taking place when the wavelength is longer than the diameter of the fish farm. Considering the geometry of all the nets combined, these results should make some sense, when the body is fixed. It is also interesting that these peaks were not seen assuming incident waves. For periods longer than 1 s the surge forces were relatively similar between the two wave profiles and increased almost linearly with longer wave periods. However a minor increase in the forces could be observed at the longest wave periods, assuming diffracted waves.

Taking motions into account, seen in Figure 6.44b showed distinct peaks for all calculations at a wave period of roughly 0.8 s, likely due to additive effects as with the peaks in Figure 6.44a. What is particularly interesting to see is that, around  $T = 0.8\text{ s}$  the surge forces on the nets were approximately doubled for all wave steepnesses, when the presence of the spar was taken into account. These peaks also coincides with the peaks from the experimentally obtained surge forces seen in Figure 6.18, which is curious. The peaks are likely to be a result of speed-up around the spar and more perpendicular inflow on each net-panel, as was the case in current as well. For longer wave periods the forces on the nets were reduced significantly as a result of reduced relative velocities between the nets and the waves. However it is also observed two seemingly non-physical peaks assuming diffracted waves, which are possibly connected some numeric singularities in the velocity field occurring at heave resonance in WAMIT.



**Figure 6.45:** Comparison of numerical calculation methods for the heave forces acting on the nets, with fish farm both fixed and free to move. Three wave steepnesses are considered;  $H/\lambda = 1/100$ ,  $H/\lambda = 1/60$  and  $H/\lambda = 1/30$ . The numerical calculation methods further assume respectively diffracted waves and undisturbed incident waves to be acting on the nets surrounding the centre spar.

Looking at Figure 6.45a, for the results assuming diffraction, small peaks at periods of 0.55 s, 0.8 s, 0.9 s and 1 s likely due to additive effects in heave is observed. These were not seen assuming undisturbed waves. As the periods approach heave resonance the heave forces gets significantly larger using a diffracted wave profile and is once again assumed to be mainly caused by a singularity in the velocity field in WAMIT, possibly close to the edge at the bottom of the spar. The differences between the two wave profiles gets somewhat smaller, when motion were considered, but the peak at heave resonance assuming diffraction is still somewhat larger than what would be expected. However all things considered, the results obtained for both the heave and surge forces, seems to be pointing in the direction of the net-panel forces being increased as a result of the presence of a large-volume structure disturbing the incident waves. To see the calculated pitch moments on the nets see Appendix G. The main tendencies of these calculations followed the results presented for the heave and surge forces, as a natural consequence of the pitch moment being determined in terms of these force components.

## Conclusion

With respect to the experimental towing tests it was found that the presence of nets approximately doubled the total drag forces on the model, compared to when nets were not attached. These results were further supported by numerical calculations that were in good compliance with the experiments. In addition the numerical calculations suggested that when nets are attached, the nets themselves comprise of approximately 84.4% of the total drag force, as their presence result in a decrease of the drag force on the columns and the spar. Furthermore it can be concluded that the implementation of reduction factors, when nets are present, is essential in order to not overestimate the drag forces. As calculations without reduction factors resulted in an overestimation of as much as 160% compared to the experimental results. It was also found that the effect of speed-up and change in the direction of the flow, due to the presence of a large-volume structure, should not be neglected when nets are in proximity to this structure, as this resulted in a noticeable increase of 10.8% on the drag forces on the nets, in addition to provide more accurate results.

From the experiments in regular waves it can, for the wave periods examined, be concluded that having net-panels attached to a large-volume structure, results in significantly reduced heave and pitch motion, in addition to a slight decrease in the surge motion and some alteration of the phases, compared to when nets were not attached. The primary reason being that the nets provided an increased damping. As a result of the reduced motions, there were also observed smaller oscillatory forces in the mooring system, in addition to reduced mean wave-drift forces, when nets were attached. Even though the mean wave-drift forces were reduced with nets, these should not be neglected, for instance in dimensioning of the mooring system. Mainly because it was found that the mean wave-drift force in surge still was in the same order of magnitude as the the drag forces in pure current.

Concerning the amplitude dependency, it was found that for the range of wave periods tested, this dependency was smaller for the oscillatory mooring line forces and the heave motion when nets were fastened to the fish farm. Most likely as a result of the drag coefficient of the columns being more amplitude dependent than the nets, thus providing a greater impact on the response when nets were not attached.

With respect to the numeric results in waves, there were observed significant differences assuming undisturbed incident waves versus taking into account the presence of the centre spar, when calculating the forces on the nets and the columns. There were observed some significant deviations in the numeric results from the experimental results, revealing that there may have been some inaccuracies and possible errors in the numerical model. However there were obtained numerical results, especially from Figure 6.40 and 6.32, indicating that taking diffraction into account on structural elements in the proximity of a large-volume structure might in fact yield very good results. Further from a closer look on the forces on the net-panels in regular waves, there were obtained numerical results that pointed towards these forces being increased, when taking diffraction into account. Most likely as a result of speed-up and altered inflow angles, effects that are not considered when assuming undisturbed waves. This should therefore be taken into account when dimensioning the attachments for the nets on the fish farm.

In conclusion, there are several different interaction effects occurring between nets and a large-volume structure in proximity of one another, both in current and in waves, and this thesis has managed to uncover, study and quantify some of these interactions, both numerically and experimentally.

As recommendations for further work, it would have been interesting to see if better numerical results could have been obtained for the RAOs if equivalent linearization of the drag on the nets and columns had been used in WAMIT, before extracting the total wave-field, thus taking radiated waves into account as well. There would also have been of interest to perform tests in irregular waves in order to see how the response changes with nets, compared to without nets. It would have been of particular interest to see whether or not the resonance peak in the surge spectrum vanishes, when nets are attached. In terms of the current forces it would have been interesting to study the issue of vortex induced motions. Both to see if resonant motions could occur and to see if the presence of nets has any impact on the vortex shedding, compared to the structure without nets.

# Bibliography


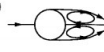







- Bachynski, E.E., Kristiansen, T., Larsen, C.M., 2019. TMR 4182 Marine Dynamics. Department of Marine Technology, NTNU.
- Blevins, R.D., 1984. Applied Fluid Dynamics Handbook. Krieger Publishing Co.
- Blevins, R.D., 2003. Applied Fluid Dynamics Handbook. Krieger Publishing Co.
- DNV, 2010. DNV-RP-C205 Environmental Conditions and Environmental Loads. URL: <https://rules.dnvgl.com/docs/pdf/dnv/codes/docs/2010-10/rp-c205.pdf>. [Accessed 06.05.2020].
- DNV, 2011. DNV-RP-H103 Modelling and Analysis of Marine Operations. URL: <https://rules.dnvgl.com/docs/pdf/DNV/codes/docs/2011-04/RP-H103.pdf>. [Accessed 04.05.2020].
- Faltinsen, O.M., 1998. Sea Loads on ships and offshore structures. Cambridge University Press.
- Goldstein, S., 1965. Modern Developments in Fluid Dynamics. Dover Publications.
- Greco, M., 2018. TMR 4215 Sea Loads, Lecture Notes. Department of Marine Technology, NTNU.
- Hess, J.L., Smith, A., 1962. Calculation of non-lifting potential flow about arbitrary three-dimensional bodies. Technical Report. Douglas Aircraft Co Long Beach CA.
- Kristiansen, T., 2019. Hydrodynamic aspects in marine operations. University Lecture.
- Kristiansen, T., Faltinsen, O.M., 2012. Modelling of current loads on aquaculture net cages. *Journal of Fluids and Structures* 34, 218–235.
- Lader, P., 2019. Aquaculture structures, sites and operations. University Lecture.
- Langen, I., Sigbjornsson, R., 1986. Dynamisk analyse av konstruksjoner. Tapir.

- 
- Løland, G., 1991. Current forces on and flow through fish farms (ph. d. thesis). University of Trondheim .
- MacCamy, R., Fuchs, R.A., 1954. Wave forces on piles: a diffraction theory. Technical Report. Corps of Engineers Washington DC Beach Erosion Board.
- Norwegian Directorate of Fisheries, 2018. Utviklingstillatelse. URL: <https://www.fiskeridir.no/Akvakultur/Tildeling-og-tillatelse/Saertillatelse/Utviklingstillatelse>. [Accessed 15.02.2020].
- Schubauer, G.B., Spangenberg, W.G., Klebanoff, P., 1950. Aerodynamic characteristics of damping screens .
- Shen, Y., Greco, M., Faltinsen, O.M., 2019. Numerical study of a well boat operating at a fish farm in current. *Journal of Fluids and Structures* 84, 77–96.
- Shen, Y., Greco, M., Faltinsen, O.M., Nygaard, I., 2018. Numerical and experimental investigations on mooring loads of a marine fish farm in waves and current. *Journal of Fluids and Structures* 79, 115–136.
- Steen, S., 2011. Motstand og propulsjon. NTNU.
- Sumer, B.M., Fredsøe, J., 2006. Hydrodynamics around cylindrical structures. volume 26. World Scientific Publishing Co. Pte. Ltd.
- Zhao, Y.P., Bi, C.W., Dong, G.H., Gui, F.K., Cui, Y., Xu, T.J., 2013. Numerical simulation of the flow field inside and around gravity cages. *Aquacultural engineering* 52, 1–13.



# Appendix

## A Flow Regimes

a)		No separation. Creeping flow	$Re < 5$
b)		A fixed pair of symmetric vortices	$5 < Re < 40$
c)		Laminar vortex street	$40 < Re < 200$
d)		Transition to turbulence in the wake	$200 < Re < 300$
e)		Wake completely turbulent. A: Laminar boundary layer separation	$300 < Re < 3 \times 10^5$ Subcritical
f)		A: Laminar boundary layer separation B: Turbulent boundary layer separation; but boundary layer laminar	$3 \times 10^5 < Re < 3.5 \times 10^5$ Critical (Lower transition)
g)		B: Turbulent boundary layer separation; the boundary layer partly laminar partly turbulent	$3.5 \times 10^5 < Re < 1.5 \times 10^6$ Supercritical
h)		C: Boundary layer com- pletely turbulent at one side	$1.5 \times 10^6 < Re < 4 \times 10^6$ Upper transition
i)		C: Boundary layer com- pletely turbulent at two sides	$4 \times 10^6 < Re$ Transcritical

**Figure 1:** Regimes of flow around a smooth, circular cylinder in steady current (Sumer and Fredsøe, 2006)

---

## B Supplementary Theory

### B.1 Diffraction Theory

The diffraction theory provided by MacCamy and Fuchs (1954), is widely used today and a detailed description of their theory is provided below. First off, one starts with the known incident wave potential,

$$\Phi_0 = \Re\{\phi_0 e^{i\omega t}\}, \quad \phi_0 = \frac{ig\zeta_a \cosh(k(z+h))}{\omega \cosh(kh)} e^{-ikx}. \quad (1)$$

The diffraction potential will be quite similar as the incident wave potential, but with a different spatial variation horizontally, and might be written as follows

$$\phi_\tau = \frac{ig\zeta_a \cosh k(z+h)}{\omega \cosh kh} \psi(x, y). \quad (2)$$

$\phi_\tau$  must satisfy the Laplace equation, which results in the Helmholtz equation,

$$\nabla^2 \phi_\tau = 0 \quad \rightarrow \quad \left( \frac{\partial^2}{\partial x^2} + \frac{\partial^2}{\partial y^2} + k^2 \right) \psi = 0 \quad (3)$$

Introducing polar coordinates,

$$x = R \cos \theta, \quad y = R \sin \theta \quad \Rightarrow \quad \psi(x, y) \rightarrow \psi(R, \theta). \quad (4)$$

This makes the Helmholtz equation take the following form,

$$\left( \frac{\partial^2}{\partial R^2} + \frac{1}{R} \frac{\partial}{\partial R} + \frac{1}{R^2} \frac{\partial^2}{\partial \theta^2} + k^2 \right) \psi = 0. \quad (5)$$

Then it is necessary to impose boundary conditions to the surface of the cylinder in order to ensure zero flux of fluid through it. This is done by enforcing zero velocity normal to the surface, as follows,

$$\frac{\partial}{\partial n} (\phi_0 + \phi_\tau) = 0 \quad \Rightarrow \quad \frac{\partial \phi_\tau}{\partial n} = -\frac{\partial \phi_0}{\partial n}, \quad (6)$$

which is the same as,

$$\frac{\partial \psi}{\partial R} = -\frac{\partial}{\partial R} (e^{-ikx}) = -\frac{\partial}{\partial R} (e^{-ikR \cos \theta}). \quad (7)$$

Then the following identity is used,

$$e^{-ikR \cos \theta} = \sum_{m=0}^{\infty} \epsilon_m J_m(kR) \cos m\theta, \quad \epsilon_m = \begin{cases} 1 & m = 0 \\ 2(-i)^m & m > 0 \end{cases} \quad (8)$$

where  $J_m$  is the Bessel function of the first kind. Based on the form of Equation 8, the following solution is tried,

---


$$\psi(R, \theta) = \sum_{m=0}^{\infty} A_m F_m(kR) \cos m\theta. \quad (9)$$

Substituting Equation 9 into Equation 5 we obtain,

$$\left(\frac{\partial^2}{\partial R^2} + \frac{1}{R} \frac{\partial}{\partial R} - \frac{m^2}{R^2} + k^2\right)F_m(kR) = 0, \quad \text{noting} \quad \frac{\partial^2}{\partial \theta^2}(\psi) = -m^2\psi. \quad (10)$$

This is recognized as the Bessel equation of order  $m$ , accepting solutions of  $F_m(kR)$ , as linear combinations of the Bessel functions of first and second kind, meaning respectively  $J_m(kR)$  and  $Y_m(kR)$ . It is necessary that the linear combination of  $J_m(kR)$  and  $Y_m(kR)$ , full-fills the radiation condition, that  $\psi$  must satisfy, in order to ensure propagating waves. The condition is that, when

$$R \rightarrow \infty \Rightarrow \psi(R, \theta) \sim e^{-ikR+i\omega t}. \quad (11)$$

Looking at the asymptotic values of the Bessel functions as  $R \rightarrow \infty$ , the following is obtained,

$$J_m(kR) \sim \sqrt{\frac{2}{\pi kR}} \cos\left(kR - \frac{1}{2}m\pi - \frac{\pi}{4}\right), \quad (12)$$

$$Y_m(kR) \sim \sqrt{\frac{2}{\pi kR}} \sin\left(kR - \frac{1}{2}m\pi - \frac{\pi}{4}\right). \quad (13)$$

The Hankel function of second kind( $H_m^{(2)}(kR)$ ) will then satisfy the far-field radiation condition in Equation 11, as presented below

$$H_m^{(2)}(kR) = J_m(kR) - iY_m(kR) \sim \sqrt{\frac{2}{\pi kR}} e^{-i(kR - \frac{1}{2}m\pi - \frac{\pi}{4})}. \quad (14)$$

Replacing  $F_m$  in Equation 9 with the Hankel function yields,

$$\psi(R, \theta) = \sum_{m=0}^{\infty} \epsilon_m A_m H_m^{(2)}(kR) \cos m\theta, \quad (15)$$

meaning that now only the constants  $A_m$  have to be determined. These are found from the boundary condition on the surface of the cylinder( $R = a$ ) from Equation 7,

$$\left.\frac{\partial\psi}{\partial R}\right|_{R=a} = -\left.\frac{\partial}{\partial R} \left(\sum_{m=0}^{\infty} \epsilon_m J_m(kR) \cos m\theta\right)\right|_{R=a} \quad (16)$$

resulting in,

$$\left.\frac{\partial}{\partial R}(A_m H_m^{(2)}(kR))\right|_{R=a} = -\left.\frac{\partial}{\partial R}(J_m(kR))\right|_{R=a} \quad (17)$$

---

which when using prime notation for the derivative, is the same as,

$$A_m H_m^{(2)'}(ka) = -J_m'(ka), \quad \text{thus} \quad A_m = -\frac{J_m'(ka)}{H_m^{(2)'}(ka)}. \quad (18)$$

The total complex potential is then given as follows,

$$\phi = (\phi_0 + \phi_7) e^{i\omega t} \quad (19)$$

$$\phi = \frac{ig\zeta_a}{\omega} \frac{\cosh k(z+h)}{\cosh kh} \left( \sum_{m=0}^{\infty} \epsilon_m \left[ J_m(kR) - \frac{J_m'(ka)}{H_m^{(2)'}(ka)} H_m^{(2)}(kR) \right] \cos m\theta \right) e^{i\omega t} \quad (20)$$

## C Experimental results for sway, roll and yaw

The figures provided in this appendix are the experimental results obtained from testing of the model with and without nets attached, in head sea regular waves. The results presented are for sway, roll and yaw. These were obtained from testing of three different wave steepnesses;  $H/\lambda = 1/100$ ,  $H/\lambda = 1/60$  and  $H/\lambda = 1/30$ .

### C.1 Sway

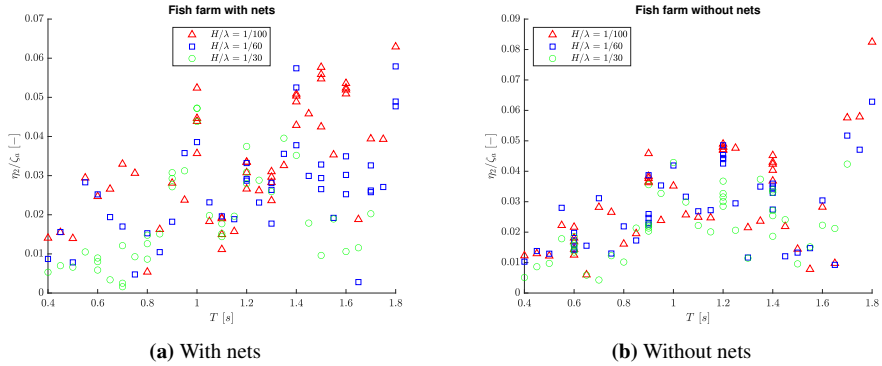


Figure 2: Sway RAOs with and without nets.

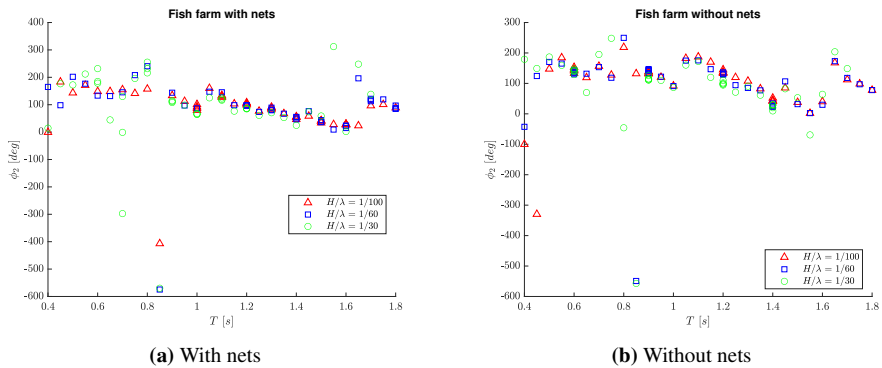
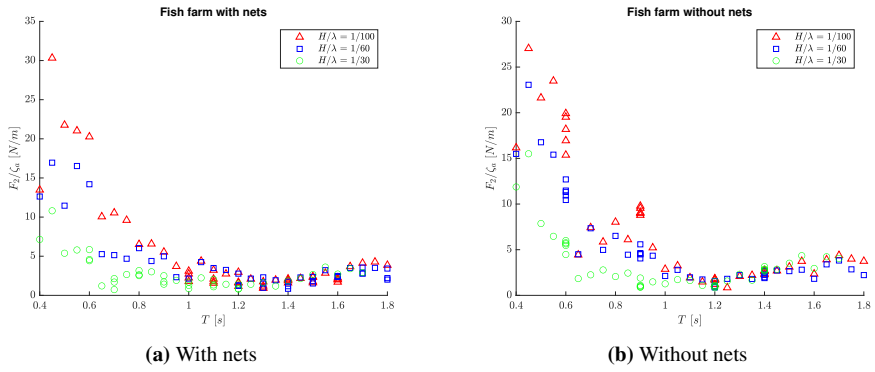
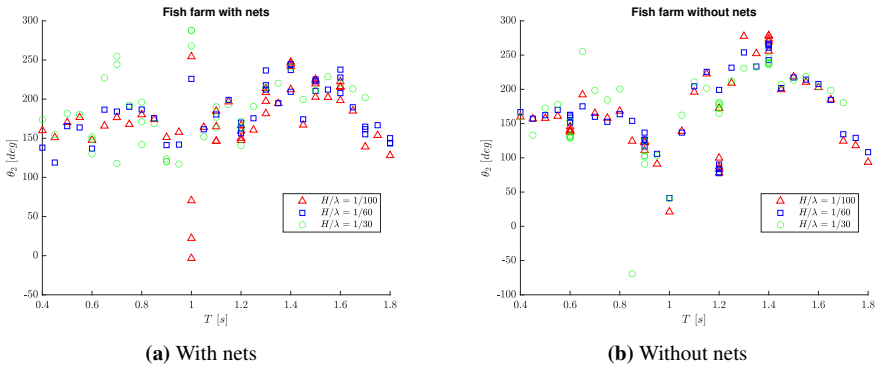


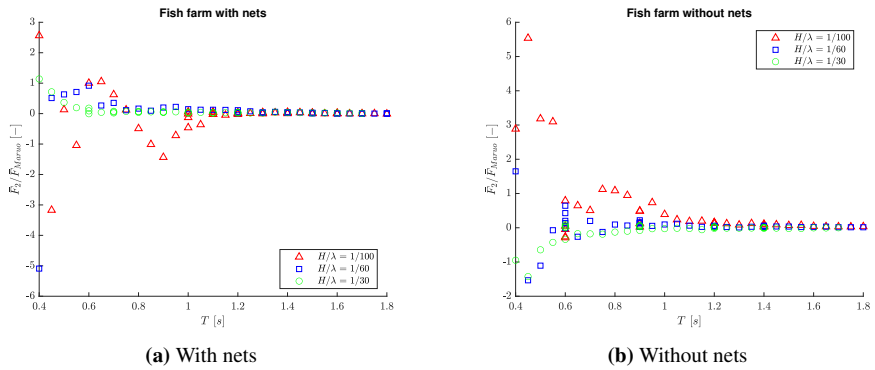
Figure 3: Sway phases with and without nets.



**Figure 4:** Mooring system sway force RAOs with and without nets.



**Figure 5:** Mooring system sway force phases with and without nets.



**Figure 6:** Non-dimensionalized mooring system mean sway force RAOs with and without nets.

## C.2 Roll

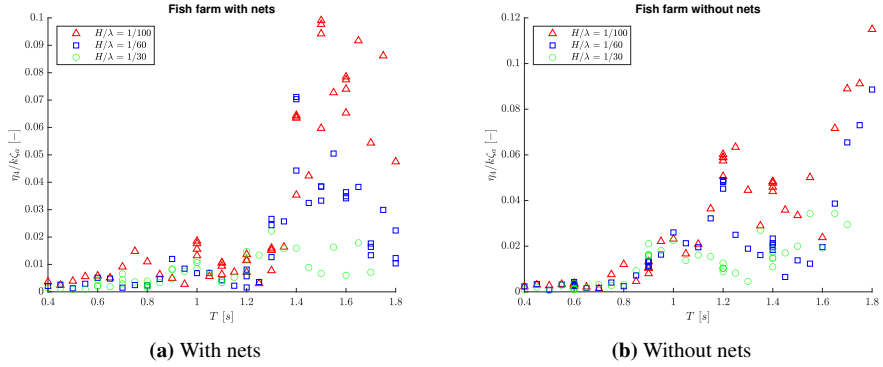


Figure 7: Roll RAOs with and without nets.

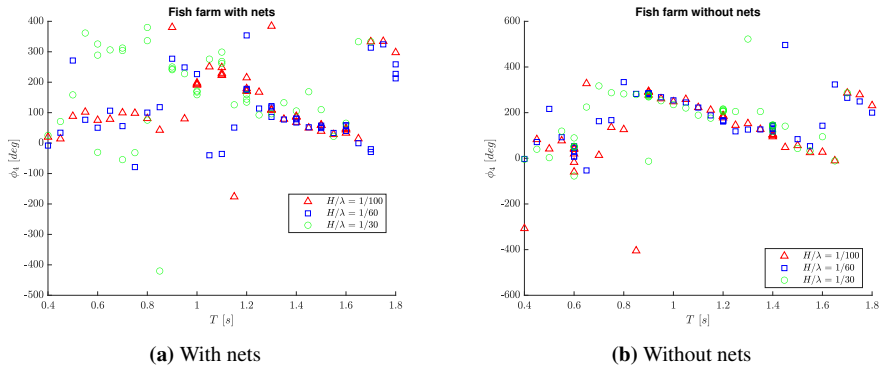


Figure 8: Roll phases with and without nets.

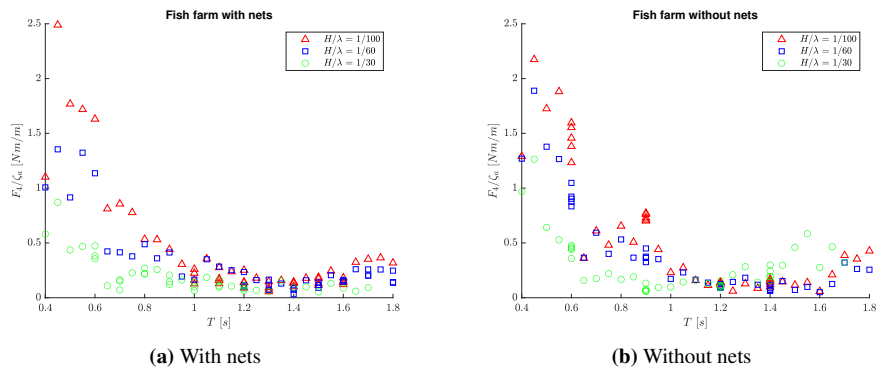


Figure 9: Mooring system roll moment RAOs with and without nets.

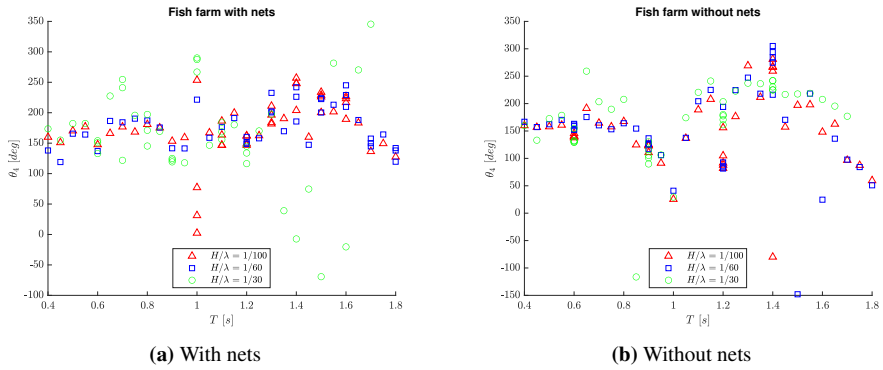


Figure 10: Mooring system roll moment phases with and without nets.

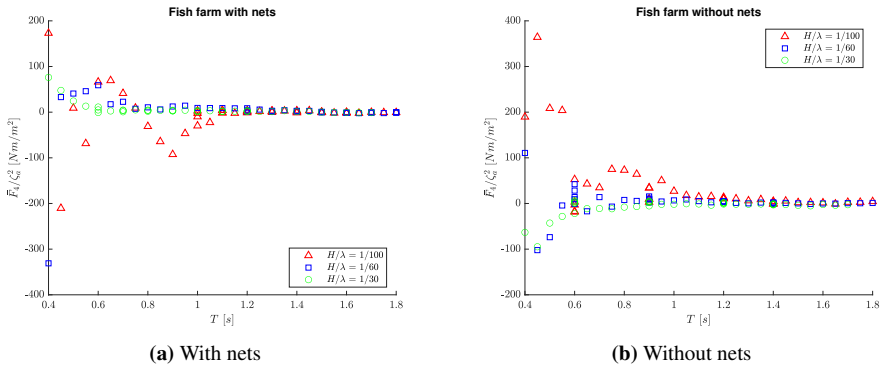


Figure 11: Mooring system mean roll moment RAOs with and without nets.

### C.3 Yaw

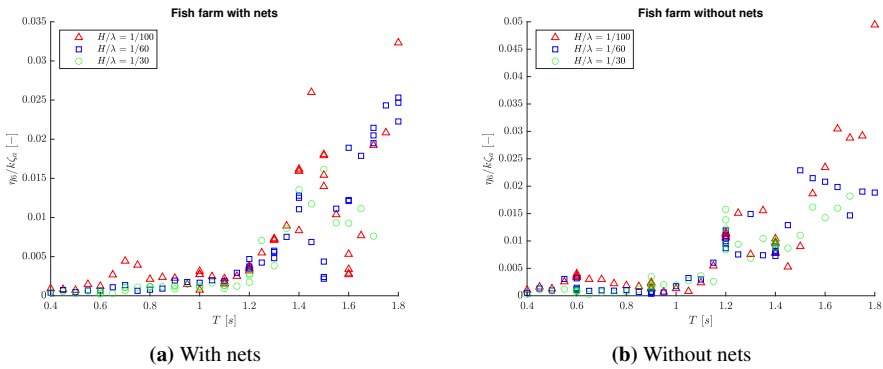


Figure 12: Yaw RAOs with and without nets.



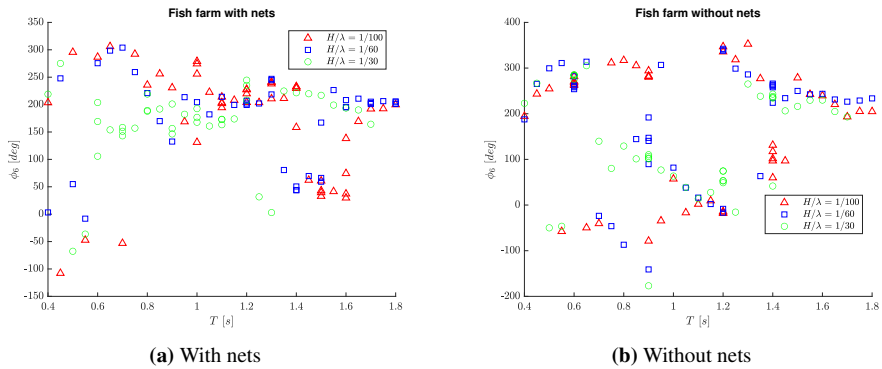


Figure 13: Yaw phases with and without nets.

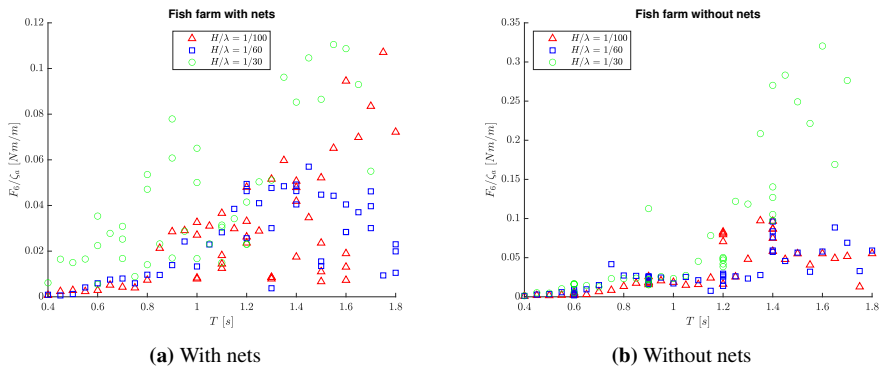


Figure 14: Mooring system yaw moment RAOs with and without nets.

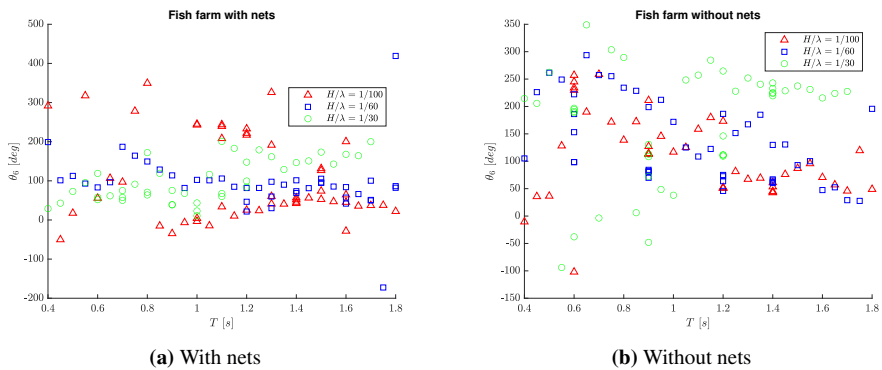
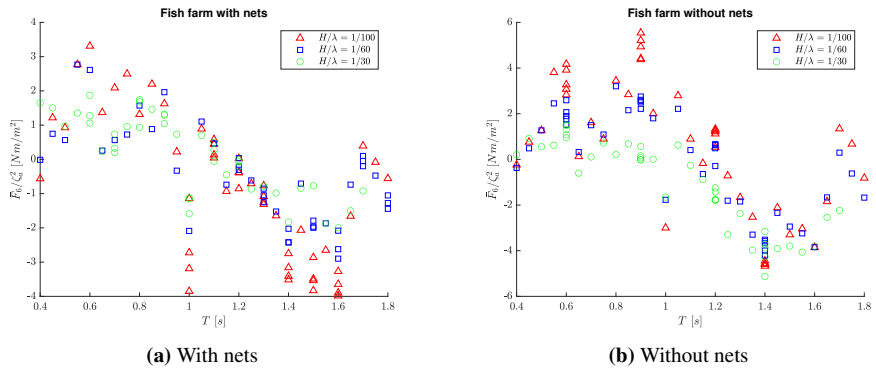


Figure 15: Mooring system yaw moment phases with and without nets.



**Figure 16:** Mooring system mean yaw moment RAOs with and without nets.

---

## D Stiffness and mass-matrices

Provided below are the mass- and stiffness matrices used for the numeric calculations of the fish farm with and without nets. Note that differences in the stiffness matrices are due to slightly different pretensions in mooring lines during experimental testing.

### D.1 With nets

$$\mathbf{M} = \begin{bmatrix} 18.4257 & 0 & 0 & 0 & -3.4272 & 0 \\ 0 & 18.4257 & 0 & 3.4272 & 0 & 0 \\ 0 & 0 & 18.4257 & 0 & 0 & 0 \\ 0 & 3.4272 & 0 & 2.0527 & 0 & 0 \\ -3.4272 & 0 & 0 & 0 & 2.0527 & 0 \\ 0 & 0 & 0 & 0 & 0 & 2.0920 \end{bmatrix} \quad (21)$$

$$\mathbf{C} = \begin{bmatrix} 58.2000 & 0 & 0 & 0 & 0 & 0 \\ 0 & 58.2000 & 0 & 0 & 0 & 0 \\ 0 & 0 & 524.8637 & 0 & 0 & 0 \\ 0 & 0 & 0 & 32.3213 & 0 & 0 \\ 0 & 0 & 0 & 0 & 32.3213 & 0 \\ 0 & 0 & 0 & 0 & 0 & 14.5500 \end{bmatrix} \quad (22)$$

### D.2 Without nets

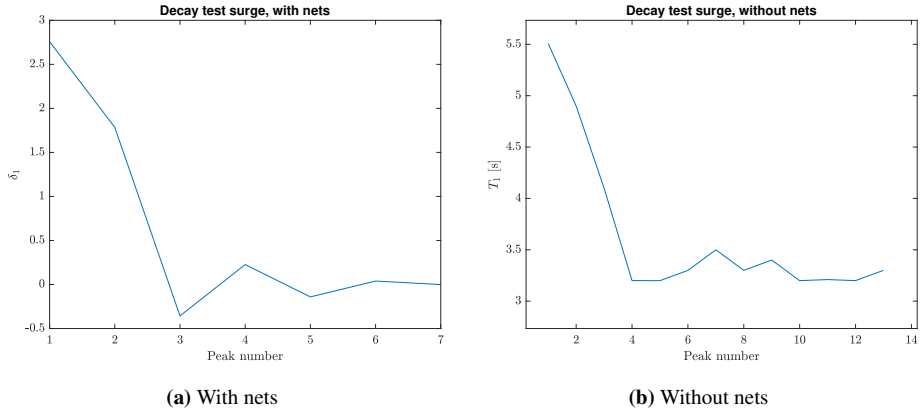
$$\mathbf{M} = \begin{bmatrix} 17.9500 & 0 & 0 & 0 & -3.6330 & 0 \\ 0 & 17.9500 & 0 & 3.6330 & 0 & 0 \\ 0 & 0 & 17.9500 & 0 & 0 & 0 \\ 0 & 3.6330 & 0 & 1.7943 & 0 & 0 \\ -3.6330 & 0 & 0 & 0 & 1.7943 & 0 \\ 0 & 0 & 0 & 0 & 0 & 1.6642 \end{bmatrix} \quad (23)$$

$$\mathbf{C} = \begin{bmatrix} 58.2000 & 0 & 0 & 0 & 0 & 0 \\ 0 & 58.2000 & 0 & 0 & 0 & 0 \\ 0 & 0 & 523.3430 & 0 & 0 & 0 \\ 0 & 0 & 0 & 28.6939 & 0 & 0 \\ 0 & 0 & 0 & 0 & 28.6939 & 0 \\ 0 & 0 & 0 & 0 & 0 & 14.5500 \end{bmatrix} \quad (24)$$

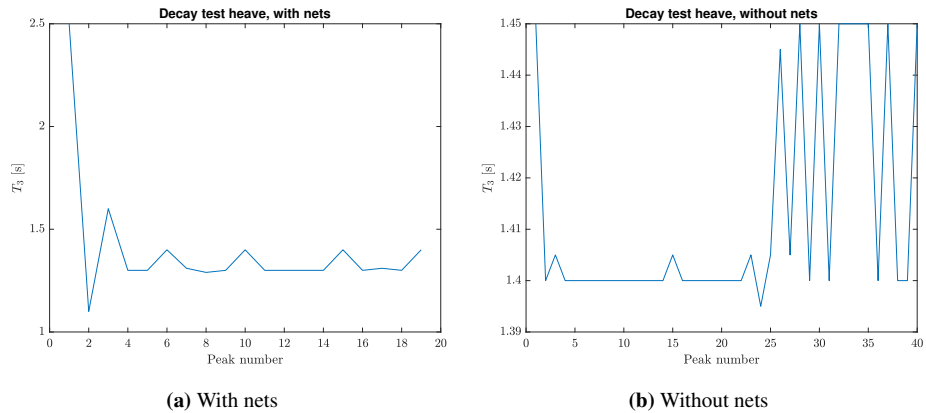
---

## E Natural periods using logarithmic decrement

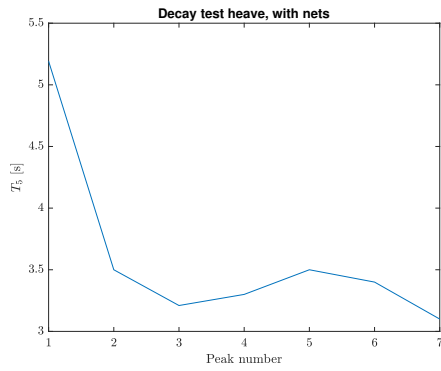
In this appendix there are provided figures of the natural periods in surge, heave and pitch, obtained from decay tests, with and without nets.



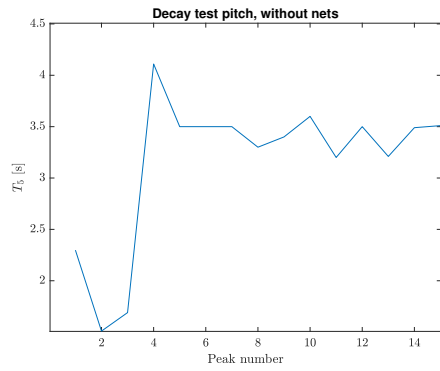
**Figure 17:** Natural period in surge as function of response peaks.



**Figure 18:** Natural period in heave as function of response peaks.



(a) With nets



(b) Without nets

**Figure 19:** Natural period in pitch as function of response peaks.

## F Hydrodynamic quantities from WAMIT

The figures provided in this appendix, are the hydrodynamic coefficients and excitation force for the centre spar of the fish farm, calculated in WAMIT. These quantities were calculated from meshes with different number of elements, in order to check convergence.

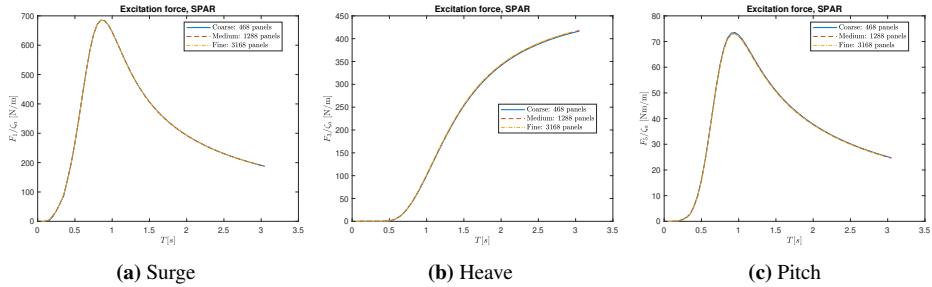


Figure 20: Excitation force in surge, heave and pitch.

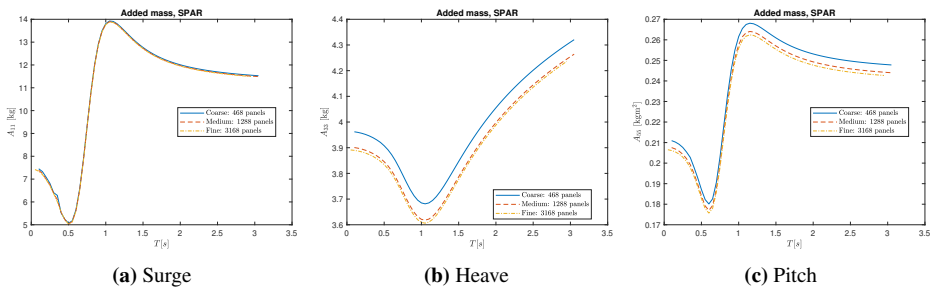


Figure 21: Added mass in surge, heave and pitch.

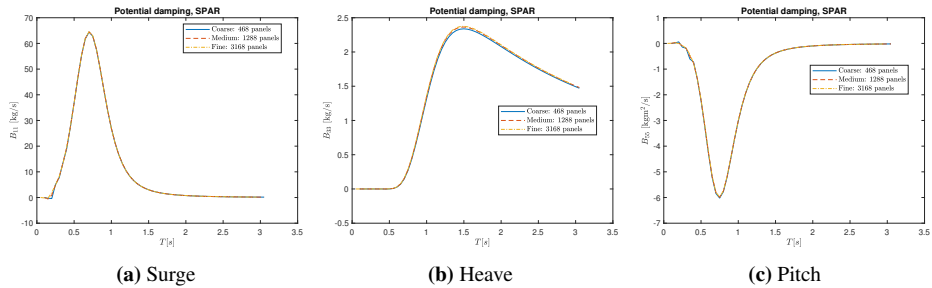
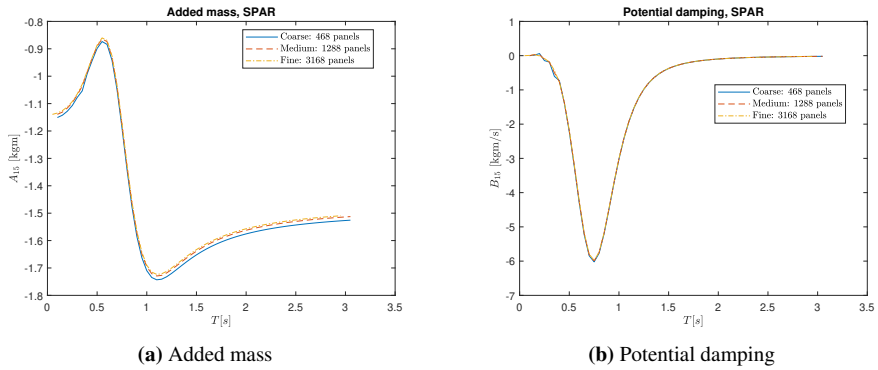


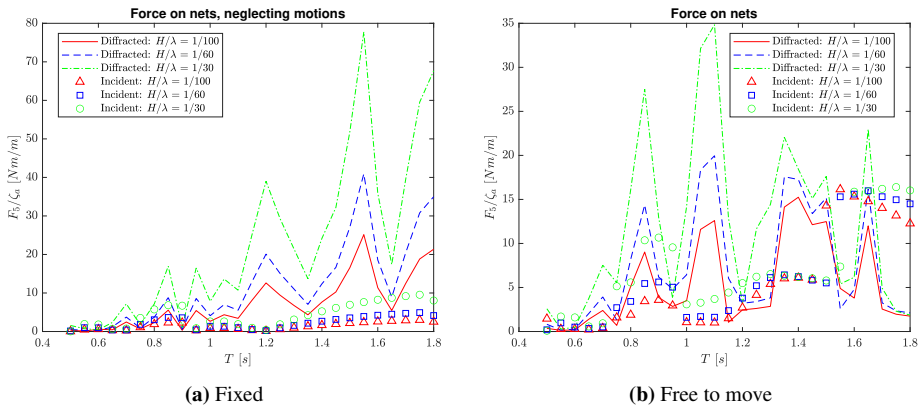
Figure 22: Potential damping in surge, heave and pitch.



**Figure 23:** Added mass and potential damping for coupled surge/pitch.

## G Net-panel moments

The figures presented below are the pitch moments acting on the nets assuming incident and diffracted waves, with the fish farm both fixed and free to move.



**Figure 24:** Comparison of numerical calculation methods for the pitch moments acting on the nets, with fish farm both fixed and free to move. Three wave steepnesses are considered;  $H/\lambda = 1/100$ ,  $H/\lambda = 1/60$  and  $H/\lambda = 1/30$ . The numerical calculation methods further assume respectively diffracted waves and undisturbed incident waves to be acting on the nets surrounding the centre spar.

